

https://dspace.org/

# Shape characterization of coarse particulates aided by focus variation microscopy

**Bezuidenhout, A. W.**

**2023**
https://hdl.handle.net/10539/35736

Downloaded from a DSpace repository. https://dspace.org/

# SHAPE CHARACTERIZATION OF COARSE PARTICULATES AIDED BY FOCUS VARIATION MICROSCOPY

A. W. Bezuidenhout

A research report submitted to the

FACULTY OF ENGINEERING AND THE BUILT ENVIRONMENT

UNIVERSITY OF THE WITWATERSRAND

JOHANNESBURG

in partial fulfilment of the requirements for the degree of

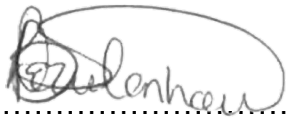
MASTER OF SCIENCE IN ENGINEERING

(CIVIL & ENVIRONMENTAL ENGINEERING)

Johannesburg, 2023

## DECLARATION

I declare that this research report is my own unaided work. It is being submitted to the Degree of Master of Science to the University of the Witwatersrand, Johannesburg. It has not been submitted before for any degree or examination to any other University.



……..

(Signature of Candidate)

17th day of January 2023

## ABSTRACT

Particle shape affects both the mechanical behaviour and packing density of soil and is thus a parameter of interest in geotechnical engineering. Shape is defined by three independent parameters: form, angularity, and roughness. This work explored the characterization of form and angularity of sand-sized specimens of different origins and shapes. The quantification of form requires the measurement of the smallest (S), intermediate (I) and largest (L) dimensions of a particle. Two of these dimensions can be readily assessed along a particle's two-dimensional outline, for example, with the aid of a microscope. Determining the third dimension, which is typically S, presents difficulties in sands. Despite advancements in modern technology, there is a lack of a simple and inexpensive method for measuring the three-dimensional form of sand.

The current work examined the efficacy of focus variation microscopy for the indirect measurement of particle height from a two-dimensional projection. Focus variation was commensurate with the measurement of particle height from a lateral projection; proving to be a relatively simple and accurate method that facilitates the quantification of form in sands.

Furthermore, particle angularity, defined by a descriptor termed 'ellipseness', was evaluated along three-orthogonal views to assess its variability. In sub-rounded and rounded particles, ellipseness in plan view was reasonably representative of the particle's mean lateral ellipseness. This descriptor adequately distinguished between rounded and angular particles, but not between particles of intermediate degrees of roundness.

## Acknowledgments

The following persons deserve acknowledgment for the role they played in supporting me and this research:

1. I cordially bid my greatest expression of gratitude to Dr. Luis Alberto Torres-Cruz, my research supervisor, for his relentless guidance, encouragement, reproach, and constructive advice that ultimately aided the satisfactory completion of this research report. Thank you for inspiring critical thinking and the incessant enhancement of one's scientific knowledge. Also, thank you for playing a kernel part in refining this research topic for this research report.
2. Thank you to former WITS (UG) students, C. Eddey and L. Tiroyabone for the availability of their 2016 IP report (on this topic).
3. I also express my sincerest gratitude to Dr Mike Otieno, Professor Y. Ballim, and Ms J. Kanjee for their generous inclination to avail the microscopy room, without any inconvenient constrictions, and for the affable support provided in the upkeep (repair) of the microscopy room's equipment.
4. Thank you to Professor Ziegler and Mr Deran Reddy from the Microscopy and Microanalysis Unit (MMU) at the University of the Witwatersrand, Johannesburg, for their support and assistance in acquiring micrographs.
5. Lastly, thank you to my beloved fiancé and family for their unconditional love and support during this period.

# TABLE OF CONTENTS

DECLARATION ..... ii

LIST OF TABLES ..... vii

LIST OF FIGURES ..... viii

LIST OF SYMBOLS ..... xiii

1 INTRODUCTION ..... 1

1.1 Topic Overview ..... 1

1.2 Research Objectives ..... 3

1.3 Organisation of this Research Report ..... 4

2 Literature Review ..... 5

2.1 Particle Shape: Form ..... 5

2.2 3Dimensional Particle Form Characterization ..... 16

2.3 Particle Shape: Angularity ..... 22

2.4 Measurement of Particle Shape: 3D Analysis ..... 27

2.5 Significance of Particle Shape ..... 29

2.6 Summative Discussion ..... 32

3 TEST PROCEDURE DEVELOPMENT ..... 34

3.1 Materials ..... 34

3.2 Particle Size Gradation ..... 38

3.3 Focus Variation (FV) Microscopy ..... 39

3.4 Focus Variation (FV) Procedure ..... 46

3.5 Form Measurement ..... 52

3.6 Angularity Measurement ..... 53

4 RESULTS & DISCUSSION ..... 55

4.1 Validation: Focus Variation (FV) Method ..... 55

4.2 Form Assessment ..... 65

4.3 Characterization of Angularity ..... 72

5 CONCLUSIONS ..... 79

6 REFERENCE LIST ..... 82

## LIST OF TABLES

Table 2-1: Definitions of 3D Form (After Clayton et al., 2009; Blott & Pye, 2008; Janoo, 1998). ..... 8

Table 2-2: Criteria for describing angularity of coarse-grained particles from ASTM 2488-17E01 (2017). ..... 25

Table 3-1: Summary of the experimental program. ..... 35

Table 3-2: NA, approximated DoF and pixel density for each objective. 45

Table 4-1: Comparison of basic statistical parameters for S/I. ..... 68

Table 4-2: Comparison of basic statistical parameters for I/L. ..... 69

Table 4-3: Comparison of basic statistical parameters for S/L. ..... 69

Table 4-4: Statistical parameters for ellipseness. ..... 76

## LIST OF FIGURES

Figure 2-1: Elements of particle shape (after Clayton et al., 2009). ..... 6

Figure 2-2: Plan view of the basic size parameters of an irregular sand particle (Wang et al., 2020). ..... 11

Figure 2-3: Example of the measurement of individual grain dimensions: (a) plan view, x-y plane; (b) elevation, y-z plane; (c) elevation, x-z plane. Dashed lines show minimum circumscribed circles and maximum inscribed circles for each view (Clayton et al., 2009). ..... 12

Figure 2-4: Comparison of S and $S_{vse}$ (redrawn after Clayton et al., 2009). ..... 14

Figure 2-5: Definitions of $D_{max}$ and $D_{min}$ (Le Pen et al., 2013). ..... 15

Figure 2-6: Comparison of S/L ratio using two methods (redrawn after Le Pen et al., 2013). ..... 16

Figure 2-7: Zingg (1935) diagram (After Le Pen et al., 2013). ..... 17

Figure 2-8: Isolines of working sphericity and shape factor plotted on the Zingg diagram (drawn by the author). ..... 18

Figure 2-9: Isolines of S/L plotted on the Zingg diagram (drawn by the author). ..... 19

Figure 2-10: Sneed & Folk (1958) ternary diagram comprising ten classes of form: C (compact), CP (compact-platy), CB (compact-bladed), CE (compact-elongated), P (platy), B (bladed), E (elongated), VP (very platy), VB (very bladed), VE (very elongated) (redrawn after Blott & Pye, 2008). ..... 20

Figure 2-11: 36 Forms plotted at regular geometric intervals to ensure even distribution of elongation and flatness ratios (a) Sneed & Folk diagram, (b) Zingg diagram (Blott & Pye, 2008)..... 21

Figure 2-12: (a) Schematic demonstrating the measure of roundness proposed by Wadell (1932), (from Blott & Pye, 2008). (b) Roundness chart for 16 – 32 mm aggregate, Krumbein (1941). ..... 23

Figure 2-13: (a) Parameters for determining the degree of angularity (After Lees, 1964), (b) Schematic indicating the measure of angularity of each corner on a projected plane (Blott & Pye, 2008). ..... 24

Figure 2-14: Visual description for particle angularity, (a) Degree of angularity (After Lees, 1964), and (b) Visual identification of aggregate angularity (after ASTM D 2488-17E01, 2017). ..... 25

Figure 3-1: Photomicrograph of West Bank beach sand..... 36

Figure 3-2: Photomicrograph of Ballito beach sand. ..... 36

Figure 3-3: Photomicrograph of crushed quartz sand. ..... 37

Figure 3-4: Photomicrograph of platinum tailings sand. ..... 37

Figure 3-5: Photomicrograph of glass beads. ..... 38

Figure 3-6: Schematic diagram of a typical measurement device based on focus variation: (1) CCD sensor, (2) lenses, (3) white light source, (4) semi-transparent mirror, (5) objective lens with limited depth of field, (6) sample, (7) vertical movement with driving unit, (8) contrast curve calculated from the local window, (9) light rays from the white light source, (10) optional analyser, (11) optional polarizer and (12) optional ring light (from Helmli, 2011)..... 40

Figure 3-7: Depth of field ranges, where NA = numerical aperture (https://www.microscopyu.com/microscopy-basics/depth-of-field-and-depth-of-focus). ..... 41

Figure 3-8: Illustration of Nikon Opti-phot Pol optical microscope, without epi-illumination system, (a) left view; (b) right view (OPTIPHOT-POL Instruction Manual). ..... 43

Figure 3-9: (a) Optical path of the Nikon Opti-phot Pol optical microscope; (b) Universal epi-illuminator (OPTIPHOT-POL Instruction Manual). ..... 44

Figure 3-10: DFK 72AUC02 CMOS Sensor (https://www.theimagingsource.com/products/industrial-cameras/usb-2.0-color/dfk72buc02/). ..... 44

Figure 3-11: Graphic user interface of NIS-Elements software (NIS Elements D, Nikon). ..... 45

Figure 3-12: Establishment of the focus variation instrument. ..... 50

Figure 3-13: Measurement of particle height from two lateral views, on a glass bead particle. ..... 50

Figure 3-14: (a) start of FV procedure, (b) end of FV procedure. ..... 51

Figure 3-15: The focus variation procedure performed at 100x magnification on a West Bank beach sand particle. ..... 51

Figure 3-16: Measurement of $D_{ic}$ and $D_{cc}$, in plan view at 50x magnification on a Ballito beach sand particle. ..... 52

Figure 3-17: Parameters used to compute ellipseness in plan-view: (a) glass bead, (b) Ballito beach sand, and (c) tailings sand. ..... 53

Figure 3-18: Construction of the circles with radii defining the degree of curvature along a particle's outline..... 54

Figure 4-1: Relationship between $D_L$ and $D_{\Delta f}$ for West Bank beach sand. ..... 56

Figure 4-2: Relationship between $D_L$ and $D_{\Delta f}$ for quartz sand. ..... 57

Figure 4-3: Relationship between $D_L$ and $D_{\Delta f}$ for platinum tailings sand.57

Figure 4-4: Relationship between $D_L$ and $D_{\Delta f}$ for glass beads. ..... 58

Figure 4-5: Relationship between $D_L$ and $D_{\Delta f}$ for Ballito beach sand. .... 58

Figure 4-6:Relationship between $D_L$ and $D_{\Delta f}$ for the entire dataset. ..... 59

Figure 4-7: Error, $D_L$ - $D_{\Delta f}$, plotted against $D_L$ for the entire dataset. ..... 59

Figure 4-8: Frequency distribution diagrams, (a) Overestimation and underestimation errors and (b) Error defined by $D_L$ - $D_{\Delta f}$. ..... 60

Figure 4-9: $D_{L1} – D_{L2}$ vs $D_L$ for the entire dataset. ..... 63

Figure 4-10: S-curve distributions for the normalized absolute $(D_L-D_{\Delta f})/D_L$ and the normalized absolute $(D_{L1}-D_{L2})/D_L$. ..... 63

Figure 4-11: Relationship between the normalized error and $D_L$. ..... 64

Figure 4-12: Error, $D_L$ - $D_{\Delta f}$, vs $D_{\Delta f}$, filtered by magnification. ..... 64

Figure 4-13: Absolute normalized error plotted against $D_{\Delta f}$. ..... 65

Figure 4-14: Plot of form parameters showing West Bank beach sand. 66

Figure 4-15: Plot of form parameters showing crushed quartz sand. .... 66

Figure 4-16: Plot of form parameters showing platinum tailings sand... 67

Figure 4-17: Plot of form parameters showing spherical glass beads... 67

Figure 4-18: Plot of form parameters showing Ballito beach sand. ..... 68

Figure 4-19: Flatness ratio, S/I, plotted against Pythagorean size, P.... 70

Figure 4-20: Elongation ratio, I/L, plotted against Pythagorean size, P. 71

Figure 4-21: Degree of equancy, S/L, plotted against Pythagorean size, P. ..... 71

Figure 4-22: $E_p$ plotted against $E_L$. ..... 72

Figure 4-23: The trend of $E_P$ - $E_L$, expressed as a percentage of $E_L$, plotted against $E_L$ ..... 73

Figure 4-24: Comparison of $E_p$, $E_{L1,}$ and $E_{L2}$: (a) to (c) glass bead, (d) to (f) platinum tailings particle. ..... 74

Figure 4-25: Evaluation of $E_p$ against Wadell's (1932) roundness, R. ... 78

Figure 4-26: $E_p$ plotted against R, including a roundness classification scheme proposed by Blott & Pye (2008). ..... 78

## LIST OF SYMBOLS

| Symbol | Description | SI Unit |
|---|---|---|
| A or $A_g$ | particle angularity | - |
| $A_o$ | area of a particle | $\mu m^2$ |
| $D_{ic}$ | diameter of the maximum inscribed circle | µm |
| $D_{cc}$ | diameter of the minimum circumscribed circle | µm |
| $D_{max}$ | longest line intersecting a particle's centroid of area between two points situated on a particle's outline | µm |
| $D_{min}$ | shortest line intersecting a particle's centroid of area between two points situated on a particle's outline | µm |
| DRI | disc-rod index | - |
| E | ellipseness | - |
| $Feret_{max}$ | maximum distance between two boundary parallel lines of a particle projection contour | µm |
| $Feret_{min}$ | minimum distance between two boundary parallel lines of a particle projection contour | µm |
| $G_s$ | specific gravity | - |
| R | particle roundness index | - |
| $R^2$ | coefficient of determination | - |
| S, I, and L | smallest, intermediate and largest dimensions of a particle | µm |
| P or $P_o$ | perimeter of the contour/outline of the particle/object | µm |
| $P_e$ | perimeter of an equivalent area ellipse | µm |
| SEES | scalene ellipsoid equivalent sphericity | - |
| $S_{vse}$ | volume equivalent minor dimension of a scalene ellipsoid | µm |
| V | volume | $m^3$ |
| W | mass | kg |

# 1 INTRODUCTION

## 1.1 Topic Overview

Particle shape is an important soil index property influencing both the physical and mechanical behaviour of a soil mass (Holtz and Kovacs, 1981; Cho et al., 2006; Clayton et al, 2009; Shin & Santamarina, 2013). Shape is generally described by three independent multi-scale descriptors: form, angularity, and roughness. Form describes a particle's overall aspect ratio, angularity depicts the sharpness of the edges and corners, and roughness relates to small-scale surface irregularities (Janoo, 1998; Clayton et al., 2009; Wang et al., 2020). These components of shape are considered independent because each can vary widely without influencing the others (Barrett, 1980; Le Pen et al., 2013).

Although full quantification of particle form requires consideration of its three-dimensional (3D) nature, the quantification of two-dimensional (2D) form in sands is often preferred due to: (i) the lack of a simple, quick and inexpensive method for quantifying 3D form and (ii) practical difficulties associated with measuring the overall dimensions in sand-sized particles from three orthogonal orientations. This introduces important limitations because 2D form parameters cannot discriminate flat (platy) particles from bulky particles (Clayton et al., 2009) and therefore, may not adequately represent a particle's form. Of engineering relevance, flat and bulky particles exhibit different mechanical behaviours (Clayton et al., 2009).

Three-dimensional form requires the measurement of the smallest (S), intermediate (I) and largest (L) dimensions of a particle. If a particle displays

its maximum projection area in plan view, dimensions I and L can be readily measured along its 2D outline. From this 2D projection, the particle's height (which is hidden from the plan view) is required to quantify its 3D form.

Hence, this research explored the efficacy of focus variation microscopy using a conventional optical microscope, with a limited depth of field, to measure particle height from only one projection. Focus variation involves the steady adjustment of the fine focus, of a microscope's objective lens, commencing at a point when the uppermost part of a particle is in sharp focus and terminating this adjustment when the base, on which a particle rests, comes into sharp focus. The adjustment of fine focus causes a vertical displacement of the microscope's stage (on which the particle's base rests). The vertical displacement can be calculated using the graduation marks indicated on the microscope's coarse and fine focus knobs. Alternatively, a dial indicator, adequately established on a microscope's stage, can also be used to measure the stage's vertical displacements. The total vertical displacement travelled by a microscope's stage, during the fine focus adjustment procedure, can provide an accurate indirect measurement of particle height (which typically corresponds to the smallest particle dimension S due to the tendency of any object to fall with its centre of mass as close as possible to the supporting surface). Focus variation essentially aids the quantification and characterization of 3D form in sand-sized particles.

With the aid of micrographs, the measurement of particle angularity, expressed by a 2D angularity descriptor termed 'ellipseness', was

performed following Le Pen et al. (2013). The advantage of using ellipseness relates to the ease and efficiency of its computation compared to other 2D angularity descriptors. Ellipseness was measured along three orthogonal views (of each particle) to assess whether ellipseness in plan view was adequately representative of a particle's mean lateral ellipseness. Hence, this research objective would investigate the efficacy with which a particle's overall ellipseness can be characterized using a single 2D view instead of rotating the particle to three orthogonal views.

Ellipseness was further evaluated against Wadell's (1932) roundness index, R, to assess the descriptor's effectiveness in distinguishing between various degrees of roundness. Wadell's roundness index, varying between 0 and 1 (where 1 represents a perfectly rounded particle and 0 describes a particle of perfect angularity), was chosen because it adequately differentiated particles of different roundness classes or degrees of roundness from one another.

## 1.2 Research Objectives

This work covers the following three research objectives:

1. Investigate the efficacy with which particle height can be inferred using focus variation microscopy, for particles varying in size between 50 μm and 1200 μm.
2. Investigate the efficacy with which the angularity descriptor termed 'ellipseness' can be used to characterize a particle's overall angularity using only a single 2D view.

3. Evaluate the effectiveness with which ellipseness can distinguish between various classes of roundness in sand-sized particles when evaluated against Wadell's (1932) roundness index (R).

## 1.3 Organisation of this Research Report

Chapter 2 provides a topical review that summarises, and critically appraises the findings from the present literature. Chapter 3 outlines the experimental programme, including a detailed discussion on the development of the focus variation procedure. Validation of the focus variation procedure is presented in Chapter 4, including the analysis of experimental results pertinent to research objectives 2 and 3. Lastly, Chapter 5 presents a final discussion of key findings stemming from this work.

# 2 Literature Review

This chapter provides a summative discussion of important literature describing form and angularity, particularly elaborating on some noteworthy contributions made by various researchers. This chapter also reviews alternative methods of measuring particle form. Lastly, the significance of particle shape on the mechanical behaviour of soil is briefly discussed.

## 2.1 Particle Shape: Form

The three components of particle shape, considered to be independent, are shown below in Figure 2-1. The first descriptor, form, defines the geometric aspect ratio or overall shape at the macroscopic level of the particle's outline (Barrett, 1980; Janoo, 1998; Clayton et al., 2009). Various definitions of 3D form have been proposed (Wadell, 1932; Zingg, 1935; Krumbein,1941; Corey, 1949; Aschenbrenner, 1956; Sneed & Folk, 1958; Hawkins, 1993; Al-Rousan et al., 2007 and Blott & Pye, 2008). Characterizing 3D form requires the measurement of the smallest (S), intermediate (I), and largest (L) dimensions of a particle. Although it is generally accepted that S, I and L should be measured perpendicular to each other, they do not need to share a common intersection point (Blott & Pye, 2008). Typically, the elongation (I/L) and flatness (S/I) ratio or, another dimensionless index based on a combination of S, I, and/or L, is used to quantify and characterize particle form (Zingg, 1935; Sneed & Folk, 1958; Clayton et al., 2009; Le Pen et al., 2013; Eddey et al., 2019; Wang et al., 2020).

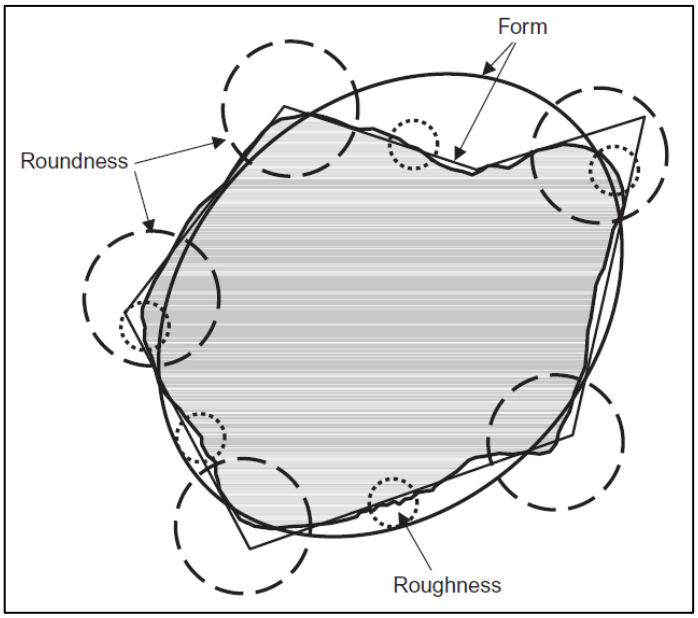



***Figure 2-1: Elements of particle shape (after Clayton et al., 2009).***

Various definitions of three-dimensional form are summarised in Table 2-1. According to Clayton et al. (2009), neither Wadell's nor Hawkins' definition of form can adequately distinguish between rod-like and plate-like forms. Clayton et al. (2009) further demonstrated that Hawkins' (1993) true sphericity fails to adequately discern between bulky (equidimensional) and platy particles, having the same major and intermediate dimensions (i.e., between cubes and square plates; cylinders and circular discs; and spheres and oblate spheroids). This is mainly due to Hawkins assuming that the particle under evaluation is spherical. The working sphericity and degree of equancy do not differentiate between discoid, bladed, and rod-like forms (as demonstrated later in section 2.3). The bladed form is not separated from discoid, rod-like, and equant forms by Aschenbrenner's (1956) shape factor. The shape factor (F) arbitrarily separates discoid and rod-like forms when F

= 1 (as discussed in section 2.3). Equant forms can exhibit a shape factor over a broad range varying between 0.67 and 1.5 (Janoo, 1998). The Oblate-Prolate index introduced by Dobkins & Folk (1970) is a function of the disc-rod index (DRI, where DRI is defined by [L-I] / [L-S]) and degree of equancy (defined by S/L). Very elongated (VE) particles (i.e., rod-like) have a DRI of between 0.67 and 1.0, whereas, very platy (VP) particles exhibit a DRI varying between 0 and 0.33. Only a clear distinction can be made between these two forms through the DRI. Blott & Pye (2008) demonstrated that the Oblate-Prolate index only distinguishes well between the extremes of platy and rod-like forms, that is, highly positive indices tend to be associated with very elongated, or rod-like, forms and highly negative indices tend to reflect very flat and platy forms.

***Table 2-1: Definitions of 3D Form (After Clayton et al., 2009; Blott & Pye, 2008; Janoo, 1998).***

| Parameter | Formula | Range | Measures | Reference |
|---|---|---|---|---|
| Wentworth flatness index | $\frac{L+I}{2S}$ | 1 to ∞ | S, I, L | Wentworth (1922a) |
| Degree of true sphericity | $\frac{S_s}{S_p}$ | 0 to 1 | $S_s$, $S_p$* | Wadell (1932) |
| Elongation and flatness ratios | $\frac{S}{I}\ and\ \frac{I}{L}$ | 0 to 1 | S, I, L | Zingg (1935) |
| Intercept sphericity | $\sqrt[3]{\frac{IS}{L^2}}$ | 0 to 1 | S, I, L | Krumbein (1941); Pye & Pye (1943) |
| Corey shape factor | $\frac{S}{\sqrt{LI}}$ | 0 to 1 | S, I, L | Corey (1949) |
| Maximum projection sphericity | $\sqrt[3]{\frac{S^2}{LI}}$ | 0 to 1 | S, I, L | Folk (1955), Sneed & Folk (1958) |

* $S_s$ = *Surface area of a sphere of the same volume as the particle and;*

$S_p$ = *Surface area of the particle*

***Table 2-1: Continued***

| Parameter | Formula | Range | Measures | Reference |
|---|---|---|---|---|
| Aschenbrenner shape factor, F† | $\frac{p}{q} = \left(\frac{S}{I}\right) x \left(\frac{L}{I}\right) = \frac{LS}{I^2}$ | 0 to 1 | S, I, L | Aschenbrenner (1956) |
| Aschenbrenner working sphericity, ψ | $\frac{12.8\sqrt[3]{p^2 q}}{1 + p(1+q) + 6\sqrt{1 + p^2(1+q^2)}}$ | 0 to 1 | S, I, L | Aschenbrenner (1956) |
| Williams shape factor, W | $1 - \frac{LS}{I^2}, when\ I^2 > LS, \frac{I^2}{LS} - 1$ | -1 to +1 | S, I, L | Williams (1965) |
| Janke form factor, E | $\frac{S}{\sqrt{\frac{L^2 + I^2 + S^2}{3}}}$ | 0 to 1 | S, I, L | Janke (1966) |
| Oblate -Prolate index | $\frac{10\left(\frac{L-I}{L-S} - 0.5\right)}{(S/L)}$ | -∞ to +∞ | S, I, L | Dobkins & Folk (1970) |
| True sphericity | $\frac{D_{vs}}{D_{cs}}$ | 0 to 1 | $D_{vs}$, $D_{cs}$ | Hawkins (1993) (in Santamarina et al., 2001) |

† *$F = p/q$, where $p = S/I$ (flatness ratio) and $q = I/L$ (elongation ratio)*

***Table 2-1: Continued***

| Parameter | Formula | Range | Measures | Reference |
|---|---|---|---|---|
| Degree of equancy | $\frac{S}{L}$ | 0 - 1 | S, L | Al-Rousan et al., (2007); Blott & Pye (2008) |
| Scalene Ellipsoid Equivalent Sphericity (SEES) | $SEES = \frac{S_{vse}}{L} = \frac{(W\ /\ nG_s)(6/\pi LI)}{L}$ | 0 - 1 | $S_{vse}$ | Clayton et al. (2009) |

When irregular shaped sand or gravel particles are dispersed onto a horizontal (x-y) plane, they tend to settle in their most mechanically stable state. Hence, for an irregular particle lying in its most mechanically stable state, the dimensions I and L tend to lie on a plane perpendicular to the line of observation under a microscope or digital camera (Figure 2-2). Hence, the particle will display its maximum projection area to the observer, because of the propensity of any object to fall with its centre of mass as close as possible to the supporting surface. Because most soil particles have irregular grain boundaries, I and L may be defined by a method involving the construction of the minimum circumscribed and maximum inscribed circles (Clayton et al., 2009; Eddey et al., 2019; Wang et al., 2020).

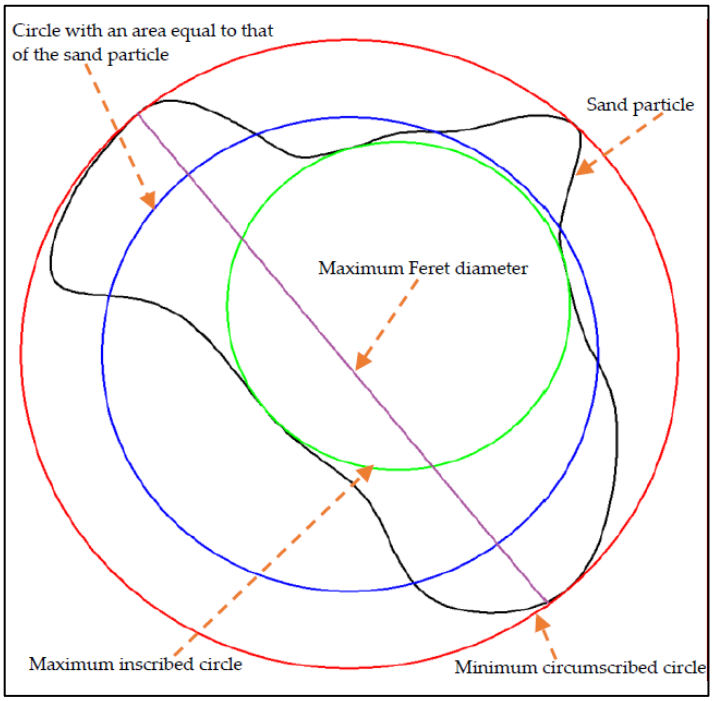



***Figure 2-2: Plan view of the basic size parameters of an irregular sand particle (Wang et al., 2020).***

Clayton et al. (2009) used the minimum circumscribed and maximum inscribed circle method in a study introducing a new method for estimating the form of coarse particulates. For each particle, the diameter of the minimum circumscribed circle, $D_{cc}$, and the diameter of maximum inscribed circle, $D_{ic}$, were determined from static digital images displaying each of three orthogonal views (Figure 2-3). The maximum projected plane was subsequently used to determine I and L, where I and L were assumed to be equal to $D_{ic}$ and $D_{cc}$, respectively.

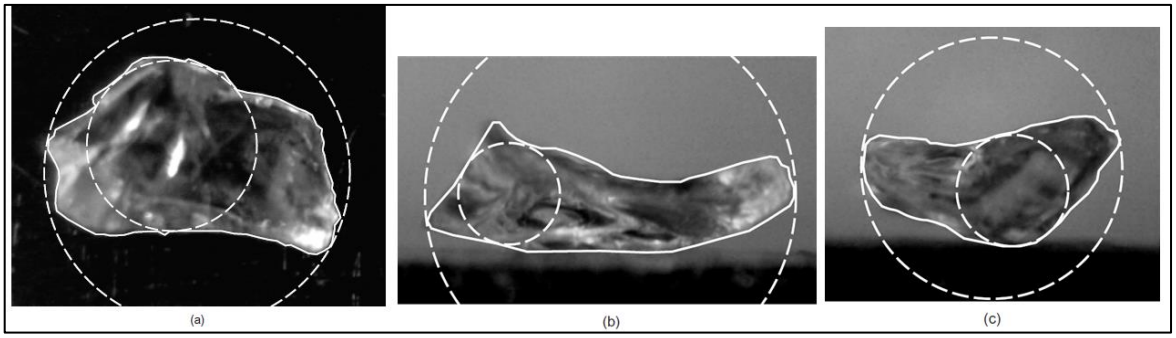



***Figure 2-3: Example of the measurement of individual grain dimensions: (a) plan view, x-y plane; (b) elevation, y-z plane; (c) elevation, x-z plane. Dashed lines show minimum circumscribed circles and maximum inscribed circles for each view (Clayton et al., 2009).***

The method proposed by Clayton et al. (2009) involved defining 3D particle form based on a *volumetric equivalent scalene ellipsoid* (i.e., an ellipsoid where the lengths of all three orthogonal principal axes are different). This arbitrary reference shape was neither two-dimensional nor spherical. After I and L are measured, the smallest dimension, S, more

accurately referred to as the *volume equivalent minor dimension of a scalene ellipsoid* ($S_{vse}$), is computed. $S_{vse}$ is calculated based on the volume (V) of a scalene ellipsoid particle defined by Eq. 2-1.

$$V = \frac{\pi}{6}(L)(I)(S) \qquad \text{Eq. 2-1}$$

Moreover, a new quotient, termed *scalene ellipsoid equivalent sphericity* (SEES) is introduced. For a group of coarse particulates, the SEES parameter can be calculated (Eq. 2-2) with the aid of automated imaging and using the: average mass (W); specific gravity ($G_s$); the total number of particles (n) and mean values of L and I.

$$SEES = \frac{S}{L} = \frac{S_{vse}}{L} = \frac{(W / nG_s)(6/\pi LI)}{L} \qquad \text{Eq. 2-2}$$

Computing a single value of $S_{vse}$ for a group of particles inevitably precludes the calculation of basic statistical descriptors such as mean, variance, standard deviation, minima, and maxima. In addition, automated image analysis has the potential to produce errors associated with counting the actual number of particles. Clayton et al., (2009) reported a maximum error of 3.95 % when automated static image analysis was used to count 937 particles of fine glass nuggets before its mean SEES value was computed.

Clayton et al., (2009) evaluated SEES against existing definitions of three-dimensional form and demonstrated that these methods (e.g. Wadell, 1932; Krumbein, 1941; Corey, 1949; Aschenbrenner, 1956; Sneed & Folk, 1958; Hawkins, 1993) do not differentiate equidimensional forms, whereas SEES excellently separated equidimensional spheres, cylinders, and cubes from

one another. A comparison between $S_{vse}$ and the measured minor dimension S (where $S = D_{ic}$, and $D_{ic}$ is assumed as the minimum diameter of the maximum inscribed circle from either lateral view) is shown in Figure 2-4. Despite the scatter, the data plots are reasonably close to the 1:1 line, producing a *coefficient of determination* ($R^2$) of approximately 0.91. Clayton et al. (2009) argued that the scatter may be due to inaccuracies associated with measuring S in irregular particles. SEES provides an alternative measure of form and differentiates between bulky and platy particles having the same major and intermediate dimensions. However, a disadvantage of the method relates to its inability to differentiate between rod-like and plate-like particles having identical major and minor dimensions, because the method provides insufficient weight to the dimension I (Clayton et al., 2009).

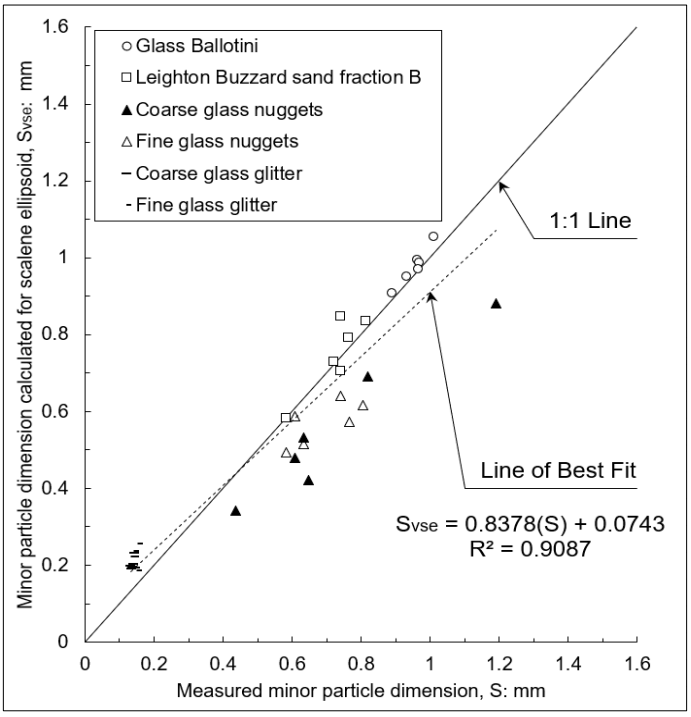



***Figure 2-4: Comparison of S and $S_{vse}$ (redrawn after Clayton et al., 2009).***

Whilst evaluating the scaled effects on form and roundness of crushed granite railway ballast, Le Pen et al. (2013) compared SEES ($S_{vse}/L$) to S/L for 120 ballast particles. The authors used two different orthogonal views to determine S, I, and L. From the two orthogonal views, $D_{max}$ and $D_{min}$ were defined as the longest and shortest lines, intersecting a particle's centroid of area, between two points situated on a particle's outline, respectively (Figure 2-5). L was defined as the absolute maximum value of $D_{max}$, I as $D_{min}$ from the most mechanically stable projection, and S as the absolute minimum value of $D_{min}$.

In regular (shaped) particles, it is reasonable to adopt the above procedure for quantifying L, I, and S provided: $S \leq I \leq L$. Figure 2-6 illustrates the trend between SEES ($S_{vse}/L$) and S/L (measured from two orthogonal views). The data does not produce a very strong correlation to the 1:1 line as indicated by the *coefficient of determination*, $R^2$, which is approximately 0.72. Figure 2-6 is essentially a comparison between $S_{vse}$ and S. Hence, the scatter in the data predominantly reflects the difference in how $S_{vse}$ and S are defined.

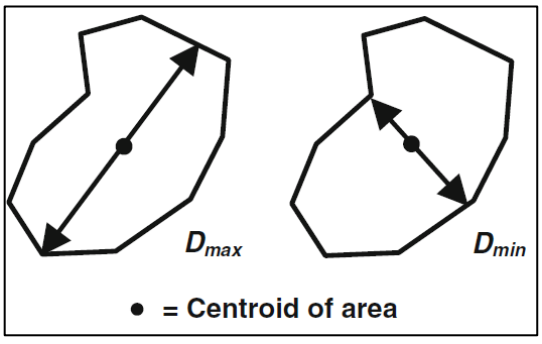



***Figure 2-5: Definitions of $D_{max}$ and $D_{min}$ (Le Pen et al., 2013).***

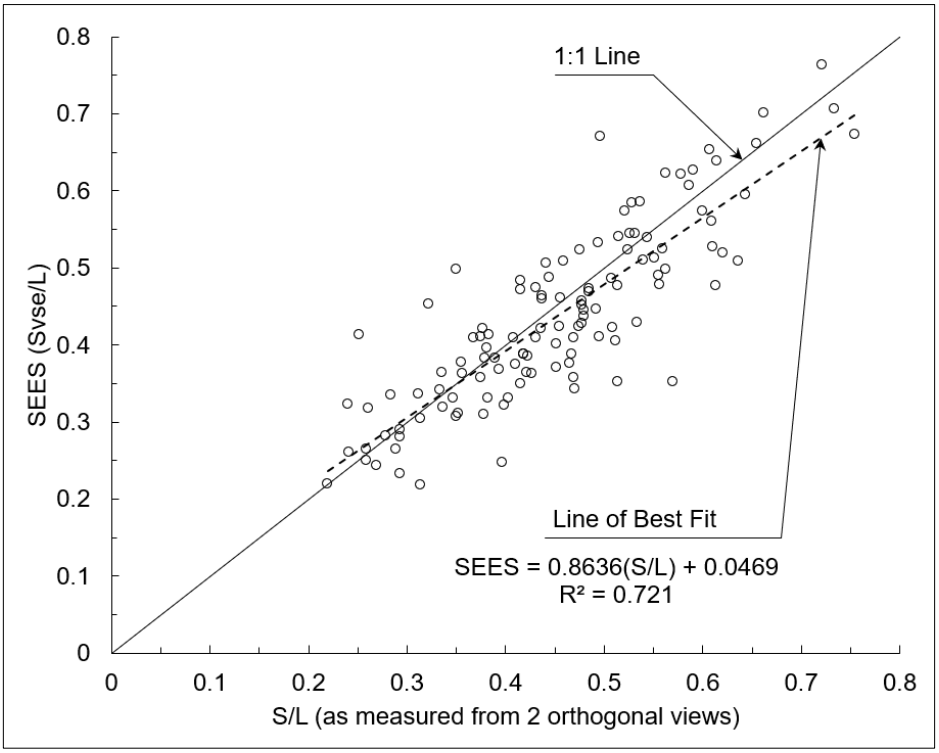



***Figure 2-6: Comparison of S/L ratio using two methods (redrawn after Le Pen et al., 2013).***

## 2.2 3Dimensional Particle Form Characterization

Zingg (1935) proposed the characterization of form in a 2D plot of I/L vs S/I (Figure 2-7). As reported by Blott & Pye (2008), the original translation of the Swiss-German terminology of Zingg's classes of form was: 'flat', 'spherical', 'flat and columnar', and 'columnar'. These form classes were later altered by Krumbein & Pettijohn (1938) and Krumbein (1941) to 'disc-shaped', 'spherical', 'bladed', and 'rod-like'. The flatness ratio differentiates blades and discs (S/I < 0.67) from rods and spheres (S/I > 0.67). The elongation ratio separates blades and rods (I/L < 0.67) from discs and spheres (I/L > 0.67). Although these divisions defining form classes are

arbitrary, the following four idealized extremes of form classes emerge (Oakey et al., 2005):

a) *equant*: spheroid or cuboid (L ≈ I ≈ S)

b) bladed (L >> I > S)

c) rod-like or elongate (L >> I ≈ S)

d) discoid (flat and platy) (L ≈ I >> S)

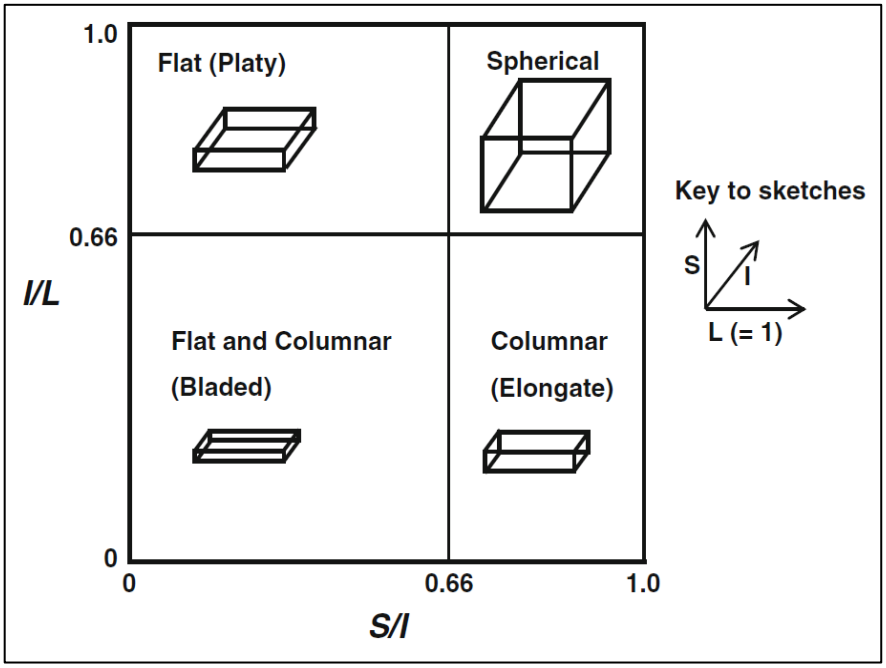



***Figure 2-7: Zingg (1935) diagram (After Le Pen et al., 2013).***

Additional descriptors emanating from sedimentary petrology used to describe the shape of aggregates include sphericity (ψ), shape factor (F), and degree of equancy (S/L) (see Table 2-1). Sphericity is defined as the

ratio of the surface area of a sphere, having the same volume as the particle of interest, to the surface area of the particle (Aschenbrenner, 1956).

Like the shape factor, isolines described by working sphericity, Ψ, (Figure 2-8) and degree of equancy, S/L, (Figure 2-9) intercept various classes of form on the Zingg diagram. S/L only separates equant forms from other classes when S/L exceeds 0.67 (Figure 2-9). Hence, S/L is more accurately a measure of equancy (Blott & Pye, 2008), instead of overall 3D form. These observations emphasize the certainty that a single scalar parameter cannot completely describe the three-dimensional form of a particle.

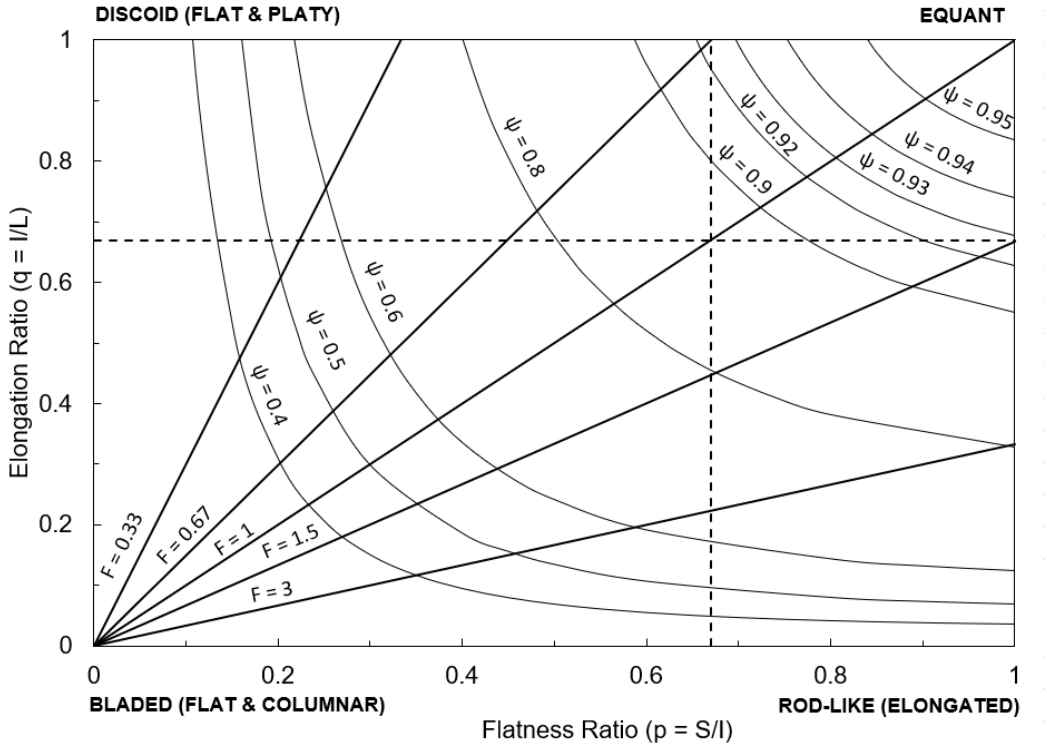



***Figure 2-8: Isolines of working sphericity and shape factor plotted on the Zingg diagram (drawn by the author).***

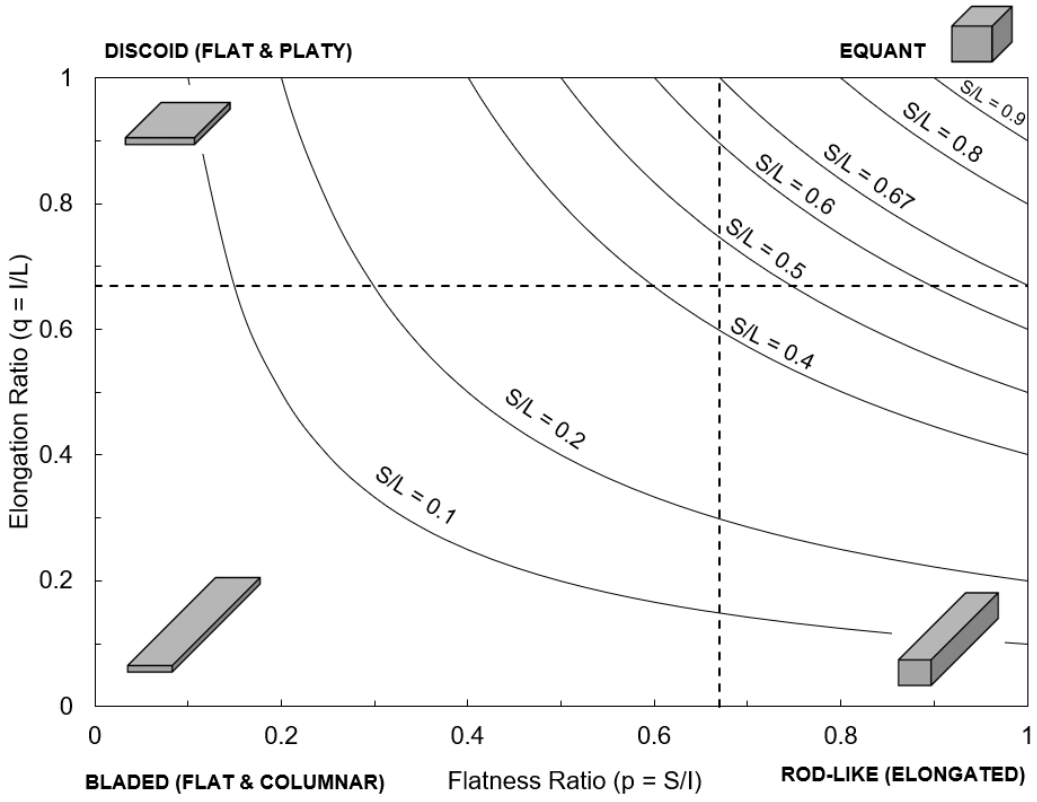



***Figure 2-9: Isolines of S/L plotted on the Zingg diagram (drawn by the author).***

Sneed & Folk (1958) proposed a ternary diagram exhibiting ten classes of form (Figure 2-10). 3D representations of three extreme classes of form (Figure 2-10) were extracted from Bonneau et al. (2019). This version of the ternary diagram uses S/L, and the disc-rod index (DRI), as proposed by Illenberger (1991).

Sneed & Folk (1958) pointed out that Zingg's diagram divided the classes of form unequally and suggested that rods were under-represented, and blades were over-represented. However, other researchers (Howard, 1992; Oakey et al., 2005) argued that the Sneed & Folk diagram produces a distortion by 'squeezing' bladed and rod-like forms into the bottom right-

hand corner of the diagram, subsequently, making these forms nearly indistinguishable. After generating a uniform distribution of artificial data (comprising elongation and flatness ratios) in the Zingg diagram, Blott & Pye (2008) showed that the same data appeared to compress blades and rods in the bottom right-hand corner of the ternary diagram, producing a non-uniform distribution (Figure 2-11).

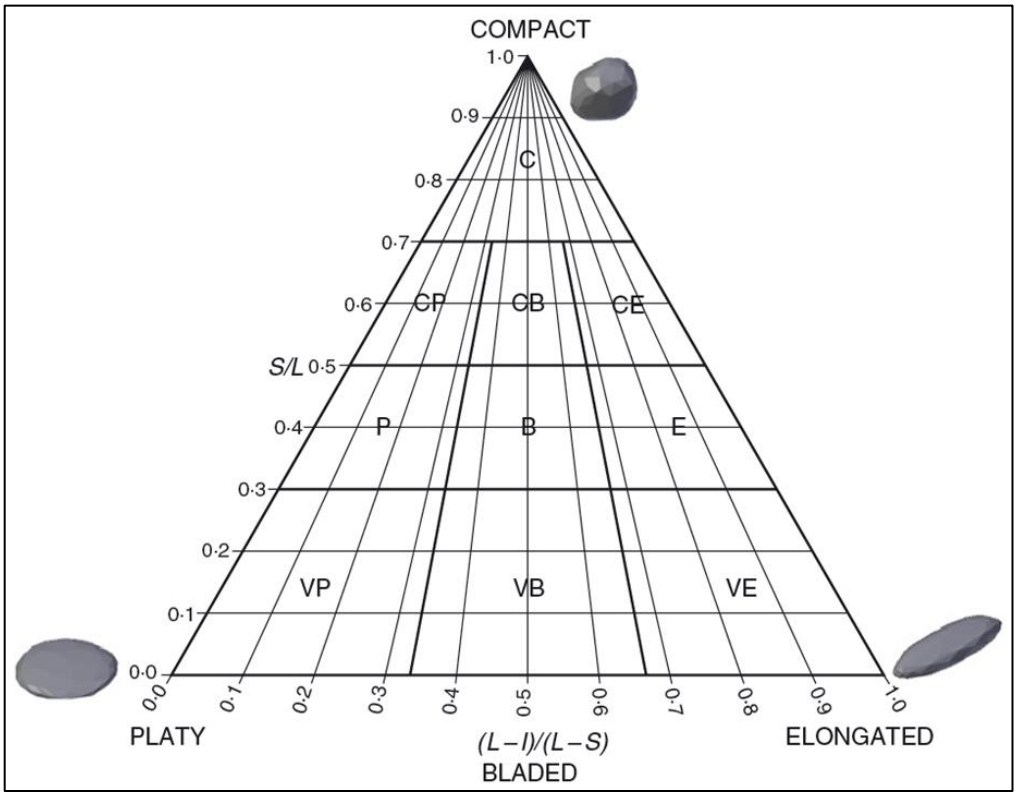



***Figure 2-10: Sneed & Folk (1958) ternary diagram comprising ten classes of form: C (compact), CP (compact-platy), CB (compact-bladed), CE (compact-elongated), P (platy), B (bladed), E (elongated), VP (very platy), VB (very bladed), VE (very elongated) (redrawn after Blott & Pye, 2008).***

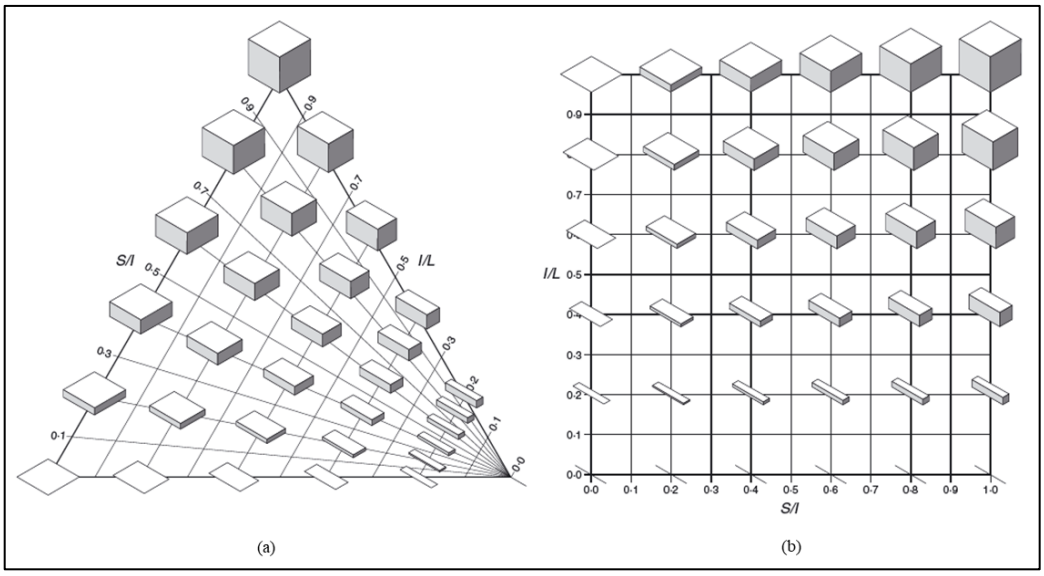



***Figure 2-11: 36 Forms plotted at regular geometric intervals to ensure even distribution of elongation and flatness ratios (a) Sneed & Folk diagram, (b) Zingg diagram (Blott & Pye, 2008).***

While Sneed & Folk's (1958) diagram emphasizes three extremes of form; combinations of L, I, and S compute four extremes of form which is consistent with the Zingg diagram (1935). Blott & Pye (2008) stated that "…*if particles are described by two independent properties of flatness and elongation, it is logical to deduce that there should be four end members*". These end members (i.e. extremes of form) are 'equant', 'platy (flat)', 'rod-like (elongated)', and 'bladed'. According to Blott & Pye (2008), "…*such a system is best plotted on a diagram with four corners (i.e. Zingg diagram)*".

## 2.3 Particle Shape: Angularity

The second level descriptor of shape, angularity, reflects the sharpness and number of edges and corners along a particle's outline. On the contrary, roundness is the average measure of the curvature of the corners and edges of a particle (Wadell, 1932; Janoo, 1998). The scale of surface features describing roundness is typically one order of magnitude smaller than the particle size (Cho et al., 2006). Some of the earlier works describing roundness originate from Wentworth (1919), Wadell (1932), and Krumbein (1941). Wadell's (1932) first formula for roundness, R, (Eq. 2-5) involved expressing the average curvature of all corners along a particle's outline as a ratio of the maximum inscribed circle within a particle's outline (Figure 2-12 a). According to Wadell (1932), a corner is defined as *"every such part of the outline of an area which has a radius of curvature equal to or less than the radius of curvature of the maximum inscribed circle of the same area*."

$$R = \frac{\sum \frac{r}{r'}}{N} \qquad \text{Eq. 2-5}$$

where r = radius of curvature of a corner along the particle's outline

r' = radius of the maximum inscribed circle within the particle's outline

N = number of corners

Wadell's (1932) method provides a very good measure of roundness but remains cumbersome, fairly complex and hence impractical for field applications. Krumbein (1941) developed a visual comparator to aid the

estimation of roundness of aggregates (Figure 2-12 b). Although, this chart can be scaled (i.e., enlarged or reduced) to suit the estimation of roundness for other sizes of aggregate, a degree of subjectivity can still be applied by the user. Limitations of this system relate to the absence of 3D features in the 2D particle silhouettes (Figure 2-12 b), a lack of descriptive terms of the 9 roundness classes, and a high number of classes which can lead to difficulties in assigning particles to certain roundness classes.

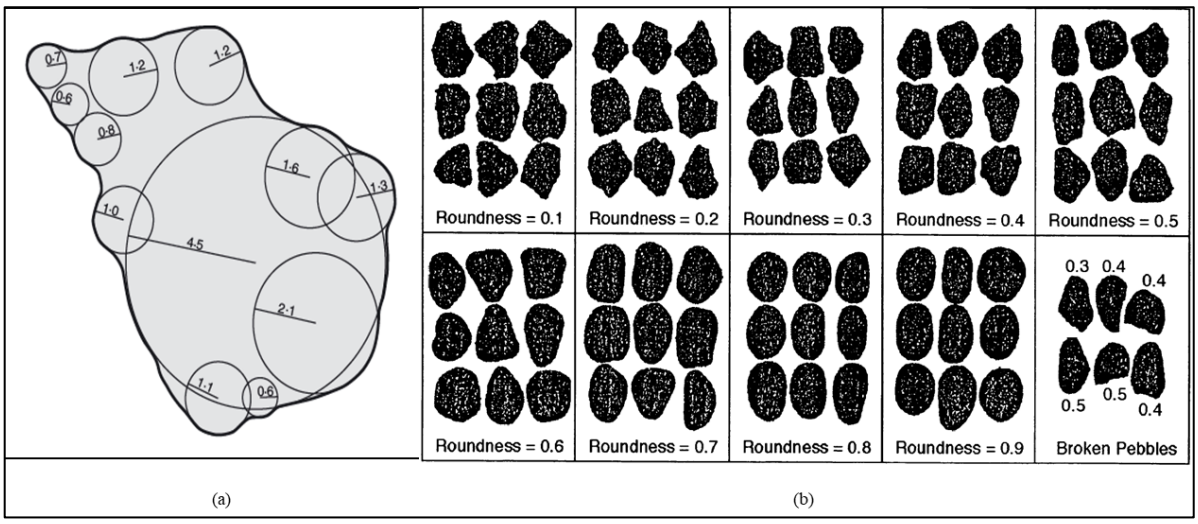



***Figure 2-12: (a) Schematic demonstrating the measure of roundness proposed by Wadell (1932), (from Blott & Pye, 2008). (b) Roundness chart for 16 – 32 mm aggregate, Krumbein (1941).***

Lees (1964 a, b) considered angularity as a concept distinct from roundness and proposed a method for computing the *degree of angularity* (A) *(*Eq. 2-6), that accounts for the relationship between two planes bounding a corner and the centre of the maximum inscribed circle (Figure 2-13 a and b).

$$A_i = (180^o - a)\frac{x}{r} \qquad \text{Eq. 2-6}$$

where $A_i$ = degree of angularity of corner i

α = apex angle of the two planes bounding the corner (Figure 2-13 a)

x = distance to the tip of the corner from the centre of the maximum inscribed circle

r = radius of the maximum inscribed circle

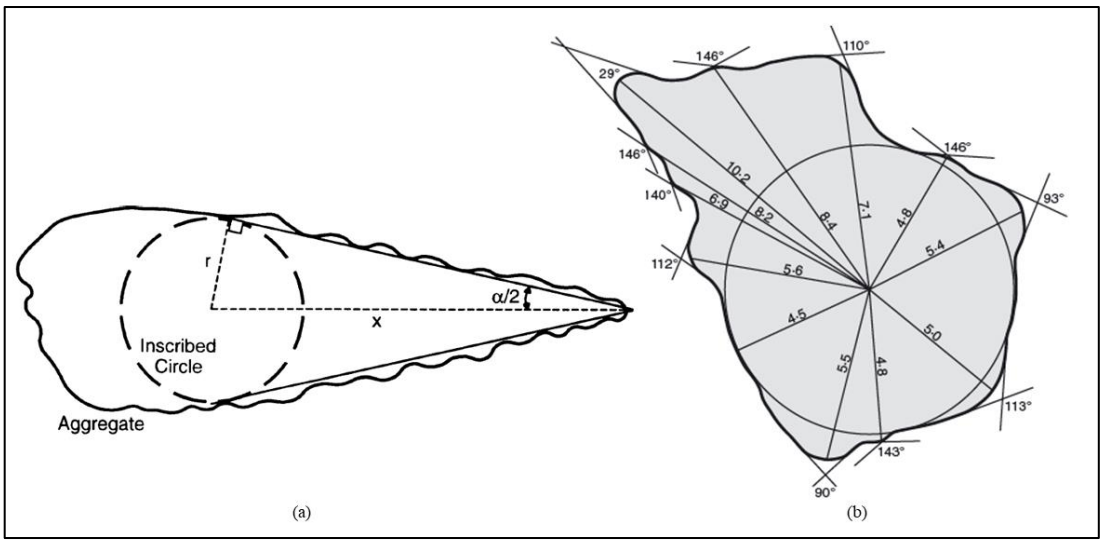



***Figure 2-13: (a) Parameters for determining the degree of angularity (After Lees, 1964), (b) Schematic indicating the measure of angularity of each corner on a projected plane (Blott & Pye, 2008).***

The total degree of angularity (A) is the sum of $A_i$ values calculated for all corners, measured along three orthogonal planes. Because of the method's complexity, Lees (1964 a, b) developed a visual comparator (Figure 2-14 a). For further simplification in characterizing angularity or roundness, ASTM D 2488-17E01 (2017): *Standard Practice for Description and Identification of Soils (Visual-Manual Procedure)* established qualitative

criteria for describing the angularity in coarse-grained particles (Figure 2-14 b and Table 2-2). This approach is practical for field applications.

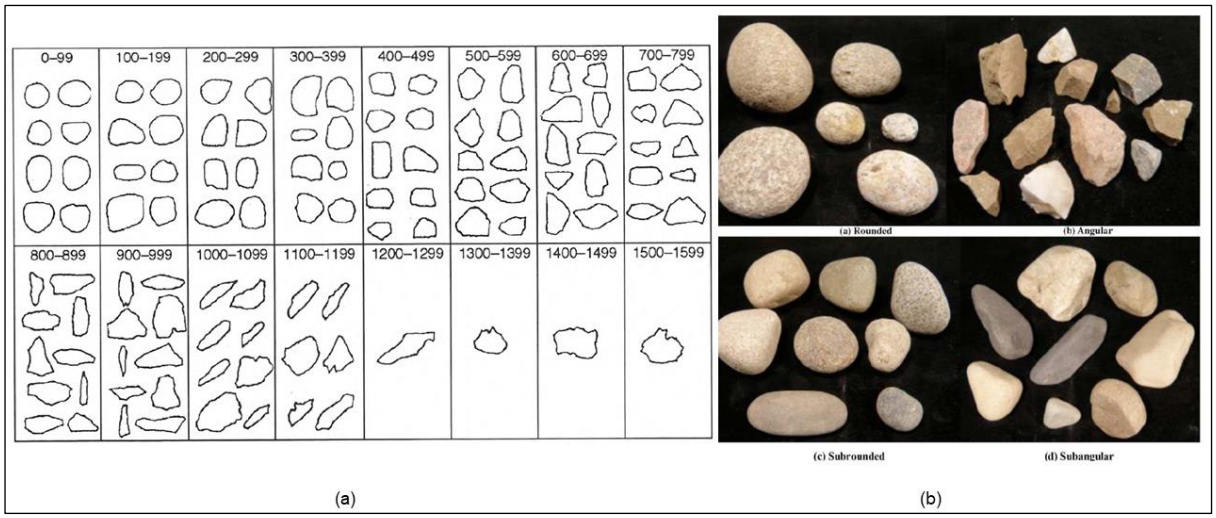



***Figure 2-14: Visual description for particle angularity, (a) Degree of angularity (After Lees, 1964), and (b) Visual identification of aggregate angularity (after ASTM D 2488-17E01, 2017).***

***Table 2-2: Criteria for describing angularity of coarse-grained particles from ASTM 2488-17E01 (2017).***

| Description | Criteria |
|---|---|
| Angular | Particles have sharp edges and relatively plane sides with unpolished surfaces. |
| Subangular | Particles are similar to angular particles but have rounded edges. |
| Subrounded | Particles have nearly plane sides but have well-rounded corners and edges. |
| Rounded | Particles have smoothly curved sides and no edges. |

Although 2D and 3D profiles of soil particles have been used to measure roundness, most methods remain either complex, time-consuming, or somewhat subjective (Le Pen et al., 2013). To measure and evaluate the influence of particle shape on a changing scale of size on crushed railway ballast, Le Pen et al. (2013) proposed a new measure for evaluating roundness, termed 'ellipseness'. Ellipseness (E) is defined as the ratio of the perimeter of a particle's 2D outline ($P_o$) to the perimeter of an equivalent area ellipse ($P_e$). Ellipseness can be easily computed using Eqs. 2-7 to 2-10. A limitation of the method pertains to how roundness is calculated based on a reference shape; the method does not explicitly define the relative sharpness of individual corners and edges along a particle's outline.

$$E = \frac{P_e}{P_o} \qquad where\ E \leq 1 \qquad \text{Eq. 2-7}$$

$$P_e \approx \pi\,(a+b)\left(1 + \frac{3\left(\frac{a-b}{a+b}\right)^2}{10+\sqrt{4-3\left(\frac{a-b}{a+b}\right)^2}}\right) \qquad \text{Eq. 2-8}$$

The major (a) and minor (b) radii are calculated using Eqs. 2-9 and 2-10, respectively:

$$a = \frac{L}{2} = \frac{D_{max}}{2} \qquad \text{Eq. 2-9}$$

$$b = \frac{A_o}{\pi a} \qquad \text{Eq. 2-10}$$

where $A_o$ = area of the particle

$D_{max}$ = longest line intersecting a particle's centroid of area, between two points situated on a particle's outline (Figure 2-5).

## 2.4 Measurement of Particle Shape: 3D Analysis

Advancements in contemporary technology have facilitated the use of X-ray micro-computed tomography (μCT) and laser scanning in generating 3D reconstructions of granular particles. These reconstructions of particles are used for the 3D characterization of shape. X-ray CT has been explored by various researchers (Fonseca, et al., 2012; Alshibli, et al., 2014; Zhao, et al., 2015; Zhou & Wang, 2016; Zhou, et al., 2017; Yu, et al., 2018; Liang, et al., 2021) for characterizing of particle shape. CT-based technology can also be used to reasonably compute volume, surface area, and the 3D (voxel) size of sand particles (Yu et al., 2018). A voxel is the three-dimensional analogue of a pixel and is related to both the pixel size and slice thickness of a 3D reconstructed particle.

Zhou et al. (2017) ornately outlined the important challenges pertinent to the calculation of morphological factors in granular particles. The authors summarised these challenges into two groups: one related to image analysis and computational geometry and the other relevant to the mathematical approach used to calculate the geometric properties based on a reconstructed particle surface. Firstly, according to Zhou et al. (2017), it remains a challenge to measure the reasonable particle surface area. To capture a particle's surface (i.e., voxel surface) from μCT images, a series of boundary voxels must be identified. A voxel-constructed surface is always characterized by a saw-tooth pattern and overlapping voxels (Zhou, et al., 2017). This results in an overestimation of the reasonable surface area, which adversely affects the accuracy of the sphericity of the particle. Zhou

et al. (2017) further state that "*it is also impossible to obtain the correct surface curvature and roundness of the particle from this kind of unsmooth surface*". Secondly, to reconstruct a particle's surface, surface smoothing must be implemented through a smoothing algorithm to simultaneously remove stair steps and preserve a particle's inherent morphology. According to Zhou et al. (2017), surface smoothing is dependent on the resolution of μCT images and the type of algorithm. Zhou et al. (2017) overcame this challenge by introducing spherical harmonic (SH) analysis to i) reconstruct a particle's surface and ii) characterize particle shape.

The use of laser scanning for the 3D analysis of particle morphology is well-documented for gravel-sized particles (Lee et al., 2007; Sun et al., 2014; Mgangira et al., 2013; Nie et al., 2018; Cruz-Matías et al., 2019). Mgangira et al. (2013) used 3D laser scanning technology to quantify and characterize the morphology of andesite aggregates, varying between 13.2 and 19 mm in size, as part of an extensive investigation aimed at linking aggregate shape parameters to the performance of pavement materials. The main advantage of using 3D laser scanning, highlighted in this study, pertained to the direct acquisition of surface texture, volume, and surface area from a particle's 3D (mesh) model. On the other hand, due to the limiting attainable pitch size (i.e. resolution), the technology is preferred for gravel-sized particles.

Le Pen et al. (2013) stated that issues related to the interpretation of data obtained from μCT and laser scanning were mainly connected to the relative *particle-to-pixel* (or voxel) size. In addition, both μCT and laser scanning

present physical limits on the sizes of the samples that can be scanned and the resolution which can be achieved (Le Pen, et al., 2013). Some of the most important disadvantages associated with μCT or laser scanning are that these technologies are not readily available to practitioners and researchers, and secondly, they remain costly in terms of both time and money (Le Pen et al., 2013; Eddey et al., 2019).

## 2.5 Significance of Particle Shape

Under static loading conditions, Holtz & Kovacs (1981), studied the effects of void ratio, angularity, surface roughness, and moisture content, amongst other parameters, on the mechanical behaviour of aggregates. It was largely concluded that an increase in the internal angle of friction correlated with increases in particle angularity and surface roughness. Intuitively, smooth and rounded particles promoted sliding behaviour, whereas angular particles elicited a better degree of interlocking (inhibiting particle mobility), ultimately contributing to greater frictional strength. Under the same conditions, at particle contact interfaces, angular particles must overcome greater frictional forces, before sliding can commence (Janoo, 1998). A similar finding - observed by Shin & Santamarina (2013) - stemmed from an increase in the mass fraction of angular particles in mixed sand (consisting of round and angular particles) that correlated to an increase in the friction angle of the granular mixture.

Cho et al., (2006) examined the effects of particle shape on packing density and on the small-to-large strain mechanical parameters of crushed and natural sands, using two databases. These databases were compiled using published data and new experimental data. Cho et al. (2006) explored and presented correlations between index properties (sphericity, roundness, and regularity) and different mechanical properties influenced by particle shape. An increase in particle angularity and irregularity (i.e. decrease in sphericity and roundness) correlated to:

- an increase in the minimum and maximum void ratios, accompanied by an increase in the difference between the minimum and maximum void ratios ($e_{max} - e_{min}$).
- an increase in the compressibility index, $C_c$, (under zero-lateral strain loading).
- a reduction in small-strain stiffness; coupled with increased sensitivity to the state of stress.
- increase in the (constant volume) critical state friction angle *($\phi_{cs}$)*

The effect of particle shape on small-strain stiffness was evaluated (in natural and crushed sands) by transmitting and measuring shear waves through each soil specimen, fitted in an oedometer cell, using *bender* elements. Shear wave velocities were consistently measured during loading and unloading cycles. In the case where the behaviour of (rounded and spherical) ASTM 20/30 sand ($D_{50}$ = 0.6 mm; $\phi_{cs}$ = 32°; $e_{max}$ = 0.69; $C_c$ = 0.0038) and (angular and irregular) crushed sand ($D_{50}$ = 0.48 mm; $\phi_{cs}$ = 41°;

$e_{max}$ = 0.86; $C_c$ = 0.0088) was compared, it was shown that - over the same loading conditions - the crushed sand experienced greater deformation over a stress range from 1 kPa to 500 kPa. Moreover, the crushed sand exhibited higher compressibility, particularly between 100 kPa and 500 kPa. And of equal importance, the change in the response time of the shear wave velocity in crushed sand was significantly greater compared to ASTM 20/30 sand during the entire loading cycle. The reduction in packing density contributed substantially to the increase in shear wave velocity. Hence, Cho et al. (2006) concluded that a reduction in sphericity, roundness, and regularity was accompanied by a reduction in the shear wave velocity (α) and increased sensitivity of the shear wave velocity to the change in the mean effective stress.

Cho et al. (2006) highlighted that *irregular* (shaped) particles promoted a lower coordination number and looser packing states – which was supported by evidence depicting the increase in the extreme void ratios ($e_{max}$ and $e_{min}$) with increasing particle irregularity and angularity. A lower coordination number can result in a looser packing state (i.e. void ratio) (Santamarina & Cho, 2004).

The quantitative assessment of the multi-scale shape parameters has proven to be invaluable in enhancing our understanding of the influence of shape on the mechanical behaviour of granular matter. According to Cho et al (2006), each scale parameter (emanating from particle shape) "…*reflects aspects of the formation history and participates in determining the global behaviour of the soil mass from particle packing to mechanical response*".

This, so assuredly, underpins the need for researchers and practitioners to reasonably measure and characterize particle shape.

## 2.6 Summative Discussion

The quantification of 3D form using the flatness and elongation ratios aids form characterisation based on four classes of form: i) discoid (flat and platy), ii) bladed (flat and columnar), iii) rod-like (elongate) and iv) equant (spheroid and cuboid). Hence, quantifying form using these two ratios has advantages over other descriptors that fail to adequately differentiate various classes of form. These classes exhibit different mechanical behaviours. For example, bulky particles mixed with platy particles of the same size cause a significant increase in the void ratio, accompanied by an increase in compressibility and a reduction in shear strength (Clayton et al., 2009). Selig & Waters (1994) also reported that 'flaky' (i.e. flat and platy) particles (used for railway ballast) appeared to i) increase abrasion and breakage, ii) increase permanent strain accumulation under repeated loading and iii) decrease stiffness. Regarding railway ballast, cubic (i.e. equant: cuboid) particles are preferred over elongated and 'flaky' particles, as they ensure a degree of particle interlocking that promotes a stable and strong railway ballast profile (Li et al., 2015; Mvelase et al., 2022).

Compared to gravels, obtaining the three principal dimensions S, I and L presents difficulties in sand-sized particles, especially in fine sediment. That is, securing these particles to a base to measure their principal dimensions along three-orthogonal views becomes difficult and time-consuming. The sophisticated technology used to characterise sand-sized particles such as

X-ray micro-computed tomography is expensive and not readily accessible to researchers and practitioners. Hence, regarding research objective 1, focus variation microscopy is investigated as an alternative cost-effective, accurate and relatively quick method for facilitating the quantification of 3D form in sand-sized particles.

Furthermore, research objective 2 aims at evaluating the variability of angularity along three-orthogonal views (in sand-sized particles) to investigate the efficacy with which particle angularity can be characterized using a single 2D projection. Hence, precluding the need to rotate particles to three-orthogonal views and therefore ensuring the rapid assessment of angularity in sands, using an angularity descriptor termed 'ellipseness'.

Despite the introduction of visual comparators in facilitating the rapid assessment and characterization of angularity (or roundness), there remain ambiguities in assigning roundness classes, particularly in systems that have a high number of roundness classes. Furthermore, visual comparators that make use of particle silhouettes, instead of 3D models or photographs, present more difficulties (to the end-user) in assigning a representative roundness class because 3D information, such as out-of-plane angularity features, is absent in silhouettes. Research objective 3 aims to i) characterize the angularity descriptor, ellipseness, using roundness classes proposed by Blott & Pye (2008), and ii) investigate the efficacy with which this easily computable descriptor can distinguish between various degrees of roundness using Wadell's (1932) roundness index, R.

# 3 TEST PROCEDURE DEVELOPMENT

This chapter describes the materials adopted for the experiment, the instrument and procedure used to perform the focus variation procedure and lastly, the procedures implemented for measuring the form and angularity in the granular particles included in each of the assessments.

## 3.1 Materials

The experimental program (Table 3-1) assessed 283 granular particles from the matter shown in Figures 3-1 to 3-5. Two beach sands were sourced from West Bank beach (East London, South Africa) and Ballito beach (Dolphin coast, situated approximately 40 km north of Durban, South Africa), respectively. The beach sands are examples of natural sands resulting from weathering and pulverization of rock matter over millions of years, and whose angularity typically varied from subrounded to rounded. The platinum tailings sand originated from a mine in the North-West province of South Africa and is an example of industrial waste. Crushed quartz sand (i.e., silica sand) is commonly used in swimming pool filters and is a constituent in glass products. Based on their visual assessment under an optical microscope, platinum tailings and quartz sand typically appeared subangular to angular. Lastly, to include a material of extreme roundness, commercially manufactured spherical glass beads, commonly used for retroreflective materials in building facades, were explored.

***Table 3-1: Summary of the experimental program.***

| Material | No. of assessments by type† | | | |
|---|---|---|---|---|
| | Validation: Focus Variation | Form Assessment | Ellipseness Assessment | Ellipseness Assessment against Wadell's (1932) Roundness Index ‡ |
| West Bank beach sand (WBS) | 50 | 50 | 25 | 15 |
| Ballito beach sand (BBS) | 50 | 50 | 50 | 15 |
| Crushed quartz sand (CQS) | 50 | 50 | 30 | 10 |
| Platinum tailings sand (PTS) | 50 | 50 | 50 | 10 |
| Glass Beads (GBS) | 20 | 20 | 20 | 10 |

**† Generally, more than one assessment was performed on a single particle, except in the case of ‡**

**‡ Assessment performed on 60 particles. Assessment of ellipseness against Wadell's (1932) roundness index, calculated using Wadell's (1932) first formula (Eq. 2-5), in the plan-view projection only. Particles used in this assessment were not considered in the other assessments.**




***Figure 3-1: Photomicrograph of West Bank beach sand.***




***Figure 3-2: Photomicrograph of Ballito beach sand.***

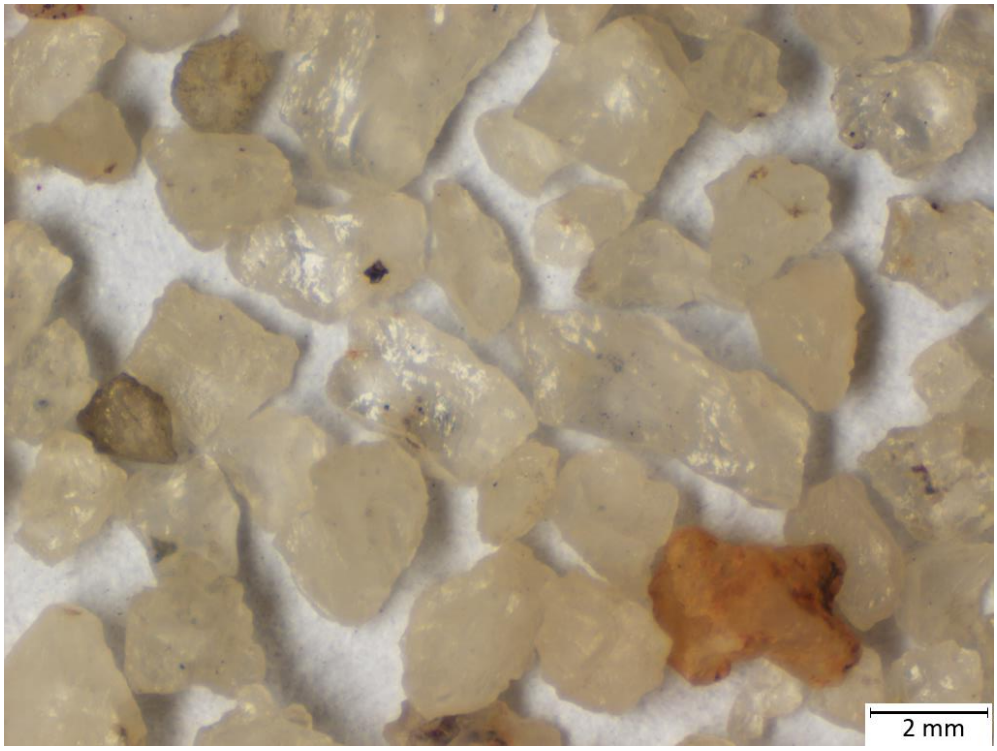



***Figure 3-3: Photomicrograph of crushed quartz sand.***

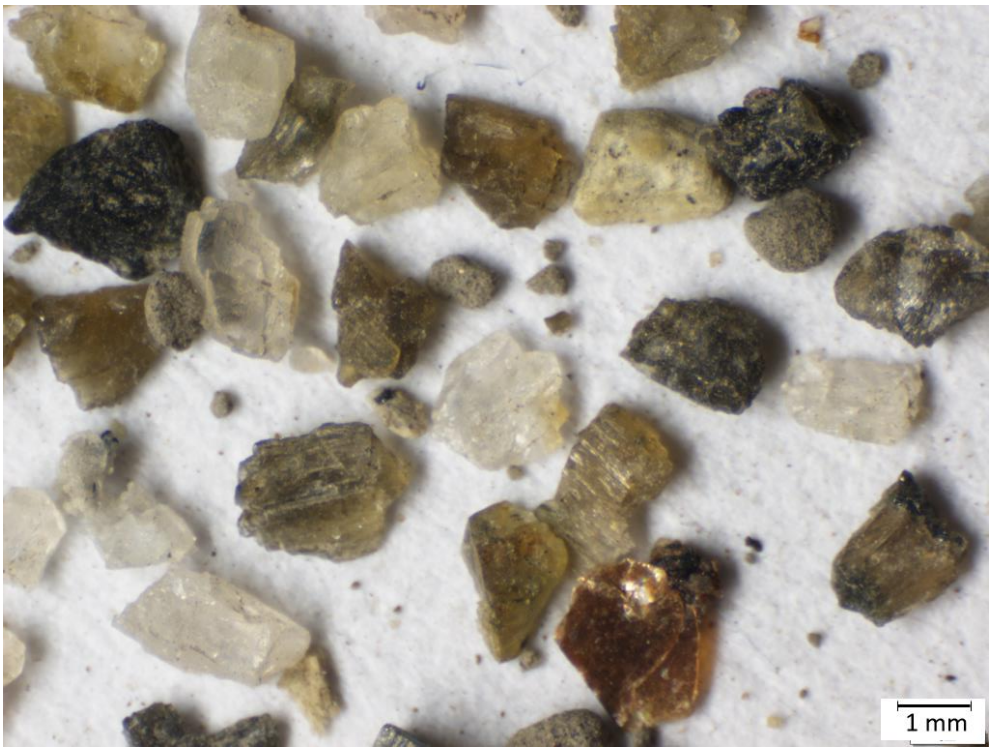



***Figure 3-4: Photomicrograph of platinum tailings sand.***

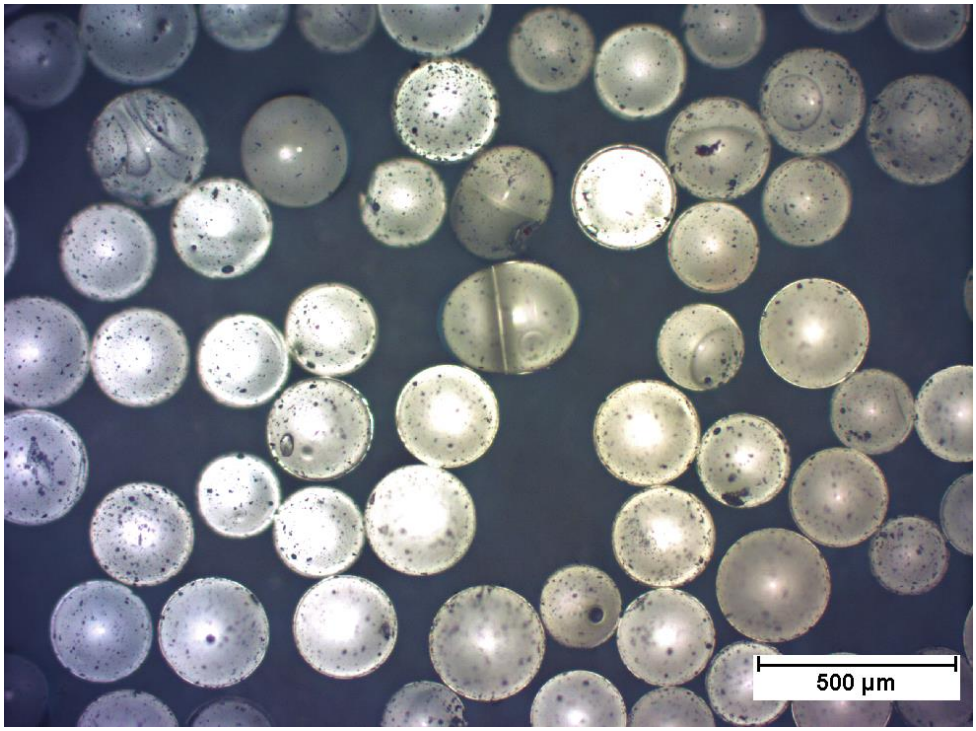



***Figure 3-5: Photomicrograph of glass beads.***

## 3.2 Particle Size Gradation

All particles analysed passed the 2360 µm sieve but were retained by the 75 µm sieve. To ensure a uniform distribution of data points, across the prescribed size range, each material was sieved using BS 410-1986 sieves configured in the following order (from top to bottom): 2360 µm; 1180 µm; 600 µm; 300 µm; 150 µm; 75 µm. A metallic retaining pan was fitted at the bottom of the sieve configuration to retain fine particles passing the 75 µm sieve. For each material type, particles retained on a specific test sieve were separately stored.

## 3.3 Focus Variation (FV) Microscopy

ISO 25178-606 (2015) defines focus variation (FV) microscopy as a "*surface topography measurement method whereby the sharpness of the surface image (or another property of the reflected light at optimum focus) in an optical microscope is used to determine the surface height at each position along the surface."* FV performs height measurements by searching for the optimum focus position of an optical element pointing to a sample (Figure 3-6) (Helmli, 2011). According to Helmli (2011), the four fundamental components of a typical FV instrument (Figure 3-6) include:

- An optical system with a limited depth of field (DoF)
- An illumination device or source
- An image sensor to detect focus (such as a charge-coupled device, CCD, or complementary dry metal oxide semiconductor, CMOS, sensor)
- A driving unit for focus search

In this study, the z-axis was defined, following ISO 25178-6 (2010) and ISO 25178-606 (2015), as the axis parallel to the optical axis and perpendicular to the (x, y) plane for an optical instrument. ISO 10934 (2020) defines the DoF (Figure 3-7) as the "*axial depth of the space on both sides of the object plane within which the object can be moved without detectable loss of sharpness in the image, while the positions of the image plane and of the objective are maintained."* The smaller the objective's numerical

aperture (NA), the smaller the opening through which light travels through the lens and the wider the DoF (Figure 3-7).

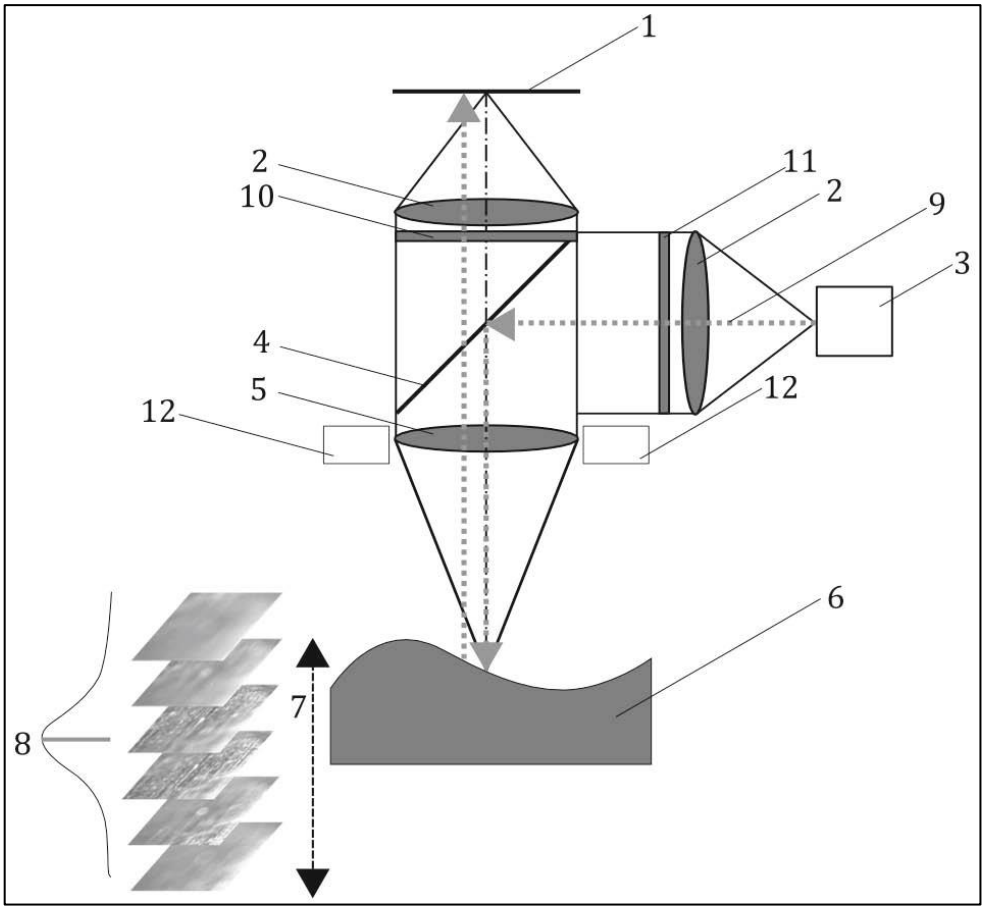



***Figure 3-6: Schematic diagram of a typical measurement device based on focus variation: (1) CCD sensor, (2) lenses, (3) white light source, (4) semi-transparent mirror, (5) objective lens with limited depth of field, (6) sample, (7) vertical movement with driving unit, (8) contrast curve calculated from the local window, (9) light rays from the white light source, (10) optional analyser, (11) optional polarizer and (12) optional ring light (from Helmli, 2011).***

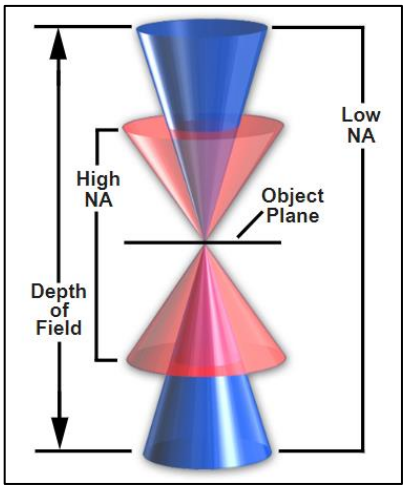



***Figure 3-7: Depth of field ranges, where NA = numerical aperture (https:// www.microscopyu.com/microscopy-basics/depth-of-field-and-depth-of-focus).***

The experiment was conducted using a Nikon Optiphot-Pol optical microscope (Figure 3-8), with a limited DoF. The optical path of the microscope is shown in Figure 3-9 a. Illumination from the epi-illuminator was used for photomicrography and to perform the FV procedure. ISO 10934 (2020) defines an epi-illuminator as "*part of the illuminating system of the reflected light microscope placed between the objective and the lamp fitting*." Hence, this system was installed between the intermediate tube "P" and the microscope arm supporting the nosepiece, to which the CF Achromat objective lenses were fixed (Figure 3-9 a and b). This system was powered by a 12-Volt, 50-Watt Halogen lamp, that helped ensure a bright and uniform field.

The microscope was fitted with 4 objectives providing magnifications of 5x, 10x, 20x, and 40x, respectively. An ocular lens, fitted to the eyepiece of

the microscope, provided an additional 10x magnification. For detecting focus, a 2592 x 1944 active CMOS (DFK 72AUC02) sensor (Figure 3-10) was fitted to the top of the micro flex tube and connected to a desktop computer. Commercially available NIS-Elements 4.0 (version D) software was used to acquire micrographs and perform measurements on particles (Figure 3-11). The microscope's objectives were calibrated to the software using a certified stage micrometre. At each magnification, the DoF was estimated using the formula (Eq. 3-1) from Inoué and Spring (1997). The NA, approximated DoF, and pixel density associated with each objective are summarised in Table 3-2.

$$Depth\ of\ Field = \frac{\lambda_0 n}{(NA)^2} + \frac{n}{M(NA)}(e) \qquad \text{Eq. 3-1}$$

Where

$\lambda_0$ = wavelength of the illuminating light, for which a characteristic value of 0.55 μm (for visible light) was used

n = lowest refractive index of the medium through which the sample is being viewed and is equal to 1.00 for air

NA = numerical aperture of the objective

M = magnification of the objective lens

e = the smallest distance that can be resolved by a detector that is placed in the image plane of the microscope objective whose lateral magnification is M (Spring & Davidson, 2022). In video microscopy, e is equal to the pixel

spacing of the camera (Goodwin, 2015). The CMOS sensor used in this study had a pixel spacing of 2.2 µm.

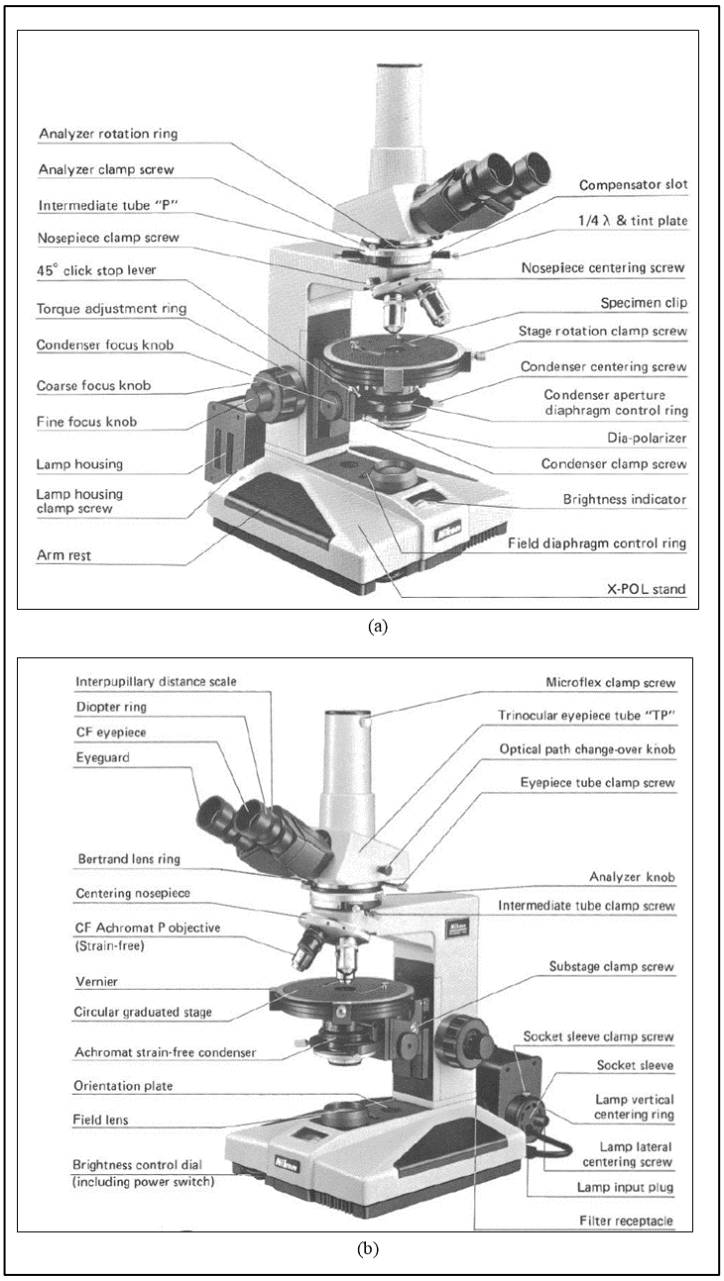



***Figure 3-8: Illustration of Nikon Opti-phot Pol optical microscope, without epi-illumination system, (a) left view; (b) right view (OPTIPHOT-POL Instruction Manual).***

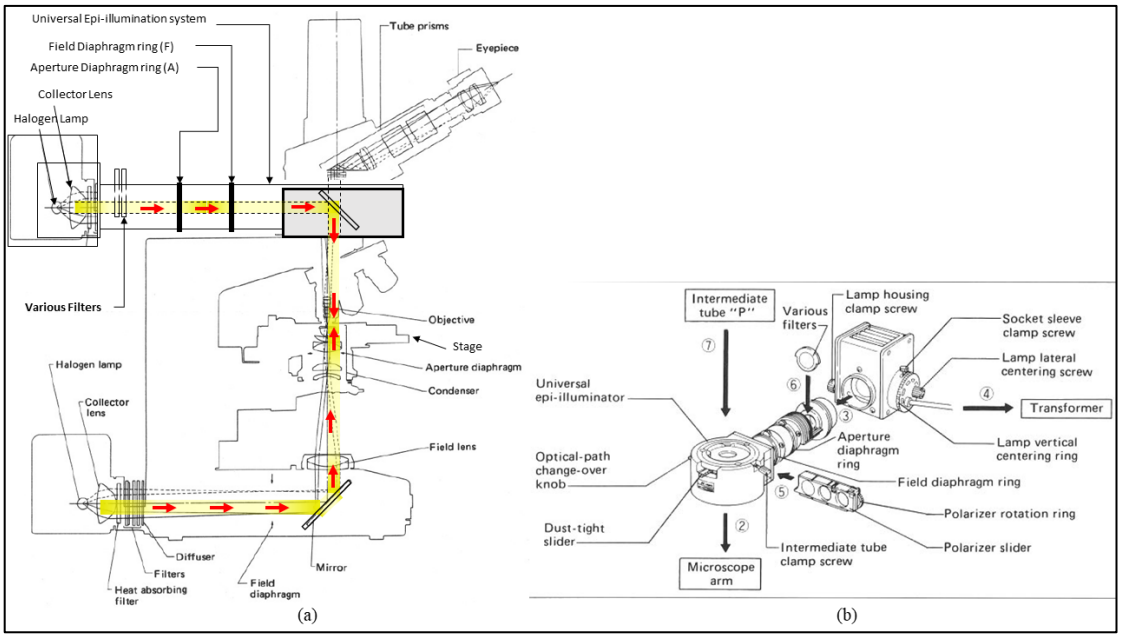



***Figure 3-9: (a) Optical path of the Nikon Opti-phot Pol optical microscope; (b) Universal epi-illuminator (OPTIPHOT-POL Instruction Manual).***

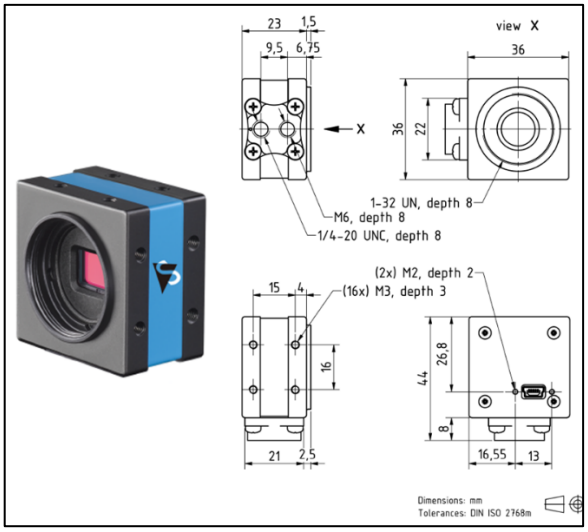



***Figure 3-10: DFK 72AUC02 CMOS Sensor (https://www.theimagingsource.com/products/industrial-cameras/usb-2.0-color/dfk72buc02/).***

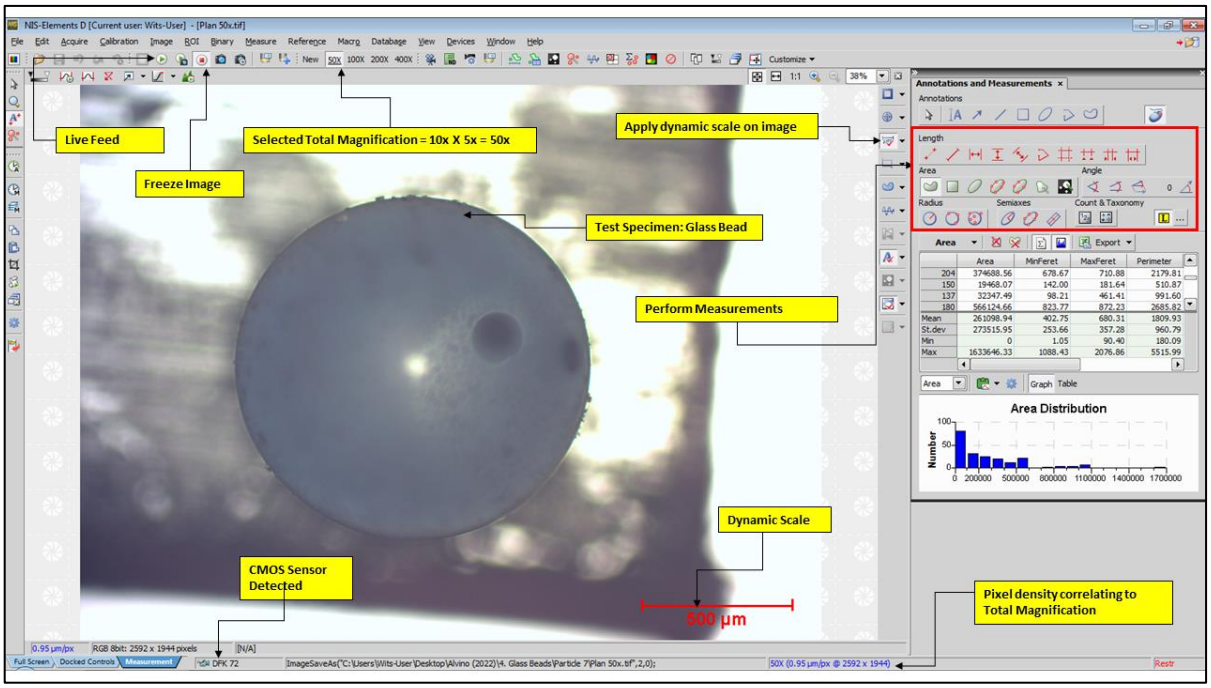



***Figure 3-11: Graphic user interface of NIS-Elements software (NIS Elements D, Nikon).***

***Table 3-2: NA, approximated DoF and pixel density for each objective.***

| Objective | NA[1] | Pixel Density[2] (µm/px) | Approximated DoF (µm) |
|---|---|---|---|
| 5x | 0.10 | 0.95 | 59.40 |
| 10x | 0.25 | 0.48 | 9.68 |
| 20x | 0.40 | 0.24 | 3.71 |
| 40x | 0.65 | 0.12 | 1.39 |

**[1] specified by Nikon™, for 'dry' objectives**

**[2] values were obtained from NIS Elements D software after calibration to the CMOS sensor and microscope**

## 3.4 Focus Variation (FV) Procedure

Figure 3-12 shows the configuration of the FV instrument used in this study. An analog dial indicator, with a 1 μm resolution, was used to measure vertical displacements of the microscope's stage during the FV procedure. The FV procedure is described below:

1. The adjustments made to the microscope included:
    a. ensuring that the objective lenses were centered, clean, and secured to the nosepiece.
    b. adjustments of the eyepiece (interpupillary distance) were made when required.
    c. selection of the necessary filters for epi-illumination.
    d. adjustment of the ¼ λ & tint plate (in the compensator slot).
    e. adjustment of the aperture and field diaphragm when required.
    f. ensuring that the analyser was brought into the optical path.
2. The *live feed* (prompt) within NIS-Elements' GUI was selected.
3. The computer monitor was observed to confirm whether the CMOS sensor detected the sample, through the objective lens, by adjusting the microscope's stage.
4. The magnification corresponding to the selected objective and scale were also selected within the software's GUI.
5. The rigid frame and magnetic base of the dial indicator were then secured adjacent to the microscope – with the dial face directed towards the user.

6. Three levels along the dial indicator establishment were checked using a spirit level: i) the horizontal level along the cantilever arm supporting the dial indicator; ii) the vertical level parallel to the back casing of the dial indicator and iii) the vertical level orthogonal to the back casing of the dial indicator.
7. As soon as the dial indicator was level, it was slowly moved into position above the microscope's stage, whilst ensuring that it did not contact the objective lenses or centering nosepiece, especially during the rotation of the nosepiece.
8. Each group of particles passing a specific sieve and retained on the subsequent sieve was separately handled and carefully dispersed onto a flat clean, hard surface.
9. Particles from each size group were randomly selected for testing.
10. The base was cleaned using an alcohol-based sanitizing agent before a particle was secured to it using adhesive liquid glue.
11. Each particle was secured to a prismatic base.
12. The base rested on a transparent (46 x 26 x 0.17 mm thick) cover glass slide, that spanned across a small opening above the condenser, on the microscope's stage.
13. The particle was brought into sharp focus using the coarse and fine focus adjustment knobs.
14. Illumination was regularly adjusted during this procedure.
15. The uppermost tip of the particle was detected - by observing a live feed from a computer monitor - and brought into sharp focus.

16. The eyepiece was also used to confirm the view displayed on the computer monitor.
17. The initial reading on the dial indicator was recorded once the uppermost tip of the particle was in sharp focus.
18. Adjustments of the microscope's coarse and fine focus knobs causes vertical stage displacements (SD) in the z-direction. The fine focus knob was slowly adjusted by moving the stage up until the base's surface was in sharp focus and the particle was out of focus.
19. The texture of the base's surface was well-defined (i.e., comprising contrasting features). That is, the base adopted for the experiment exhibited unique surficial microscopic striations which easily contrasted the particle's outline.
20. After the base's surface was in sharp focus, the final reading on the dial indicator was recorded.
21. The particle height ($D_{\Delta f}$) was calculated as the difference between the initial and final readings recorded from the dial indicator.
22. The particle was then orthogonally rotated to two lateral views.
23. In each lateral view, the particle's outline was brought into sharp focus.
24. This facilitated the measurement of the particle height (using a *parallel line*-enabled drawing tool in NIS Elements*)* from the top of the base to the uppermost tip of the particle in each lateral view (Figure 3-13). The particle's height in each lateral view was denoted as $D_{L1}$ and $D_{L2}$, respectively.

25. Figure 3-14 indicates the position of the objective relative to the particle and the stage at the start and end of the FV procedure. Figure 3-15 illustrates the FV procedure in plan-view, performed at a total magnification of 100x.

26. For the validation of the FV procedure: the mean height of two-orthogonal lateral views, denoted as $D_L$, was computed using Eq. 3-2 and subsequently compared to $D_{\Delta f}$. Furthermore, in this study, the measurement error was expressed as the difference between the mean particle height, $D_L$, and the particle height inferred using FV, $D_{\Delta f}$ (Eq. 3-3).

$$D_L = \frac{D_{L1}+D_{L2}}{2} \quad \text{Eq. 3-2}$$

$$Error = D_L - D_{\Delta f} \quad \text{Eq. 3-3}$$

Positive and negative errors were indicative of height underestimation and overestimation, respectively. The mean underestimation and overestimation errors were computed using Eq. 3-4 and 3-5, respectively.

$$Mean\ underestimation\ error = \frac{Sum\ of\ all\ positive\ errors}{\Sigma(n1)} \quad \text{Eq. 3-4}$$

$$Mean\ overestimation\ error = \frac{Sum\ of\ all\ negative\ errors}{\Sigma(n2)} \quad \text{Eq. 3-5}$$

Where Σ(n1) = sum of readings associated with positive errors and Σ(n2) = sum of readings associated with negative errors.

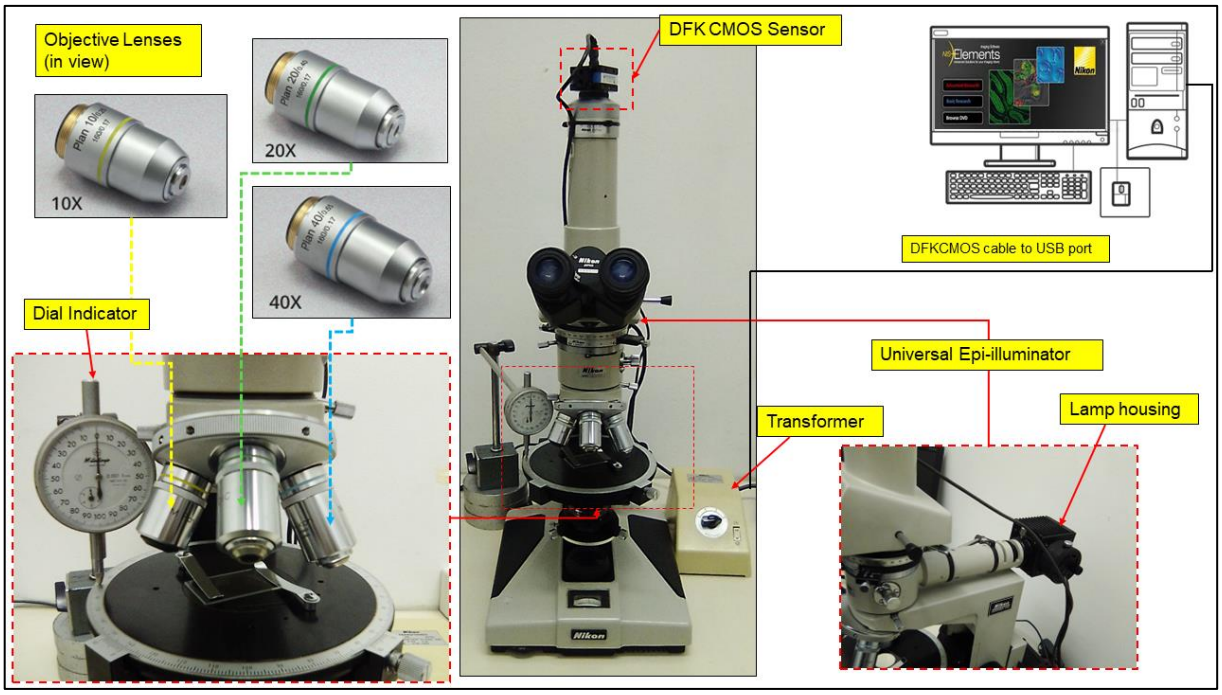



***Figure 3-12: Establishment of the focus variation instrument.***

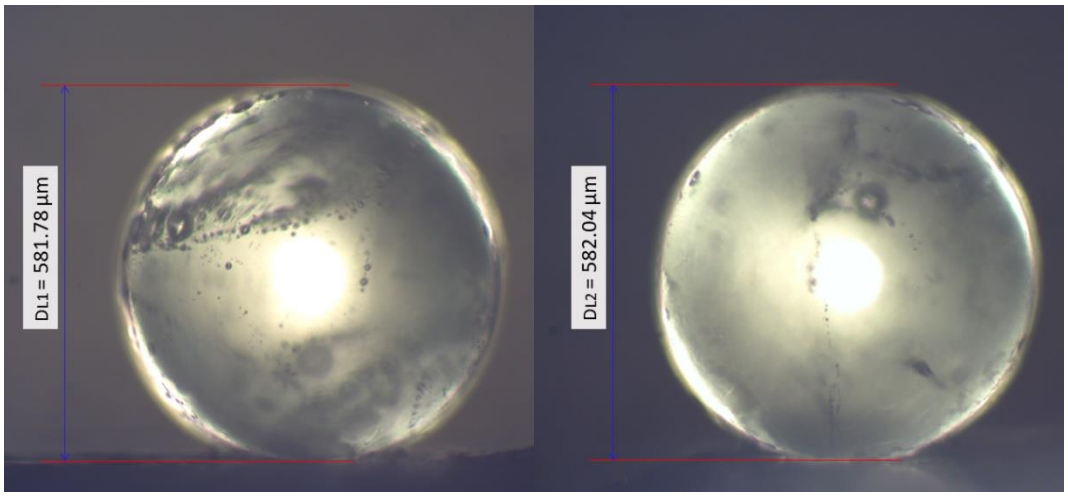



***Figure 3-13: Measurement of particle height from two lateral views, on a glass bead particle.***

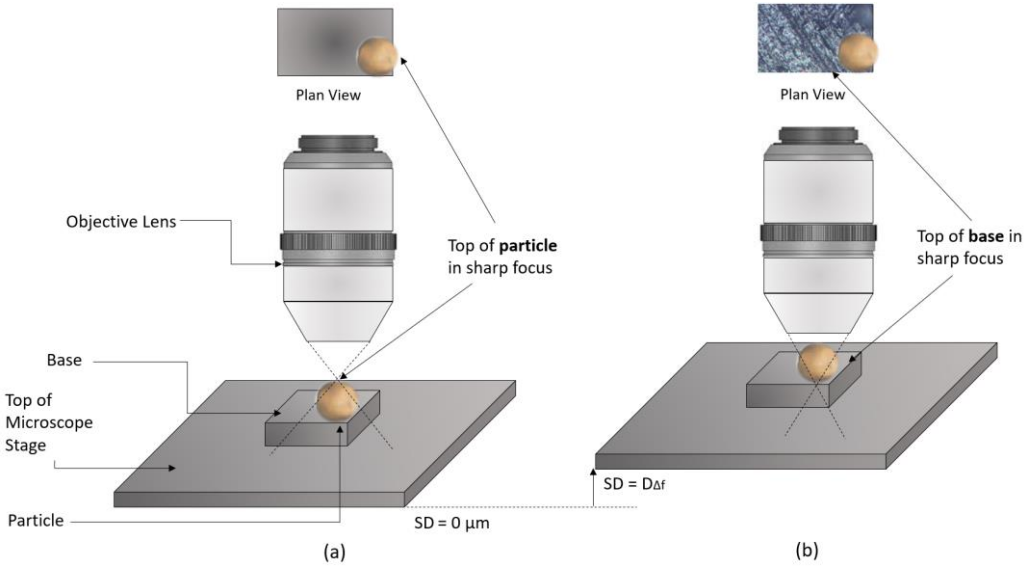



***Figure 3-14: (a) start of FV procedure, (b) end of FV procedure.***

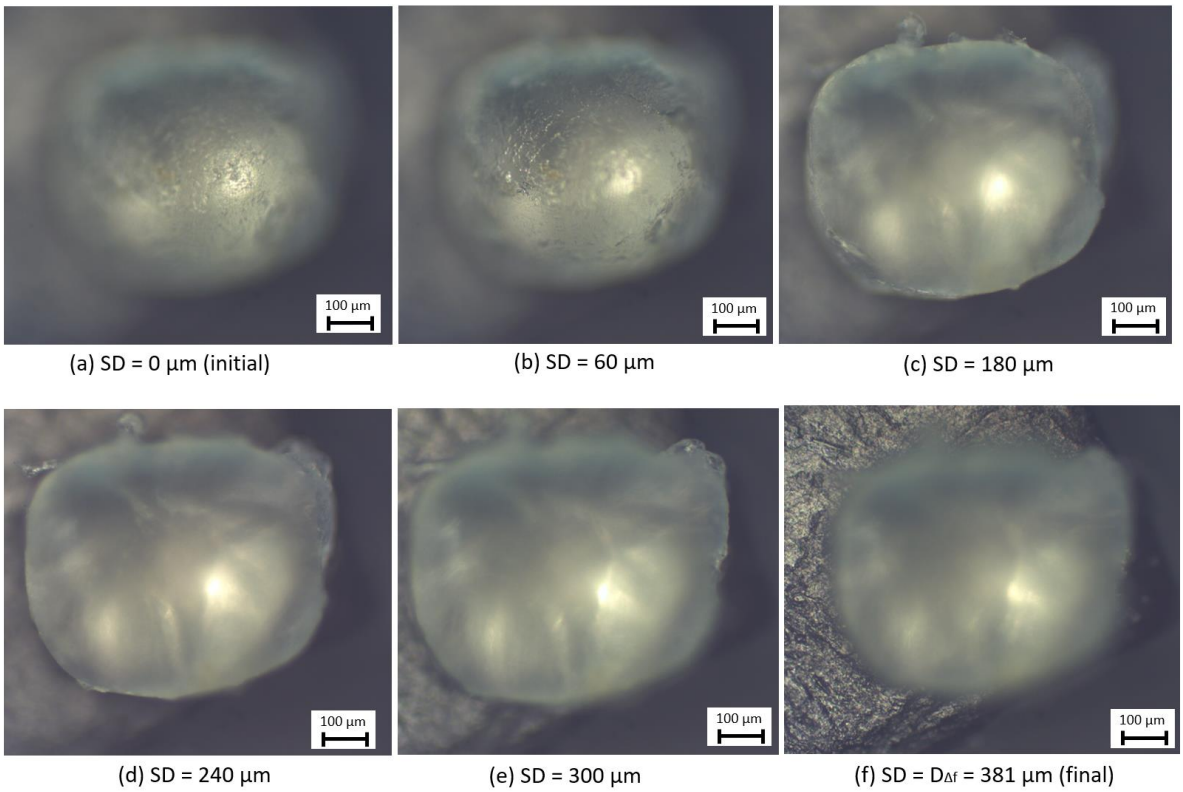



***Figure 3-15: The focus variation procedure performed at 100x magnification on a West Bank beach sand particle.***

### 3.5 Form Measurement

In this study, the measurements of S, I and L were simplified to how a particle exhibits its maximum projection area to the observer in plan view when dispersed onto a flat surface (which was discussed in 2.1). In plan view, L was assumed to be equal to the diameter of the minimum circumscribed circle ($D_{cc}$) and I was assigned the value of the maximum inscribed circle ($D_{ic}$), and S = $D_{\Delta f}$, provided S ≤ I ≤ L. However, if I (= $D_{ic}$) was smaller than S (= $D_{\Delta f}$), then S, I, and L were re-assigned to satisfy the inequality: S ≤ I ≤ L. Figure 3-16 shows how $D_{cc}$ and $D_{ic}$ were measured on a micrograph of a Ballito beach sand particle.

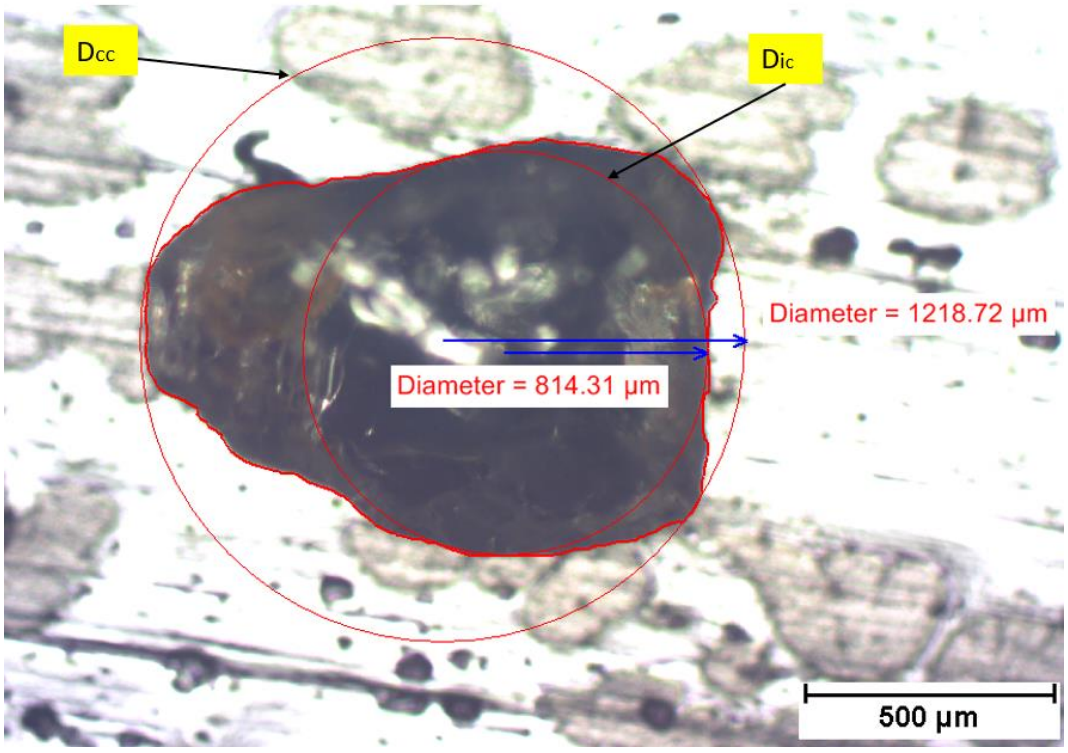



***Figure 3-16: Measurement of $D_{ic}$ and $D_{cc}$, in plan view at 50x magnification on a Ballito beach sand particle.***

### 3.6 Angularity Measurement

Particle angularity, defined by ellipseness, was calculated using Eqs. 2-7 to 2-10. Hence, research objective 2 entailed:

1. Assessing the ellipseness of particles considered for FV.
2. The measurement of the area ($A_o$), perimeter ($P_o$) and $D_{max}$ along the particle's outline in plan view (Figure 3-17).
3. The orthogonal rotation of the particle to the first lateral view in which measurements of $A_o$, $P_o$ and $D_{max}$ were made.
4. The subsequent orthogonal rotation of the particle to a second lateral view in which measurements of $A_o$, $P_o$ and $D_{max}$ were also performed.

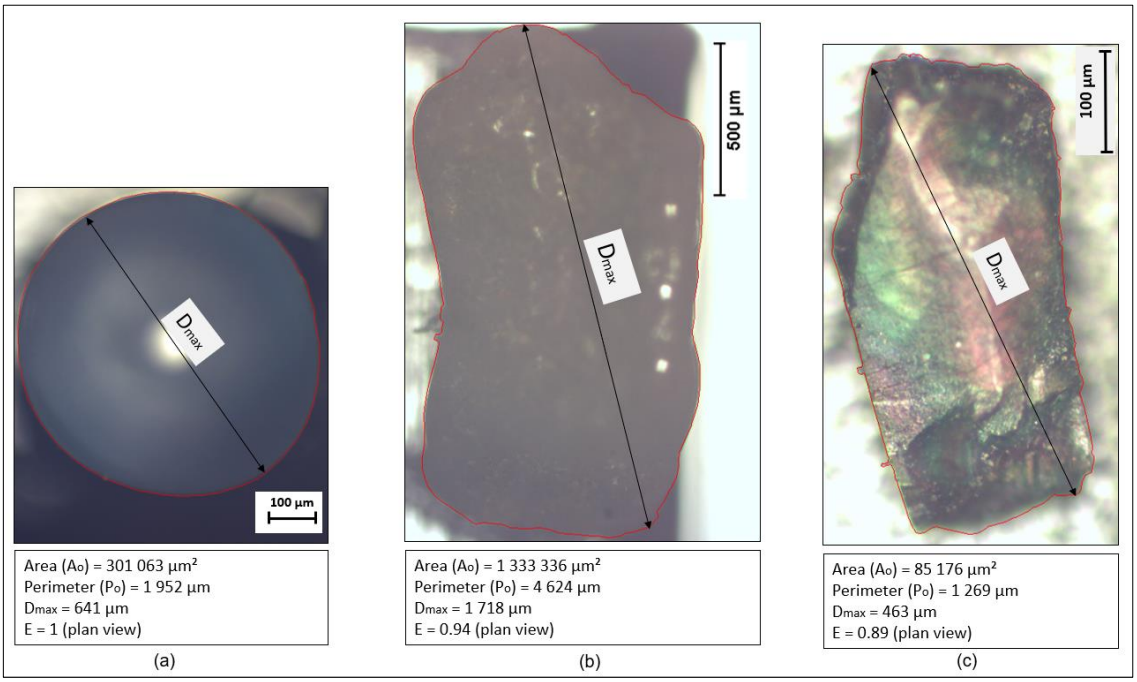



***Figure 3-17: Parameters used to compute ellipseness in plan-view: (a) glass bead, (b) Ballito beach sand, and (c) tailings sand.***

The measurement procedure on research objective 3 entailed the following:

1. All measurements were performed in plan view.
2. Each particle's $A_o$, $P_o$, and $D_{max}$ were measured on micrographs, which facilitated the computation of ellipseness in plan view.
3. Thereafter, the maximum inscribed circle (whose diameter is denoted as $D_{ic}$) was constructed within each particle's outline.
4. The degree of curvature of a corner along a particle's outline was determined by the construction of a circle whose radius coincided with the radius of curvature of that corner. This procedure was repeated for corners along the particle's outline (Figure 3-18).
5. Wadell's (1932) first formula (Eq. 2-5) was used to compute the roundness index, denoted as R, in this study.

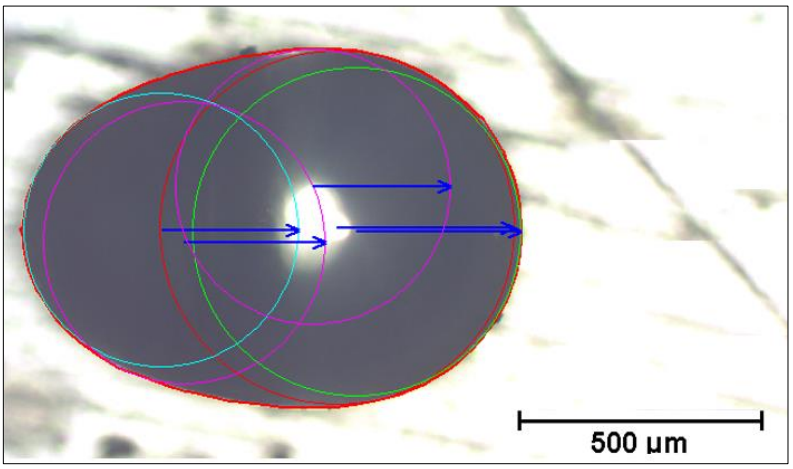



***Figure 3-18: Construction of the circles with radii defining the degree of curvature along a particle's outline.***

# 4 RESULTS & DISCUSSION

Herein, the experimental results validating the focus variation procedure are presented. Moreover, form characterization - using the Zingg (1935) diagram - and the analysis exploring particle angularity are discussed.

## 4.1 Validation: Focus Variation (FV) Method

The relationship between $D_L$ and $D_{\Delta f}$ for each material group is presented in Figures 4-1 through 4-5. Figure 4-6 covers the entire dataset's relationship between these two variables. There is a very strong correlation between $D_L$ and $D_{\Delta f}$ to the 1:1 line, producing a coefficient of determination of 0.9995 ($R^2 \approx 1$). This observation indicates excellent agreement between the two methods and reinforces the aptness of the FV technique. Eddey et al. (2019) produced a similarly strong correlation (where $R^2 = 0.999 \approx 1$) between the two variables, with a much smaller dataset comprising iron filings and platinum tailings, within a height interval from 500 to 1200 μm. The maximum underestimated and overestimated errors, defined by $D_L$-$D_{\Delta f}$, were 16.3 μm and 16 μm, respectively (Figure 4-7). Focus variation produced a mean underestimation and overestimation of error 4.1 μm and 4.3 μm, respectively (Figure 4-7). Furthermore, these two data subsets (i.e. underestimation where $D_L - D_{\Delta f} > 0$ and overestimation where $D_L - D_{\Delta f} < 0$) were statistically similar based on the following characteristics:

- Both their mean errors were comparatively very close to one another - producing a difference of 3.5 %
- Both errors varied over the same range of approximately 16 μm.

- Both the underestimation and overestimation errors produced positively skewed approximately normal distributions (as indicated by the frequency distribution histograms in Figure 4-8 a) with skewness coefficients of 1.4 and 1.1, respectively;
- The standard deviations of 3.7 μm and 3.5 μm associated with ($D_L$ - $D_{\Delta f}$ > 0) and ($D_L$ - $D_{\Delta f}$ < 0), respectively, were within 3.8 % of one another.

The error (including both $D_L$ - $D_{\Delta f}$ > 0 and $D_L$ - $D_{\Delta f}$ < 0) produced an approximately normal distribution curve with a mean error of -0.19 μm (Figure 4-8 b). Hence, the FV method did not produce any systematic bias to neither underestimate nor overestimate the mean particle height ($D_L$).

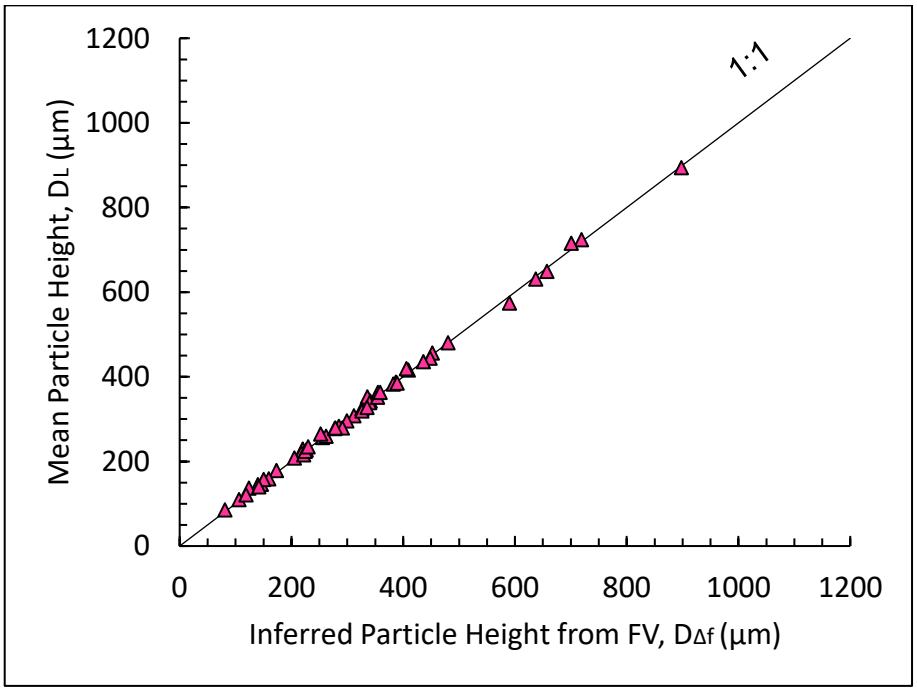



***Figure 4-1: Relationship between $D_L$ and $D_{\Delta f}$ for West Bank beach sand.***

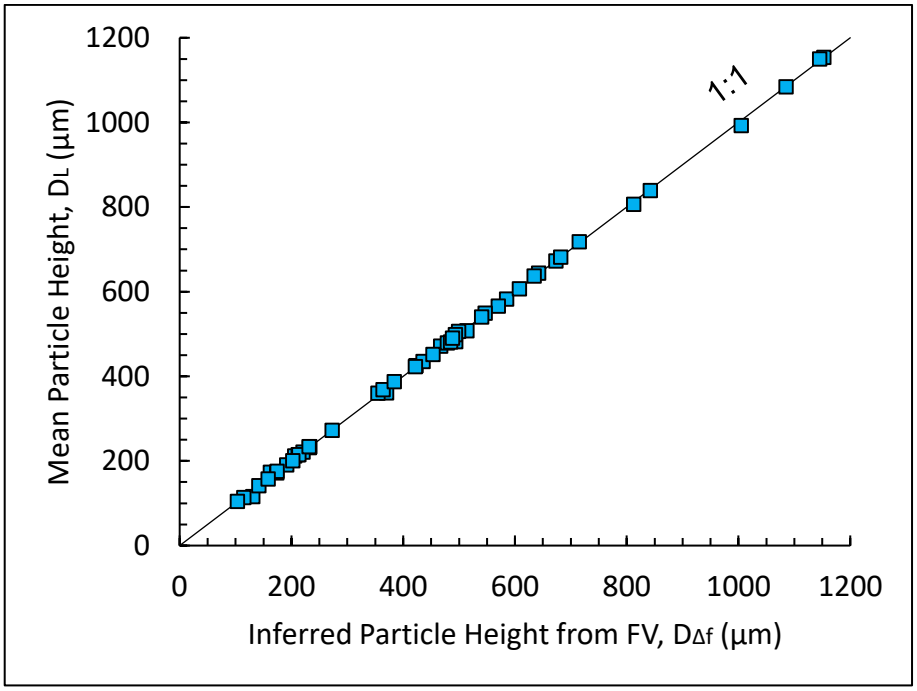



***Figure 4-2: Relationship between $D_L$ and $D_{\Delta f}$ for quartz sand.***

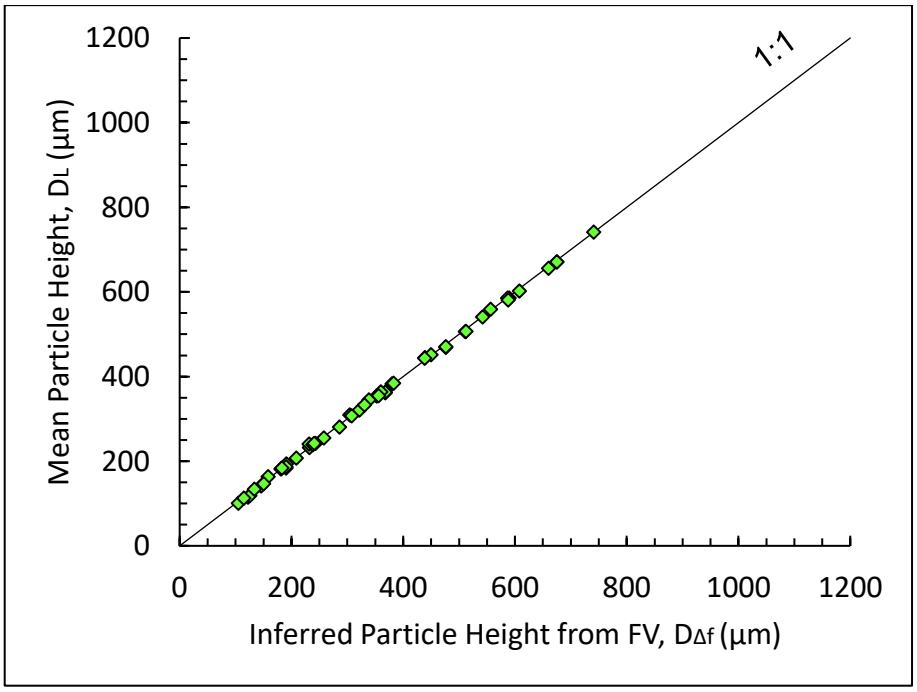



***Figure 4-3: Relationship between $D_L$ and $D_{\Delta f}$ for platinum tailings sand.***

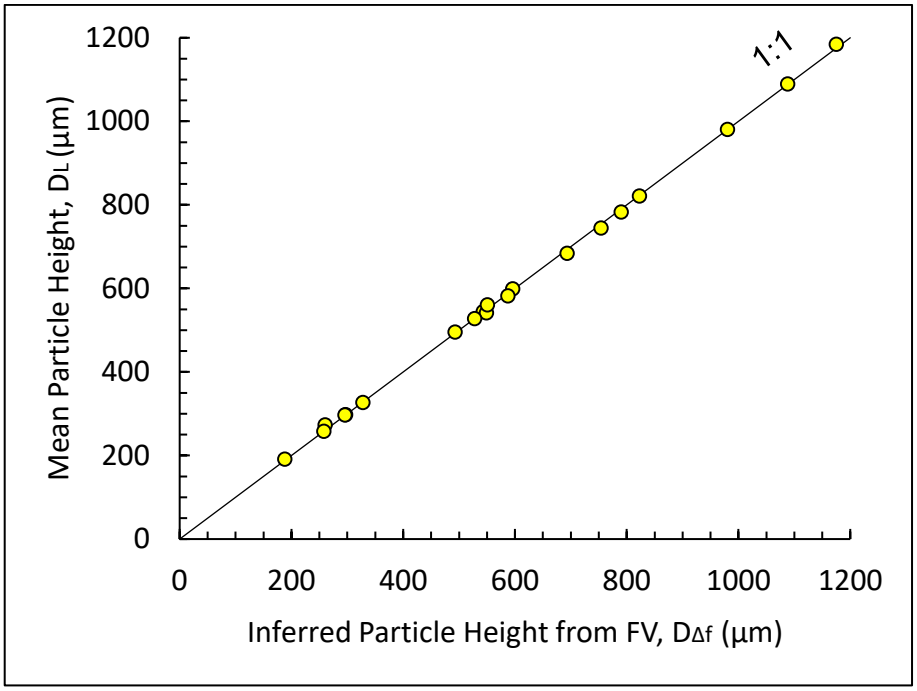



***Figure 4-4: Relationship between $D_L$ and $D_{\Delta f}$ for glass beads.***

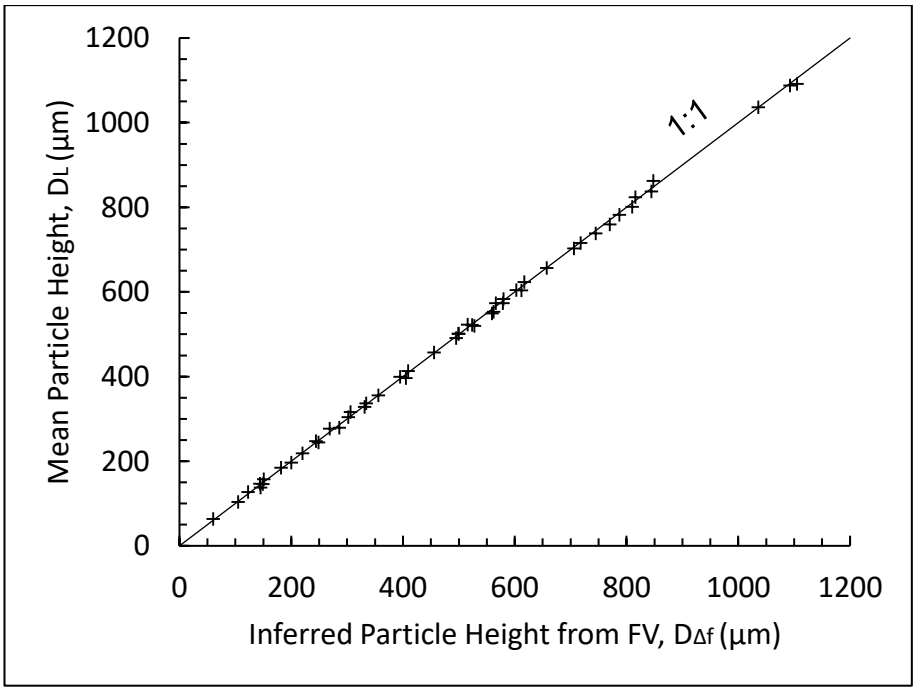



***Figure 4-5: Relationship between $D_L$ and $D_{\Delta f}$ for Ballito beach sand.***

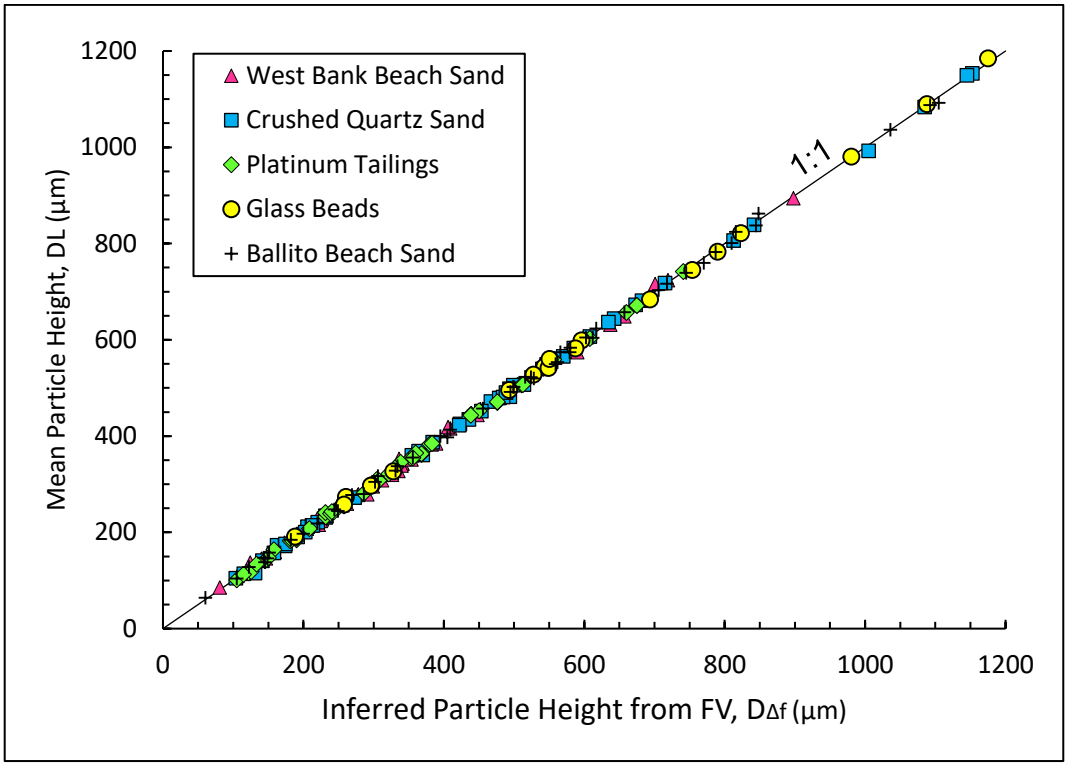



***Figure 4-6:Relationship between $D_L$ and $D_{\Delta f}$ for the entire dataset.***

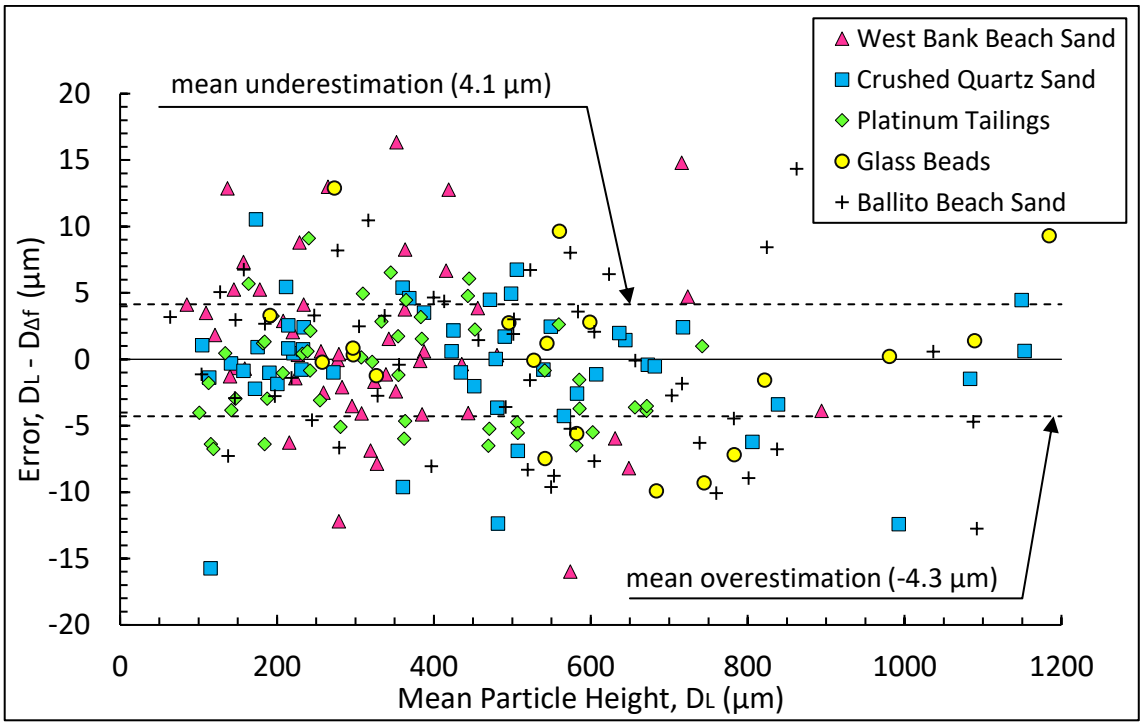



***Figure 4-7: Error, $D_L$ - $D_{\Delta f}$, plotted against $D_L$ for the entire dataset.***

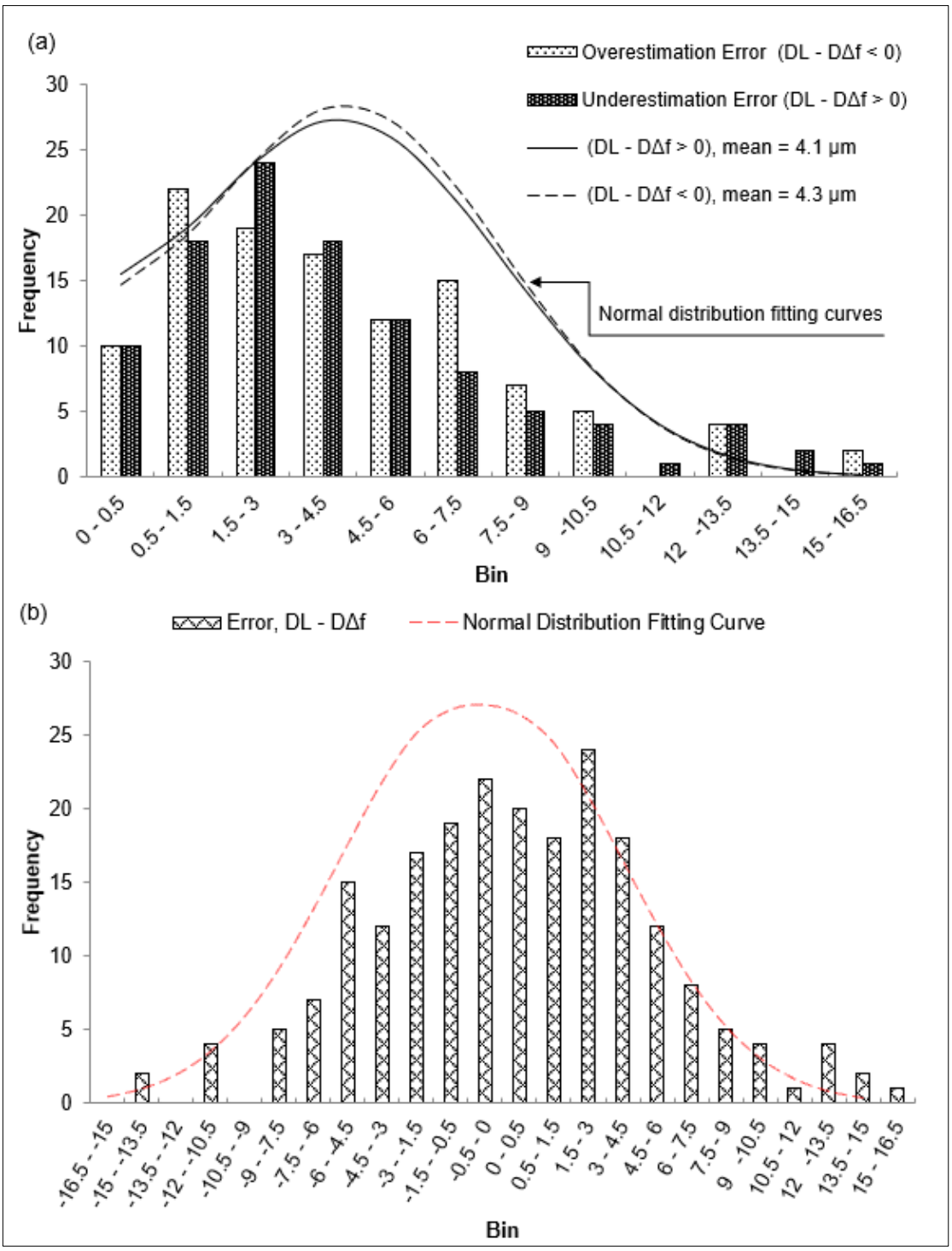



***Figure 4-8: Frequency distribution diagrams, (a) Overestimation and underestimation errors and (b) Error defined by $D_L$ - $D_{\Delta f}$.***

Per Figure 4-9, the mean absolute difference between the two lateral (orthogonal) particle height measurements (i.e., mean of abs [$D_{L1} – D_{L2}$]) was 2.2 μm. The trend between the error, $D_L – D_{\Delta f}$, plotted against $D_L$ (Figure 4-7), and the trend of $D_{L1} – D_{L2}$ plotted against $D_L$ (Figure 4-8) are similar – their cumulative distribution curves are very close to one another (as shown in Figure 4-10). Along both S-curves, 90 % of each dataset, produced an absolute error of less than 3.3 % when $D_L – D_{\Delta f}$ and $D_{L1} – D_{L2}$ were both normalized by $D_L$. This suggests that some of the differences between $D_L$ and $D_{\Delta f}$ which are observed in Figure 4-7, are due not to limitations in the FV method, but rather due to inherent limitations in assessing particle height from a lateral view. If the latter method were perfect, there would be no measurable differences between $D_{L1}$ and $D_{L2}$, but Figure 4-9 indicates that this is not the case. These observations support the validity of the FV method to indirectly measure particle height.

Discrepancies between $D_{L1}$ and $D_{L2}$ may generally be attributed to difficulties in tracing the particle outline that emanate from a limited depth of field - in which irregularly shaped particles may not distinctly display their entire outline. This limitation was observed even though measurements of the lateral views were predominantly performed using 50x total magnification– which produced the largest and widest depth of field.

Figure 4-11 presents the error, $D_L – D_{\Delta f}$, normalized by $D_L$, plotted against $D_L$. A mean normalized absolute error of 1.34 % was calculated for the entire dataset, which produced a minimum and maximum normalized error of -14 % and 9.4 %, respectively. The underlying premise is that the FV method

does not show a tendency towards under- or overestimations of particle height. The upper and lower bounds shown in Figure 4-11 are symmetric about the horizontal axis. So, in agreement with this result, I suggest that the upper and lower bounds are simply mirrored reflections of one another.

The effect of magnification on $D_{\Delta f}$ was also explored (Figures 4-12 and 4-13). A narrow error range resulted from the use of higher magnification to measure $D_{\Delta f}$. The magnification of 50x produced a wider error range (i.e. max. error – min. error, where the error is defined by $D_L$-$D_{\Delta f}$) of 30.8 µm, compared to an error range of 17.7 µm (42 % less), associated with the 200x magnification. Darker images associated with the 5x objective contributed to an increased error range. Similarly, the 100x magnification produced a higher error between 150 µm and 300 µm, along the x-axis, compared to the 200x magnification. The lower the magnification, the wider the depth of field, and the higher the absolute error that can be incurred when implementing the focus variation method.

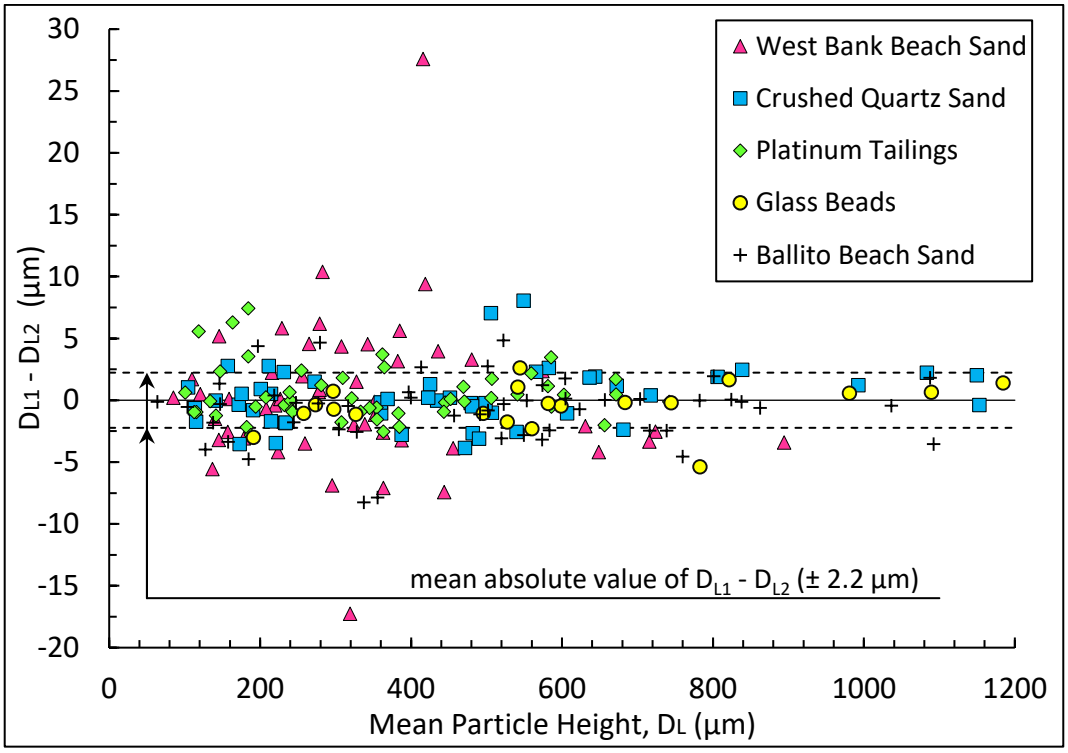



***Figure 4-9: $D_{L1} – D_{L2}$ vs $D_L$ for the entire dataset.***

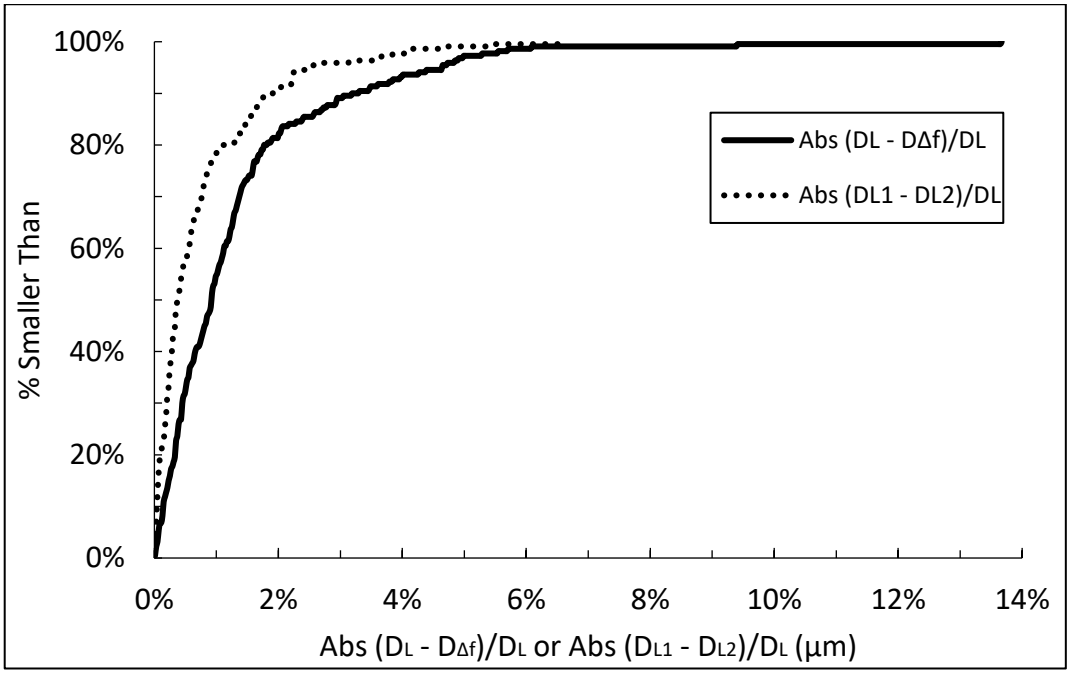



***Figure 4-10: S-curve distributions for the normalized absolute ($D_L$-$D_{\Delta f}$)/$D_L$ and the normalized absolute ($D_{L1}$-$D_{L2}$)/$D_L$.***

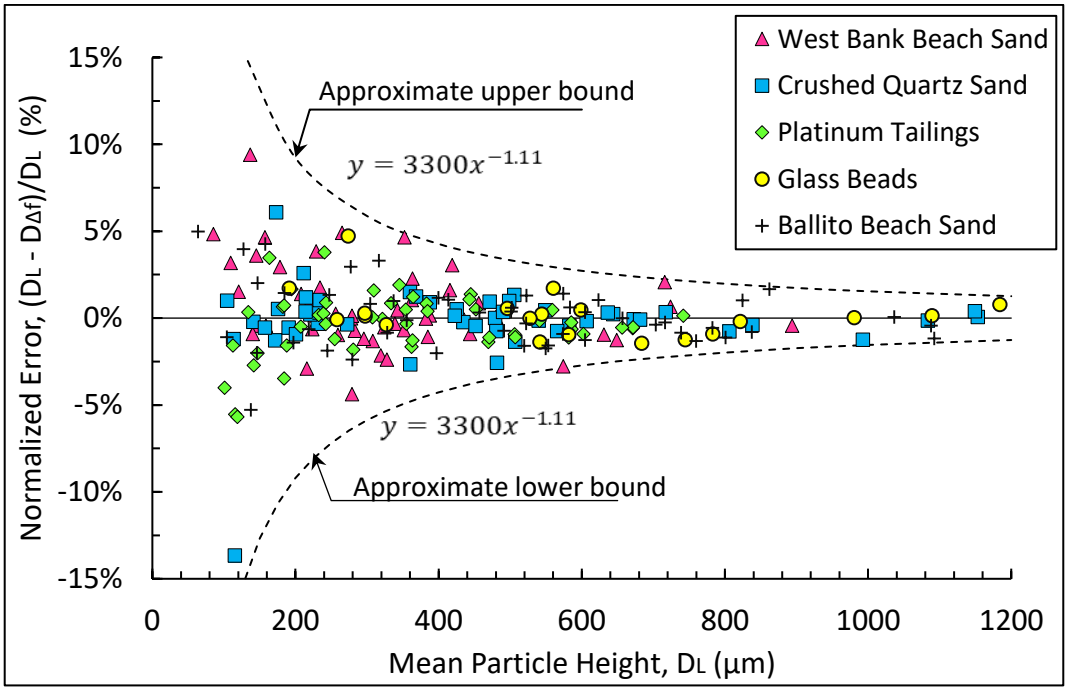



***Figure 4-11: Relationship between the normalized error and $D_L$.***

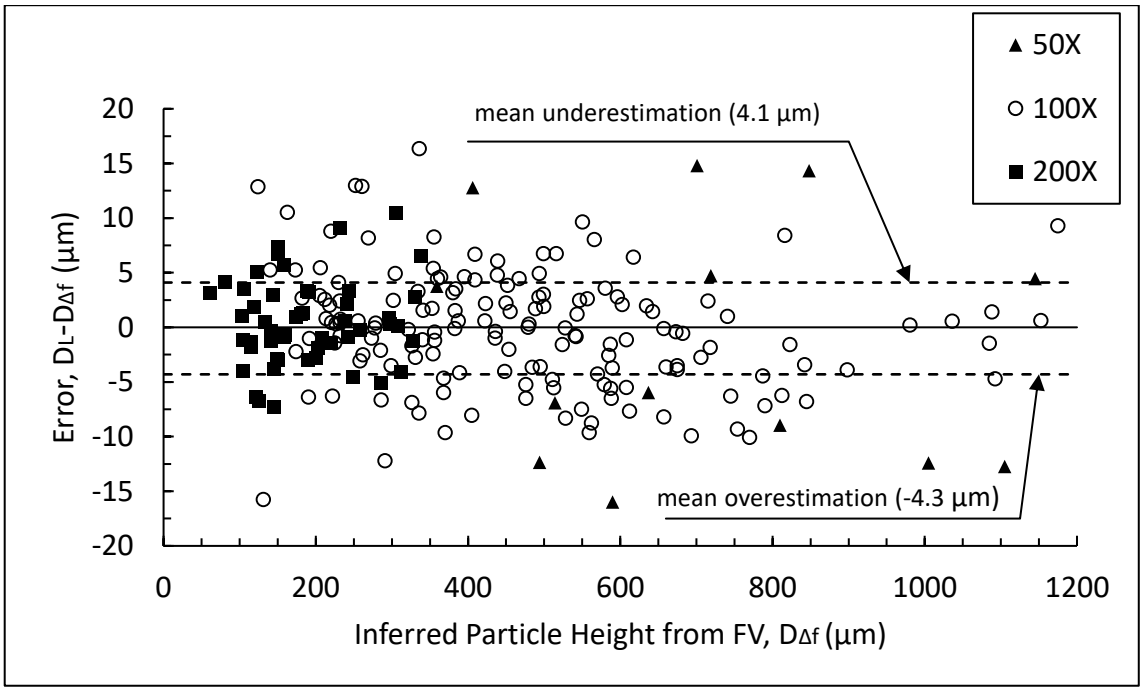



***Figure 4-12: Error, $D_L$ - $D_{\Delta f}$, vs $D_{\Delta f}$, filtered by magnification.***

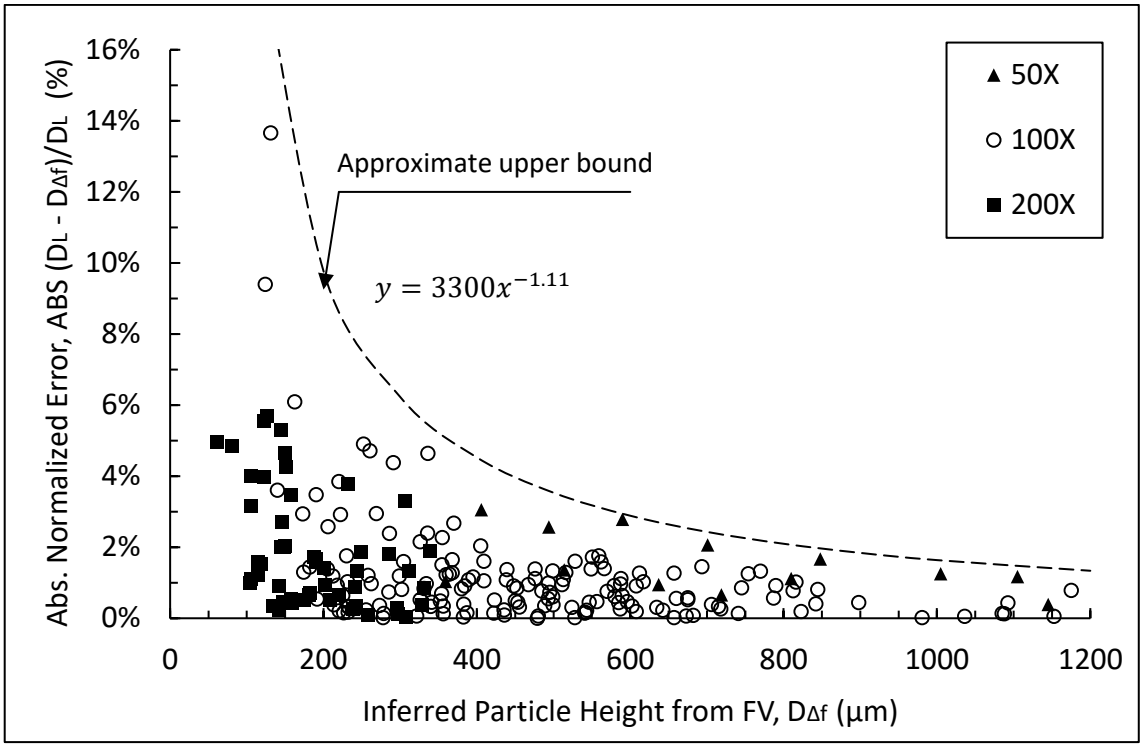



***Figure 4-13: Absolute normalized error plotted against $D_{\Delta f}$.***

## 4.2 Form Assessment

The distributions of form across the Zingg (1935) diagram are illustrated in Figures 4-14 to 4-18. Except for glass beads, the spatial distributions of natural and crushed sands were mainly concentrated between rod-like and equant forms. Both platinum tailings and quartz sand consisted of mainly elongated (rod-like) particles. Basic statistical parameters for the flatness (S/I) and elongation ratios (I/L), and degree of equancy (S/L) of all material groups are summarised in Tables 4-1, 4-2, and 4-3, respectively. All materials exhibited high mean S/I and I/L ratios, explaining why most data points were scattered between equant and elongated classes. Analysis of the range and standard deviation of S/I, I/L, and S/L suggests that the variability of these form ratios, in sands, is quite similar.

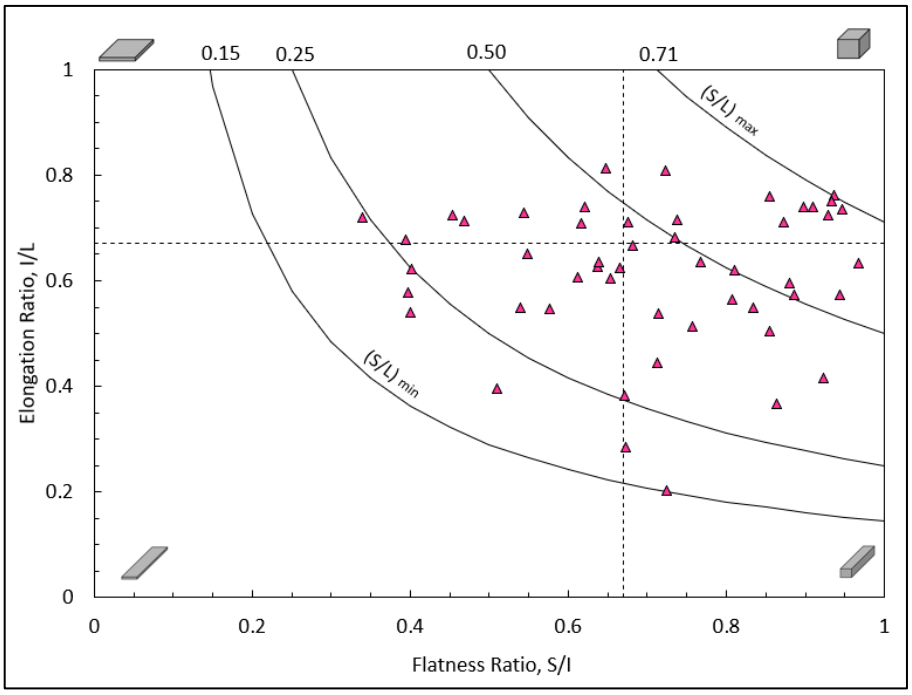



***Figure 4-14: Plot of form parameters showing West Bank beach sand.***

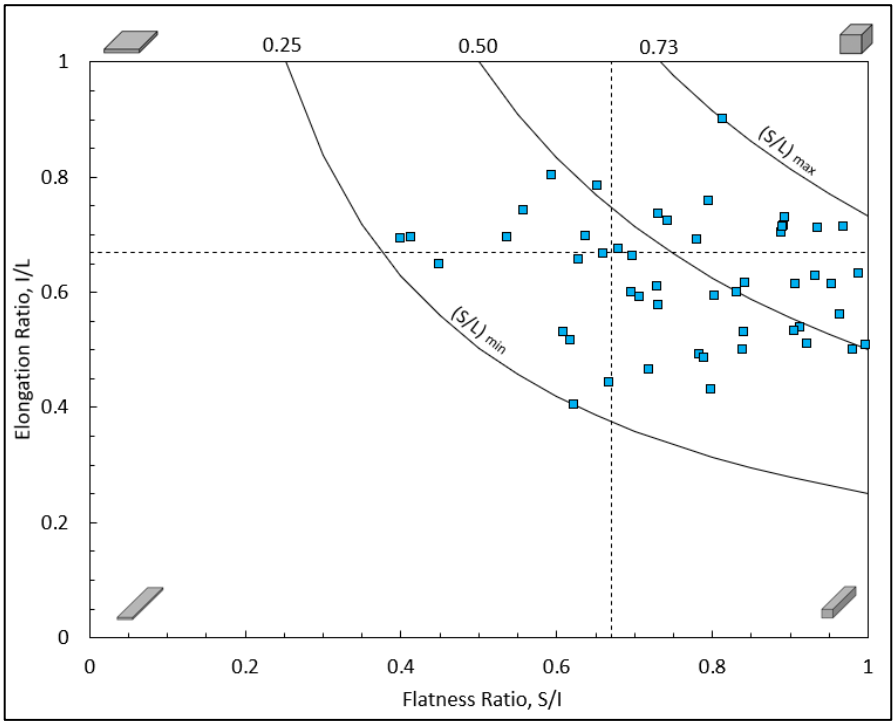



***Figure 4-15: Plot of form parameters showing crushed quartz sand.***

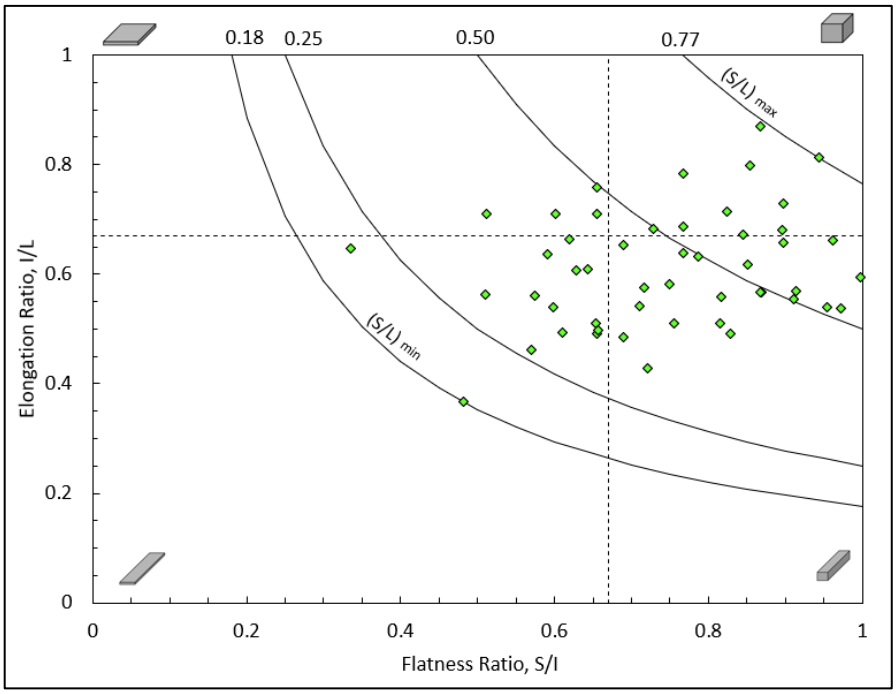



***Figure 4-16: Plot of form parameters showing platinum tailings sand.***

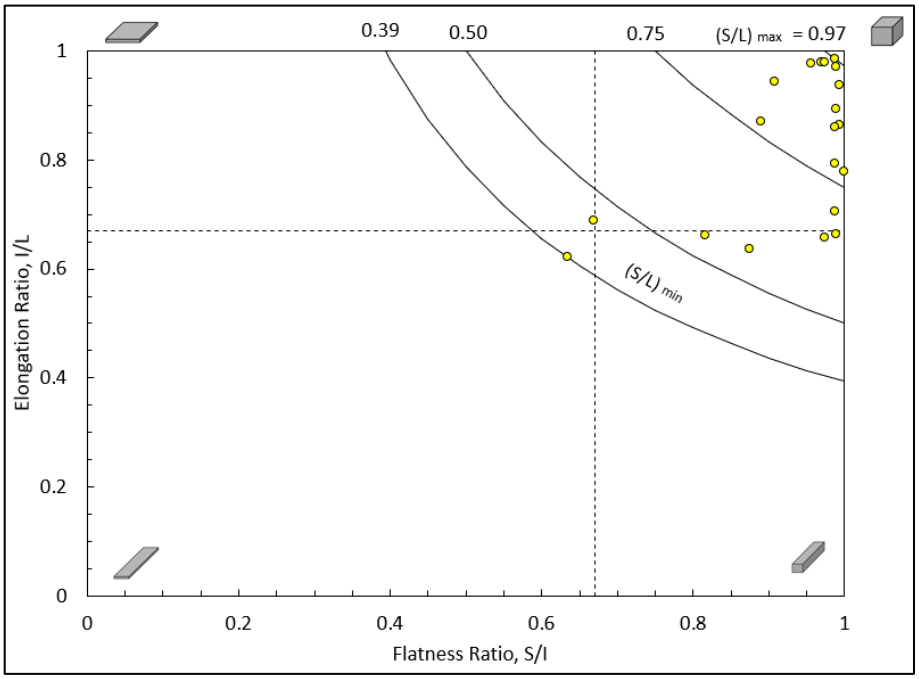



***Figure 4-17: Plot of form parameters showing spherical glass beads.***

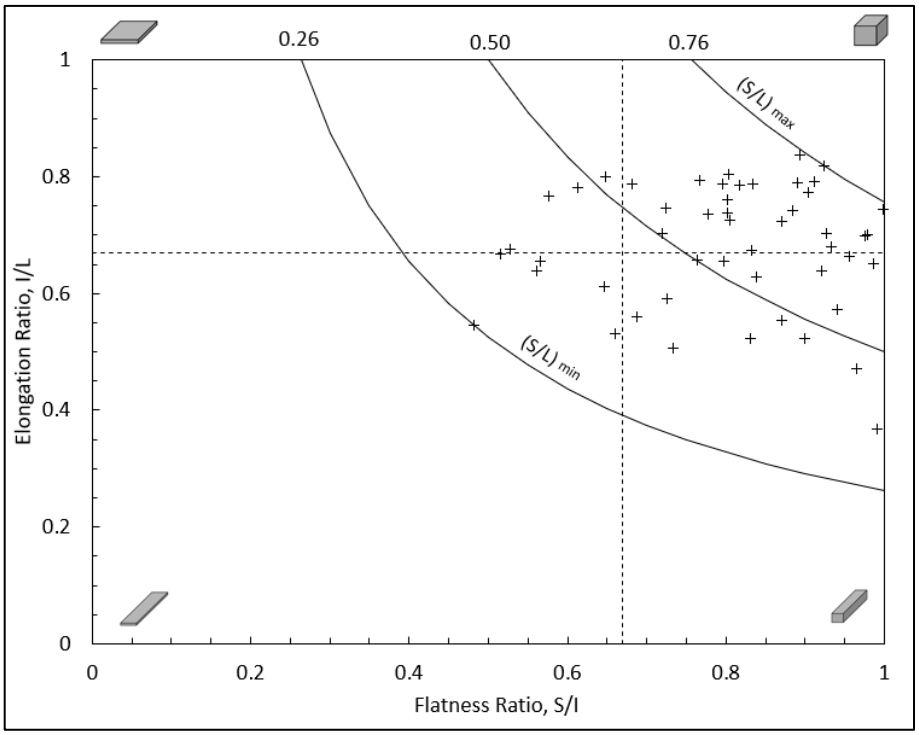



***Figure 4-18: Plot of form parameters showing Ballito beach sand.***

***Table 4-1: Comparison of basic statistical parameters for S/I.***

| Material | Min. | Max. | Range | Mean | Std. Dev. |
|---|---|---|---|---|---|
| Westbank beach sand | 0.34 | 0.97 | 0.63 | 0.71 | 0.17 |
| Quartz sand | 0.40 | 1.00 | 0.60 | 0.77 | 0.15 |
| Platinum tailings | 0.34 | 1.00 | 0.66 | 0.74 | 0.15 |
| Glass Beads | 0.63 | 1.00 | 0.36 | 0.93 | 0.11 |
| Ballito beach sand | 0.48 | 1.00 | 0.52 | 0.80 | 0.14 |

***Table 4-2: Comparison of basic statistical parameters for I/L.***

| Material | Min. | Max. | Range | Mean | Std. Dev. |
|---|---|---|---|---|---|
| Westbank beach sand | 0.20 | 0.81 | 0.61 | 0.61 | 0.13 |
| Quartz sand | 0.40 | 0.90 | 0.50 | 0.62 | 0.11 |
| Platinum tailings | 0.37 | 0.87 | 0.50 | 0.61 | 0.10 |
| Glass Beads | 0.62 | 0.99 | 0.37 | 0.82 | 0.13 |
| Ballito beach sand | 0.37 | 0.84 | 0.47 | 0.68 | 0.10 |

***Table 4-3: Comparison of basic statistical parameters for S/L.***

| Material | Min. | Max. | Range | Mean | Std. Dev. |
|---|---|---|---|---|---|
| Westbank beach sand | 0.15 | 0.71 | 0.57 | 0.43 | 0.15 |
| Quartz sand | 0.25 | 0.73 | 0.48 | 0.48 | 0.12 |
| Platinum tailings | 0.18 | 0.77 | 0.59 | 0.46 | 0.13 |
| Glass Beads | 0.39 | 0.97 | 0.58 | 0.77 | 0.18 |
| Ballito beach sand | 0.26 | 0.76 | 0.49 | 0.54 | 0.13 |

Although the Zingg (1935) diagram permits a comprehensive characterization of form, it contains no information on particle size. Because sieve analysis can be considered a very crude measurement of particle size, the three-dimensional Pythagorean size (P) of each particle was calculated using Eq. 4-1 below. This arbitrary equation is simple and accounts for three principal dimensions: S, I, and L. The effect of the Pythagorean particle size on S/I, I/L, and S/L was explored, as shown in Figures 4-19, 4-20, and 4-21,

respectively. There exists no discerning trend between P and any of the three form ratios, as these form ratios can vary widely with P. This observation contests those from Le Pen et al. (2013) who observed a weak trend for S/L to reduce with increasing particle size in Ballast stone. Wang et al. (2020) also observed weak trends between various particle shape parameters and particle size ranges for coral and quartz sands.

$$P = \sqrt{S^2 + I^2 + L^2} \qquad \text{Eq. 4-1}$$

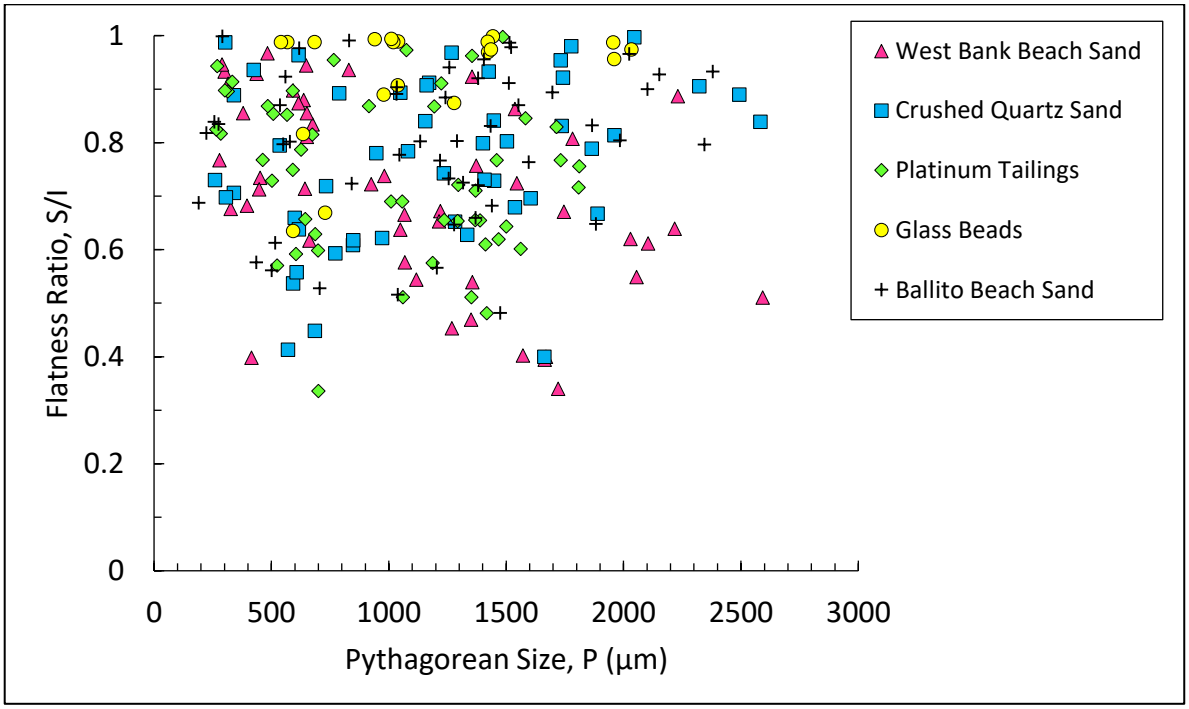



***Figure 4-19: Flatness ratio, S/I, plotted against Pythagorean size, P.***

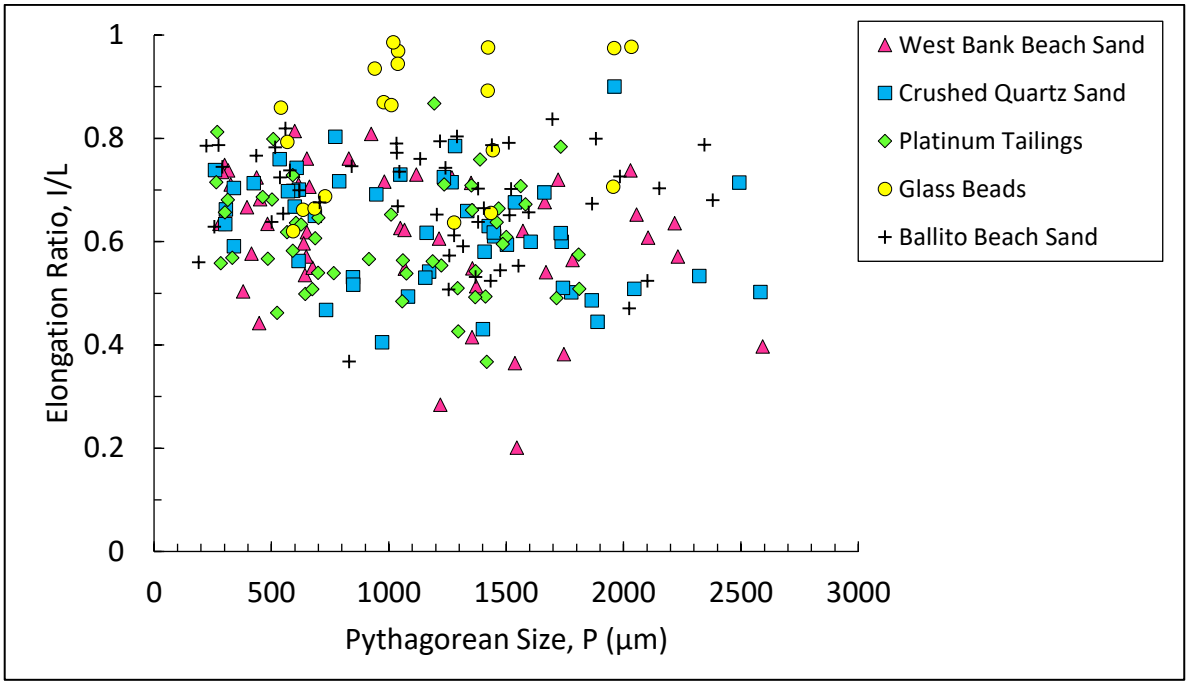



***Figure 4-20: Elongation ratio, I/L, plotted against Pythagorean size, P.***

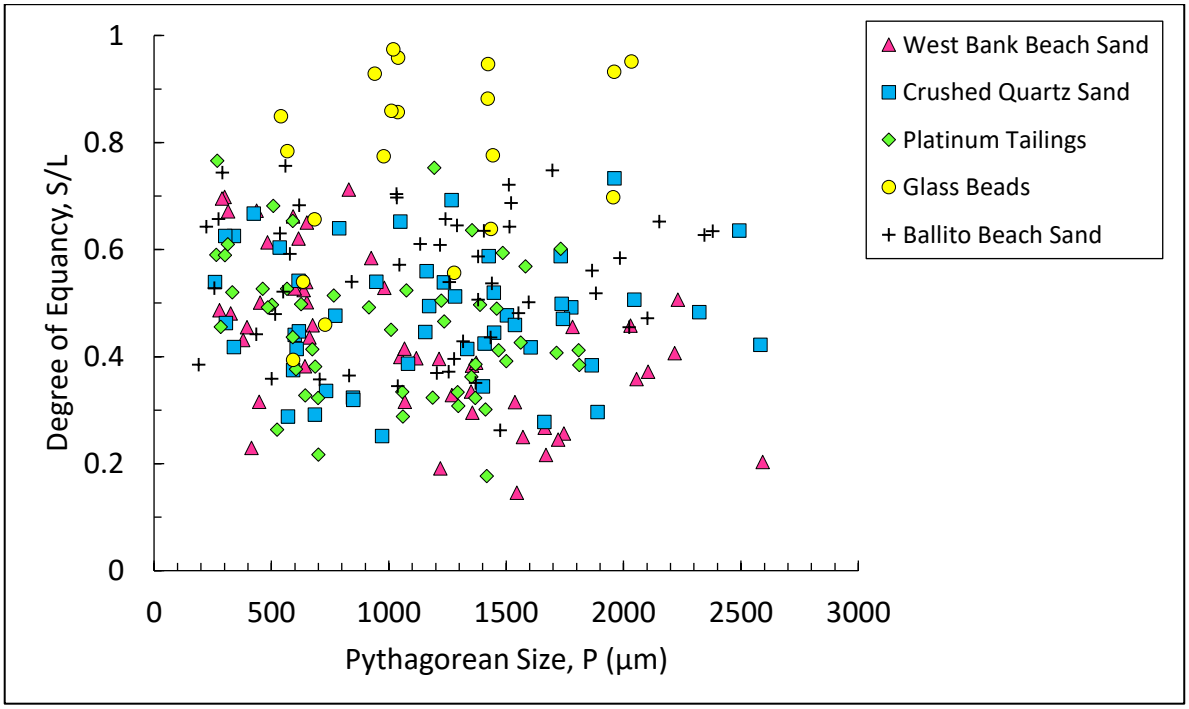



***Figure 4-21: Degree of equancy, S/L, plotted against Pythagorean size, P.***

## 4.3 Characterization of Angularity

The relationship between the mean ellipseness from two orthogonal lateral views (i.e. $E_L$ where $E_L$ is the mean of $E_{L1}$ and $E_{L2}$) and ellipseness in the plan view ($E_p$) was evaluated as shown in Figure 4-22. The scatter in the data is largely attributed to the angular quartz and tailings sands. For the sands considered in this study, $E_p$ differed by as much as 10.7 % less than $E_L$ and, 9.9 % more than $E_L$ (Figure 4-23). The overall trend observed in Figures 4-22 and 4-23, is that the discrepancy between $E_p$ and $E_L$ reduces as $E_L$ tends toward 1 (i.e. as the overall particle roundness increases and approaches a shape of perfect roundness).

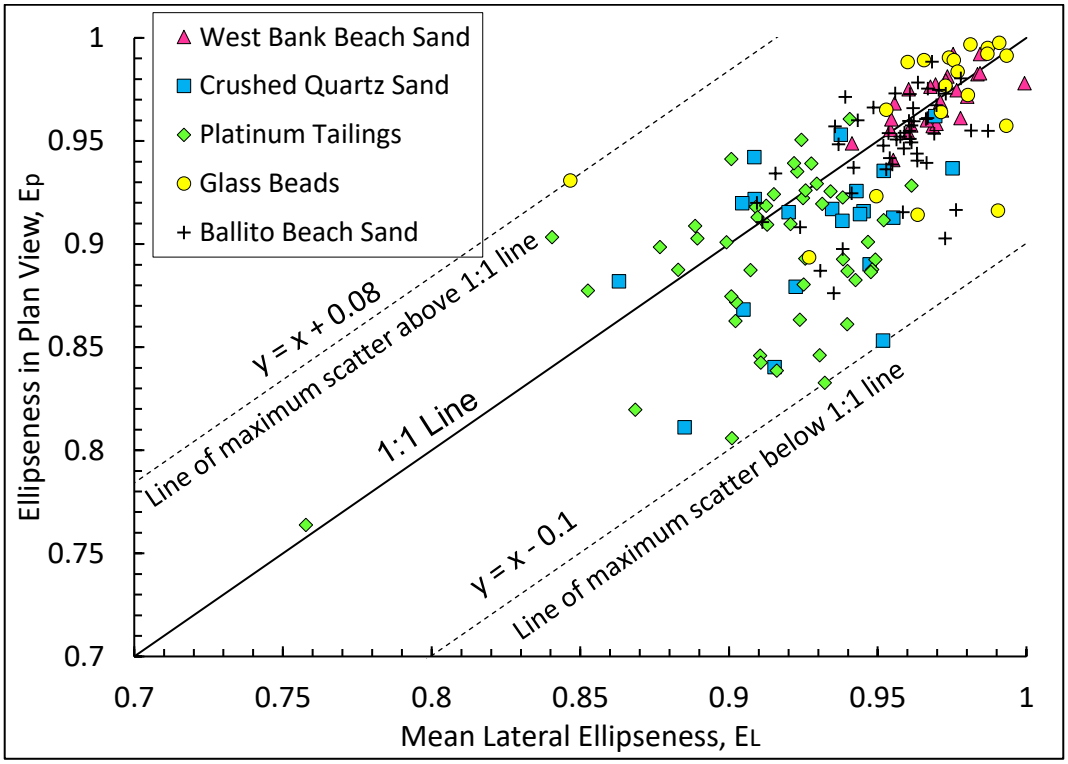



***Figure 4-22: $E_p$ plotted against $E_L$.***

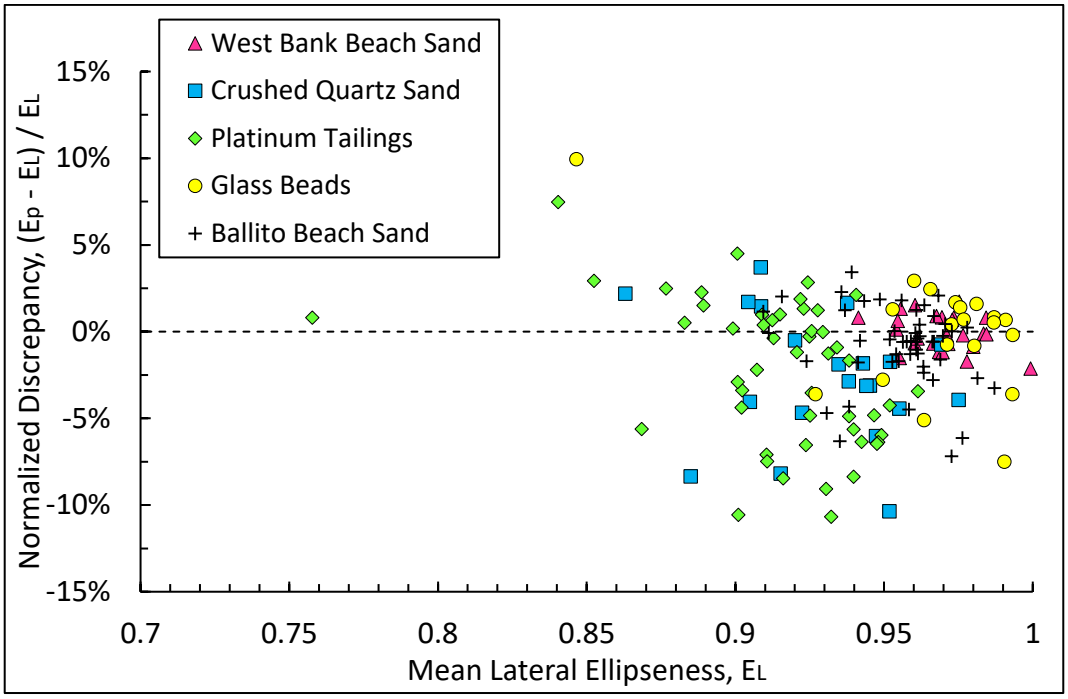



***Figure 4-23: The trend of $E_P$ - $E_L$, expressed as a percentage of $E_L$, plotted against $E_L$.***

Figure 4-24 shows examples of two particles where $E_p$ varied by more than 9.9%, in a glass bead particle (Figure 4-24 a to c), and by more than 9%, in a tailings sand particle (Figure 4-24 d to f), relative to $E_L$. The increase in the discrepancy between $E_p$ and $E_L$ was affected by: i) an increase in the number and magnitude of protruding corners and edges along a particle's outline, and ii) an increase in roughness and the degree of irregularity along the particle's outline.

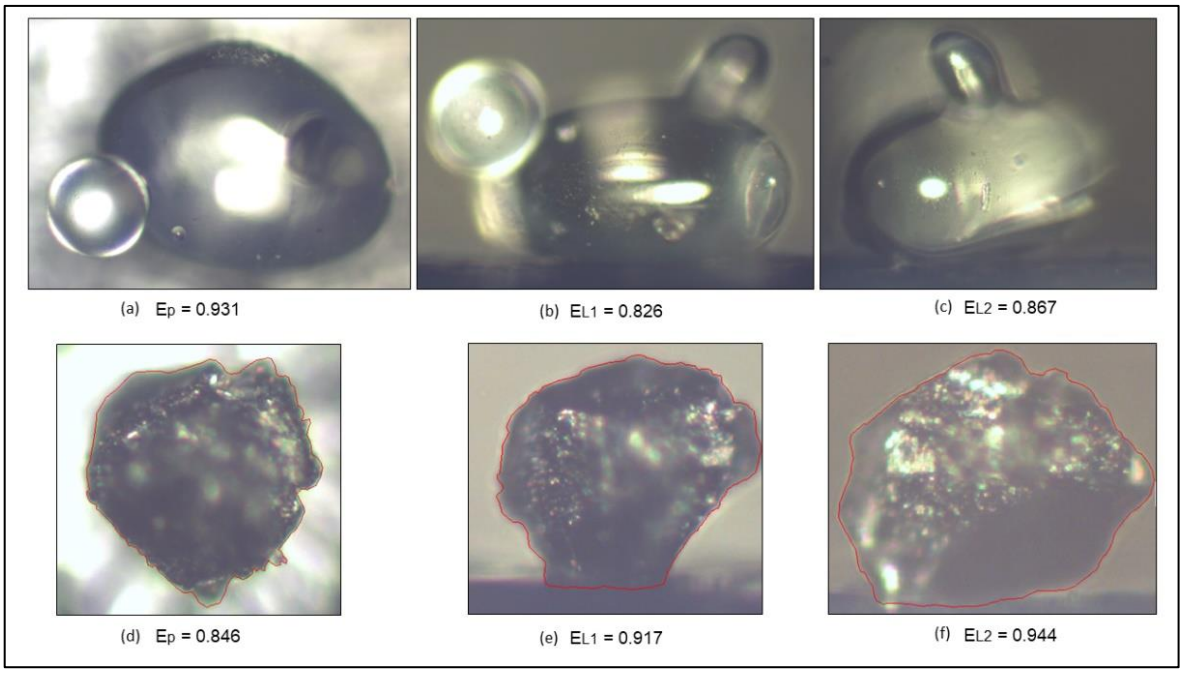



***Figure 4-24: Comparison of $E_p$, $E_{L1}$, and $E_{L2}$: (a) to (c) glass bead, (d) to (f) platinum tailings particle.***

The basic statistical descriptors for $E_p$, $E_{L1}$ and $E_{L2}$ are shown in Table 4-4. The beach sands produced the lowest standard deviations associated with the measurement of $E_p$, $E_{L1}$, and $E_{L2}$. The angular tailings and quartz sands produced the highest ranges, in which ellipseness varied, and the highest standard deviations for $E_p$, $E_{L1}$, and $E_{L2}$ – implying higher variability of ellipseness in the three-orthogonal projections assessed. These observations mean that there is typically less variability in the ellipseness in the three (orthogonal) views assessed in both beach sands compared to tailings and quartz sands. This finding is also in agreement with the observation that the variability of ellipseness between the plan view and

orthogonal lateral views tends to reduce as the particle becomes more rounded, that is, as the particle's ellipseness tends toward 1.

Glass beads and both beach sands revealed high degrees of ellipseness with mean ellipseness values varying between i) 0.969 and 0.97, for West Bank beach sand, ii) 0.965 and 0.969 for glass beads and, iii) 0.947 and 0.960 for Ballito beach sand. Platinum tailings sand produced the widest range of ellipseness values, which varied between 0.74 and 0.975.

The effects of chipping and fracturing due to the rock-crushing process involved during the formation of the quartz and platinum tailings sands appear to contribute to the higher variability of ellipseness in the three-orthogonal projections. Based on these findings, I suggest that the overall characterization of ellipseness in crushed (angular) sands cannot be relied upon from a single 2D view. On the other hand, I suggest that one projection is satisfactory in characterizing the total or overall ellipseness of subrounded to rounded beach sands that experienced natural and gentle conditions of wear. Wadell (1932) argued that a high degree of roundness is often an indication of gentle conditions of wear relative to the size, hardness and toughness of the particle.

***Table 4-4: Statistical parameters for ellipseness.***

| Material | $E_P$ = Ellipseness in plan-view | | | | | $E_{L1}$ = Ellipseness in lateral view 1 | | | | | $E_{L2}$ = Ellipseness in lateral view 2 | | | | |
|---|---|---|---|---|---|---|---|---|---|---|---|---|---|---|---|
| | **Min.** | **Max.** | **Range** | **Mean** | **Std. Dev.** | **Min.** | **Max.** | **Range** | **Mean** | **Std. Dev.** | **Min.** | **Max.** | **Range** | **Mean** | **Std. Dev.** |
| West Bank beach sand | 0.941 | 0.992 | 0.051 | 0.969 | 0.013 | 0.929 | 1.000 | 0.071 | 0.970 | 0.015 | 0.931 | 0.996 | 0.065 | 0.969 | 0.015 |
| Quartz sand | 0.811 | 0.962 | 0.150 | 0.905 | 0.038 | 0.853 | 0.982 | 0.130 | 0.931 | 0.034 | 0.873 | 0.974 | 0.100 | 0.929 | 0.026 |
| Platinum tailings | 0.764 | 0.961 | 0.197 | 0.893 | 0.039 | 0.743 | 0.963 | 0.220 | 0.907 | 0.039 | 0.772 | 0.975 | 0.203 | 0.921 | 0.036 |
| Glass beads | 0.893 | 0.998 | 0.100 | 0.966 | 0.033 | 0.826 | 0.995 | 0.170 | 0.965 | 0.04 | 0.867 | 0.996 | 0.130 | 0.969 | 0.030 |
| Ballito beach sand | 0.876 | 0.988 | 0.112 | 0.947 | 0.025 | 0.872 | 0.989 | 0.118 | 0.952 | 0.026 | 0.919 | 0.996 | 0.076 | 0.960 | 0.015 |

Further assessment of ellipseness entailed the evaluation of $E_p$ against Wadell's (1932) roundness index, R, (Figure 4-25). R can vary over a broad range between 0 and 1, thus, distinguishing between angular, sub-angular, sub-rounded, and rounded particles. The trend shown in Figure 4-25 suggests that the roundness index, R, becomes rapidly sensitive to change with increasing $E_p$ (particularly for $E_p$ values between 0.95 and 1).

The relationship between $E_p$ and R is better represented on a semi-logarithmic plot (Figure 4-26) to facilitate the characterization of ellipseness into four roundness classes. Hence, the interpretation of the trend between these two parameters was enhanced by incorporating a roundness classification scheme proposed by Blott & Pye (2008).

Despite the overlap between the datasets (Figure 4-25), the broad trend is that the glass beads and West Bank beach sand produced the highest ellipseness and roundness indices, and the quartz and tailings sands produced the lowest ellipseness and roundness indices. This trend is consistent with the erosion processes that lead to the rounding of beach sand particles (facilitated by attrition). Wadell (1932) noted that the rounding of sedimentary particles is a special type of disintegration attributed to attrition and solution. The low roundness in crushed quartz and tailings sands is consistent with the rock-crushing processes involved in the creation of these sands - roundness is effectively reduced by fracturing and chipping. Although ellipseness sufficiently separated angular particles from rounded particles, it did not distinctly separate subangular particles from subrounded and rounded particles.

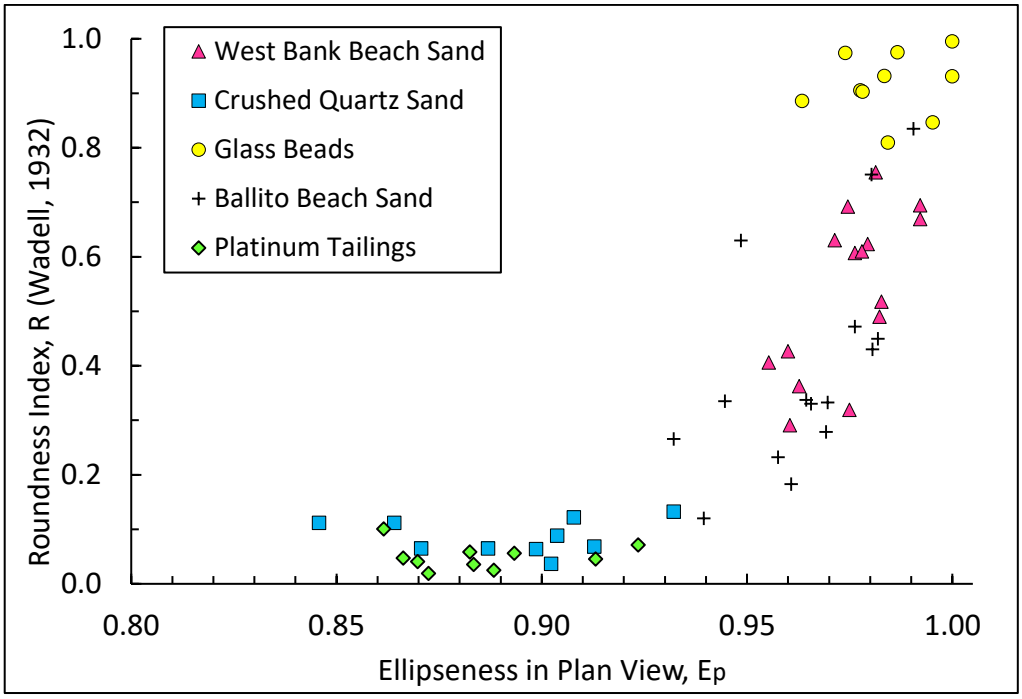



***Figure 4-25: Evaluation of $E_p$ against Wadell's (1932) roundness, R.***

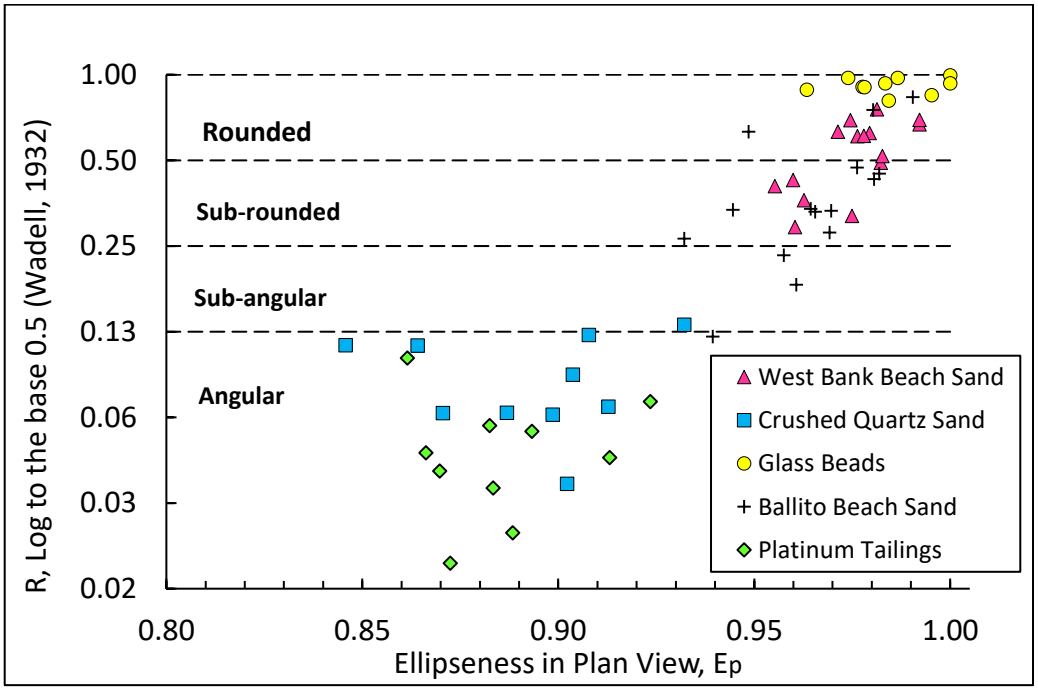



***Figure 4-26: $E_p$ plotted against R, including a roundness classification scheme proposed by Blott & Pye (2008).***

# 5 CONCLUSIONS

Particle shape is an important soil index property influencing the mechanical behaviour of a soil mass. Shape is defined by form, angularity, and roughness. Despite advancements in contemporary technology, there lacks a simple and inexpensive method for measuring the three-dimensional form of sand-sized particles. By measuring a particle's overall breadth and length in one projection, focus variation can be implemented to facilitate the quantification of three-dimensional form, in that same projection, thus eliminating the need to rotate a particle to its lateral projections.

Focus variation microscopy is routinely used in surface metrology studies (e.g., Danzl et al., 2009; Danzl et al., 2011; Helmli, 2011; Xu et al., 2022).

Hence, this study's first research objective pertained to the efficacy of using focus variation for the indirect measurement of particle height ($D_{\Delta f}$), using a conventional optical microscope, on sand-sized particles ranging from rounded natural sands to crushed, angular sands, and varying in size between 50 and 1200 μm. Particle heights were, in fact, successfully measured within a size interval from 60.5 to 1175 μm.

Focus variation (FV) was validated by measurements of particle height from two orthogonal lateral views – which necessitated securing each particle to a base. FV produced mean absolute discrepancies of approximately 4 μm and with no tendency of $D_{\Delta f}$ to over- or underestimate mean particle height, $D_L$. When expressed as a percentage of $D_L$, the mean and maximum absolute discrepancies between $D_{\Delta f}$ and $D_L$ were typically lower than 1.4 % and 14 %, respectively. The FV procedure does not appear

to compromise the quality of particle height measurements, as the trends of $D_L$ - $D_{\Delta f}$ vs $D_L$ and, $D_{L1}$ – $D_{L2}$ vs $D_L$ were statistically similar. The FV method was therefore commensurate with rotating a particle orthogonally to a lateral view to measure its height.

The FV procedure facilitated the characterization of form in spherical glass beads, two beach sands and quartz and tailings sands. The form ratios S/I, I/L and S/L varied widely within each type of sand – suggesting that a single scalar parameter cannot be relied upon to characterise the form of a group of particles such as in the case of Clayton et al.'s (2009) SEES parameter. Furthermore, the results indicated that these form ratios can also vary widely for particles of similar size when particle size was expressed as the Pythagorean size, P. These observations challenge findings from previous studies regarding the variability of form with particle size (Le Pen et al., 2013; Wang et al., 2020).

FV has proven to be a relatively quick, robust, simple, and cost-effective engineering instrument, which can be easily adopted by geotechnical engineering practitioners and researchers, to facilitate the three-dimensional quantification and characterization of sand-sized particles.

Particle angularity was characterized using the ellipseness (E) parameter, following Le Pen et al. (2013). Glass beads were used as a proxy for particles of extreme roundness. West Bank beach sand and Ballito beach sand generally exhibited high degrees of ellipseness in three orthogonal projections typically greater than 0.95.

For the sands considered in this study, ellipseness in plan-view ($E_p$) can vary by as much as 10.7 %, to the mean lateral ellipseness ($E_L$). In subrounded and rounded particles, ellipseness in plan view reasonably represented a particle's mean lateral ellipseness, with a discrepancy typically less than 2 %. Therefore, the overall ellipseness in subrounded to rounded beach sands can typically be characterized from one 2D view.

An increase in the discrepancy between $E_p$ and $E_L$ was caused by an increase in i) the number and magnitude of corners and edges along a particle's outline and, ii) the degree of irregularity and roughness along a particle's outline. Hence, in crushed (angular) sands, characterizing a particle's overall ellipseness cannot be relied upon from a single 2D view, due to a greater variability of ellipseness along three-orthogonal views.

Ellipseness was further assessed against Wadell's (1932) roundness index to examine the efficacy with which ellipseness distinguished between various degrees of roundness. For the sands considered in this study, ellipseness varied over a narrow range, typically between 0.75 and 1, and appeared to '*compress*' values predominantly between 0.85 and 1. This may be attributed to the limitations of the ellipseness method. Ellipseness sufficiently distinguished angular particles from rounded particles, but particles of intermediate degrees of roundness were not well separated from one another. The trend and characterization of angularity were consistent with i) the weathering processes involved in the formation of subrounded to rounded beach sands and ii) the crushing process involved in the creation of angular quartz and tailings sands.

# 6 REFERENCE LIST


Abbireddy, C., 2008. *Particle form and its Impact on Packing and Shear Behaviour of Particulate Materials. Doctor of Philosophy,* Southampton: University of Southampton.

Alshibli, K. A. et al., 2014. Quantifying Morphology of Sands Using 3-D Imaging. *J. Mater. Civil Eng..*

Aschenbrenner, B. C., 1956. A new method for expressing particle sphericity. *J. Sed. Petrol.,,* Volume 26, pp. 15 - 31.

ASTM2488-17E01, 2017. *Standard practice for description and identification of soils (visual-manual procedure).* West Conshohocken, PA, United States: ASTM International.

Barret, P. J., 1980. The shape of rock particles: a critical review. *Sedimentology,* 27(3), pp. 291 - 303.

Benn, D. I. & Ballantyne, C. K., 1993. The description and representation of particle shape. *Earth Surf. Proc. Land,* Volume 18, pp. 665 - 672.

Blott, S. & Pye, K., 2008. Particle shape: a review and new methods of characterization and classification. *Sedimentology,* Volume 55, pp. 31 - 63.

Bonneau, D. A. et al., 2019. Three-dimensional rockfall shape back analysis: methods and implications. *Nat. Hazards Earth Syst. Sci,* pp. 2745 - 2765.

Cho, G., Dodds, J. & Santamarina, J., 2006. Particle shape effects on packing density stiffness and strength: natural and crushed sands. *J. Geotech. Environ. Eng. ASCE,* 132(5), pp. 591 - 602.

Clayton, C. R. L., Abbireddy, C. O. R. & Schiebel, R., 2009. A method of estimating the form of coarse particulates. *Geotechnique,* 59(6), pp. 493-501.

Corey, A. T., 1949. *Influence of shape on fall velocity of sand. MSc thesis,* Colorado, A & M College: s.n.

Cruz-Matías, I., Ayala, D., Hiller, D. & Gutsch, S., 2019. Sphericity and roundness computation for particles using the extreme vertices model. *Journal of Computational Science,* Volume 30, pp. 28 - 40.

Danzl, R., Helmli, F. & Scherer, S., 2009. *Focus variation - A new technology for high resolution optical 3D surface metrology.* Ljubljana, Slovenia, 10th International Conference of the Slovenian Society for Non-Destructive Testing.

Danzl, R., Helmli, F. & Scherer, S., 2011. Focus variation - A robust technology for high resolution optical 3D surface metrology. *Strojniški Vestnik - Journal of Mechnical Engineering,* 57(3), pp. 245 - 256.

Eddey, C., Tiroyabone, L. & Torres-Cruz, L. A., 2019. *Three dimensional characterisation of the form of sand-sized particles.* Cape Town, s.n.

Fonseca, J., O'Sullivan, C., Coop, M. & Lee, P., 2012. Non-invasive characterization of particle morphology of natural sands. *Soils and Foundation,* 52(4), pp. 712 - 722.

Goodwin, P., 2015. A Primer on the Fundamental Principles of Light Microscopy: Optimizing Magnification, Resolution, and Contrast. *Molecular Reproduction & Development,* Volume 82, pp. 502 - 507.

Helmli, F., 2011. *Focus Variation Instruments, R. Leach (Ed): Optical Measurement of Surface Topography.* Berlin, Germany: Springer.

Holtz, R. D. & Kovacs, W. D., 1981. *An Introduction to Geotechnical Engineering.* Englewood Cliffs, New Jersey: Prentice-Hall Inc..

Howard, J. L., 1992. An evaluation of shape indices as palaeoenvironmental indicators using quartzite and metavolcanic clasts in Upper Cretaceous to Palaeogene beach, river and submarine fan conglomerates. *Sedimentology,* Volume 39, pp. 471 - 486.

Illenberger, W., 1991. Pebble shape (and size!). *J. Sed. Petrol.,* Volume 61, pp. 756 - 767.

Imaging Source, T., 2022. *The Imaging Source.* [Online] Available at: https://www.theimagingsource.com/products/industrial-cameras/usb-2.0-color/dfk72buc02/
[Accessed 12 April 2022].

ISO10934, 2020. *Microscopes - Vocabulary for light microscopes,* s.l.: International Organization for Standardization.

ISO25178-606, 2015. *Geometric product specification (GPS) - Surface texture: Areal - Part 606: Nominal characteristics of non-contact (focus variation) instruments,* s.l.: International Organization for Standardization.

ISO25178-6, 2010. *Geometrical product specifications (GPS) - Surface texture - Areal: Part 6: Classification of methods for measuring surface texture,* s.l.: International Organization for Standardization.

Janoo, V. C., 1998. *Quantification of Shape, Angularity, and Surface Texture of Base Course Materials,* s.l.: s.n.

Kogaku, N. K. K., n.d. *Polarizing Microscope: OPTIPHOT-POL Instruction Manual.* Japan: Nikon.

Krumbein, W., 1941. Measurement and geological significance of shape and roundness of sedimentary particles. *J. Sed. Petrol. ,* Volume 11, pp. 64 - 72.

Krumbein, W. C. & Pettijohn, F. J., 1938. *Manual of Sedimentary Petrology,* New York: D. Appleton-Century Company Inc.,.

Le Pen, L. M. et al., 2013. Dependence of shape on particle size for a crushed rock railway ballast. *Granular Matter,* Volume 15, pp. 849 - 861.

Lee, J. R. J., Smith, M. L. & Smith, L. N., 2007. A new approach to the three-dimensional quantification of angularity using image analysis of the size and form of coarse aggregates. *Engineering Geology,* 91(2), pp. 254 - 264.

Lees, G., 1964a. A new method for determining the angularity of particles. *Sedimentology,* Volume 3, pp. 2 - 21.

Lees, G., 1964b. The measurement of particle shape and its influence in engineering materials. *J. British Granite Whitstone Federation,* Volume 4, pp. 1 - 22.

Liang, H., Shen, Y., Xu, J. & Shen, X., 2021. Multiscale Three-Dimensional Morpological Characterisation of Calcareous Sand Particles Using Spherical Harmonic Analysis. *Front. Phys.*, September, Volume 9.

Li, D., Hyslip, J., Sussman, T. & Chrismer, S., 2015. *Railway Geotechnics.* New York: Taylor and Francis.

Mgangira, M., Anochie-Boateng, J. K. & Komba, J., 2013. *Quantification of Aggregate Grain Shape Characterisation using 3-D Laser Scanning Technology.* Pretoria, South Africa, 32nd South African Transportation Conference.

Montgomery, D. & Runger, G., 2011. *Applied Statistics and Probability for Engineers.* 5th ed. Asia: John Wiley & Sons.

Mvelase, G., Anochie-Boateng, J. & Gräbe, P., 2022. Application of a modern laser technique to evaluate the performance of recycled railway ballast. *Journal of the South African Institute of Civil Engineering ,* 64(4), pp. 16 - 28.

Nie, Z., Liang, Z. & Wang, X., 2018. A three-dimensional particle roundness evaluation method. *Granular Matter,* 20(32).

Nikon, n.d. *NIS Elements D,* s.l.: s.n.

Oakey, R. J. et al., 2005. Grain-shape Analysis - A New Method for Determining Representative Particle Shapes of Natural Grains. *Journal of Sedimentary Research,* Volume 75, pp. 1065 - 1073.

Olympus, 2022. *Knowledge, Depth of Focus.* [Online] Available at: https://www.olympus-ims.com/en/microscope/terms/focal_depth/ [Accessed 9 October 2022].

Pye, W. & Pye, M., 1943. Sphericity determination of pebbles and sand grains. *J. Sed. Petrol. ,* Volume 13, pp. 28 - 34.

Ramanujan, S., 1913. Modular equations and approximations to π. *Q. J. Pure Appl. Math.,* Volume 45, pp. 350 - 372.

S., I. & Spring, K., 1997. *Video microscopy: The fundamentals.* 2nd ed. New York: Plenum Press.

Santamarina, J. & Cho, G., 2004. *Soil behaviour: The role of particle shape.* London, Proc. Skempton Conf..

Selig, E. & Waters, J., 1994. *Track Geotechnology and Substructure Management.* 1st ed. London: Thomas Telford.

Shin, H. & Santamarina, J. C., 2013. Role of particle angularity on the mechanical behaviour of granular mixtures. *J. Geotech. Geoenviron.,* Volume 139, pp. 353 - 355.

Sneed, E. & Folk, R., 1958. Pebbles in the Lower Colorado River, Texas: a study in particle morphogenesis. *J. Geol,* 66(2), pp. 114-150.

Spring, K. R. & Davidson, M. W., 2022. *MicroscopyU.* [Online] Available at: https://www.microscopyu.com/microscopy-basics/depth-of-field-and-depth-of-focus
[Accessed 19 July 2022].

Sun, Y., Indraratna, B. & Nimbalkar, S., 2014. *Three-dimensional characterisation of particle size and shape for ballast,* s.l.: Faculty of Engineering and Information Sciences - Papers: Part A, University of Wollongong.

Wadell, H., 1932. Volume, shape and roundness of rock particles. *J. Geol.,* Volume 40, pp. 443 - 451.

Wang, X. et al., 2020. Shape Characteristics of Coral Sand from the South China Sea. *Journal of Marine Science and Engineering,* Issue 8.

Weibull, W., 1951. A statistical distribution function of wide applicability. *J. Appl. Mech.,* Volume 18, pp. 293 - 297.

Wentworth, 1919. A laboratory and field study of cobble abrasion. *J. Geol.,* Volume 2, pp. 507 - 521.

Xu, X., Hagemeier, S. & Lehmann, P., 2022. Outlier Elimination in Rough Surface Profilometry with Focus Variation Microscopy. *Metrology,* Volume 2, pp. 263 - 273.

Yu, L., Gong, F., You, Z. & Wang, H., 2018. Aggregate Morphological Characterisation with 3D Optical Scanner vs X-Ray Computed Tomography. *J. Mater. Civil Eng.,* Volume 30.

Zhao, B. et al., 2015. An investigation of single sand particle fracture using X-ray micro tomography. *Géotechnique,* 65(8), pp. 625 - 641.

Zhou, B. & Wang, J. F., 2016. Generation of a realistic 3D sand assembly using X-ray micro-computed tomography and spherical harmonic-based principal component analysis. *Int. J. Numer. Anal. Meth. Geomech..*

Zhou, B., Wang, J. & Wang, H., 2017. Three-dimensional sphericity, roundness and fractal dimension of sand particles. *Géotechnique,* May.

Zingg, T., 1935. Beitrage zur Schootteranalyse. Schweizminer.. *Petrog. Mitt.,* Volume 15, pp. 38 - 140.